

STRUCTURE AND THERMAL TRANSPORT
IN DISORDERED MATERIALS:

MOLECULAR DYNAMICS SIMULATION
AND ANALYSIS WITH THE WAVELET TRANSFORM

A Dissertation presented to the Faculty of
the School of Engineering & Applied Science at
the University of Virginia in partial fulfillment of
the requirements of the degree of
Doctor Philosophiae

Christopher H. Baker

May 17, 2015

Signatures

Author

Christopher H. Baker,
Dept. Mech. & Aero. Eng. _____

Advisory Committee

PROF. PATRICK E. HOPKINS, *chair*,
Dept. Mech. & Aero. Eng. _____

PROF. PAMELA M. NORRIS, *advisor*,
Dept. Mech. & Aero. Eng. _____

PROF. LEONID V. ZHIGILEI,
Dept. Mater. Sci. & Eng. _____

PROF. CHARLES A. SACKETT,
Department of Physics _____

PROF. ALAN J. H. MCGAUGHEY,
Dept. Mech. Eng.,
Carnegie Mellon University _____

Dean of the School of Engineering & Applied Sciences

DEAN JAMES H. AYLOR _____

To God and His Son,
who are the architects of this amazing world in which I live.

To my wife Louisa,
whose love and support empower me.

And to our first child,
who is to join us soon and is already filling our lives with joy.

ABSTRACT

The disordered atomic structure of alloys and glasses hinders the development of theoretical models of thermal transport through them, as many of the assumptions used for crystals, which are ordered, are no longer valid. The vibration of atoms carries most of the heat in semiconductors and insulators, whether they be disordered materials or crystalline. Yet because the normal modes of vibration are inherently non-localized, broadband, and interact with each other in complex ways, directly observing their behavior in either experiments or simulations poses a major challenge. Attempting to answer questions like, “how does the phonon population interact with or change near an interface?” adds further complexity. Classical molecular dynamics simulation offers a means to study alloys and glasses by explicitly modeling the disordered arrangement of atoms within “virtual experiments.” Furthermore, molecular dynamics simulations implicitly contain everything there is to know about the vibrational transport through them, and so the challenge becomes one of developing post-processing techniques capable of extracting the desired information on thermal transport.

In this work, I develop the wavelet transform as a tool to analyze molecular dynamics simulations to extract the localized—with respect to both location and time—dynamics of vibrational heat carriers in bulk crystals, interfacial systems, and glasses. Three types of simulations developed with the wavelet transform in mind may yield the following: 1) visualization of phonon wave-packets undergoing anharmonic decay and scattering with an interface, 2) steady-state phonon populations versus position during non-equilibrium thermal transport across an interface in a 1-D chain, and 3) ballistic-diffusive transport of vibrational energy in response to localized heating and transient decay of thermal energy in a glass. Using the newly developed simulation and analysis technique for glasses, I demonstrate its efficacy for calculating the frequency-dependent vibrational diffusivity of amorphous silicon and silica. The results for amorphous silicon agree with the Allen-Feldman theory but the method has two advantages: it scales more efficiently with the number of atoms, requiring only $\mathcal{O}(N)$ instead of $\mathcal{O}(N^3)$ computation time; and the bond force constants are not required. Lastly, using molecular dynamics simulation, I decouple the short-range order from the long-range order in a model of SiGe alloy and find that the short-range order accounts for the entire change of the thermal conductivity upon ordering.

CONTENTS

1	INTRODUCTION	1
1.1	Thermal Conductivities of Amorphous Materials	1
1.2	Theory of Thermal Transport in Amorphous Materials	3
1.3	Thermal Conductivities of Alloys	5
1.4	Theory of Thermal Transport in Alloys	6
1.5	Overview of Doctoral Contribution	8
2	NUMERICAL METHODS	10
2.1	The Continuous Wavelet Transform	10
2.2	Calculation of the Vibrational Density of States	16
2.3	Constructing Alloys with Variable Long- and Short-Range Order	19
2.3.1	Long-Range Order	20
2.3.2	Short-Range Order	22
2.4	Contributions	24
3	LEVERAGING THE WAVELET TRANSFORM IN MOLECULAR DYNAMICS SIMULATIONS	25
3.1	Wave-Packet Simulations of Interfaces and Anharmonic Scattering	25
3.1.1	Anharmonic scattering of a wave-packet	27
3.1.2	Wave-packet studies of interface transmission	28
3.2	Steady-State Phonon Populations Near an Interface	30
3.3	Transient Thermal Transport in Amorphous Materials	32
3.4	Contributions	35
4	POTENTIALS FOR THE SIMULATION OF AMORPHOUS SILICON AND SILICA	36
4.1	Potentials	37
4.1.1	Silicon Potentials	38
4.1.2	Silica Potentials	39
4.2	Methods	40
4.2.1	Obtaining the Amorphous Structure	40
4.2.2	Thermal Conductivity	41
4.2.3	Density of States	41
4.2.4	Structural Characterization	42
4.2.5	Elastic Constants	42
4.3	Results	42
4.3.1	a-Si Results	42
4.3.2	a-SiO ₂ Results	44
4.4	Discussion	46
4.5	Tabulated Data	49

4.6	Contributions	50
5	EFFECT OF LONG- AND SHORT-RANGE ORDER ON SILICON-GERMANIUM ALLOY THERMAL CONDUCTIVITY	51
5.1	Structure Generation and Characterization	51
5.2	Thermal Conductivity and Size Effects	53
5.3	Normal Mode Relaxation Times	54
5.4	Contributions	58
6	FREQUENCY DEPENDENT VIBRATIONAL DIFFUSIVITY OF AMORPHOUS SILICON AND SILICA CALCULATED WITH THE WAVELET TRANSFORM	59
6.1	The Cahill–Pohl model and Allen–Feldman theory	59
6.2	Simulation Details	62
6.3	The effect of ping direction, atom, and magnitude	64
6.4	Results and Discussion	66
6.5	Contributions	71
7	CONCLUSIONS	73
	Acknowledgements	76
	List of Symbols	77

LIST OF FIGURES

Figure 1.1	Experimental thermal conductivity versus temperature for select crystalline and amorphous materials	2
Figure 1.2	Experimental thermal conductivity of $\text{Si}_{1-x}\text{Ge}_x$, $\text{Cu}_{1-x}\text{Au}_x$, and $\text{PbTe}_{1-x}\text{Se}_x$ alloys at 300 K	6
Figure 2.1	Kernel functions for the Fourier and wavelet transforms	12
Figure 2.2	Determination of the minimum and maximum analyzable frequencies by the wavelet transform	13
Figure 2.3	Analysis of elementary functions in the time, frequency, and wavelet domains	15
Figure 3.1	Anharmonic scattering of a large-amplitude wave-packet viewed with the wavelet transform	27
Figure 3.2	Scattering of a wave-packet with an interface in multiple wave-packet simulation viewed with the wavelet transform	28
Figure 3.3	Interface morphologies studied by wave-packet simulation: alloyed, chemically graded, sawtooth, and sinusoidal interface profiles	29
Figure 3.4	Polarization conversion of a wave-packet scattering with a sawtooth interface viewed by the wavelet transform	29
Figure 3.5	Bulk dispersion of two materials in a 1-D chain	30

Figure 3.6	Spatial temperature profiles and space-wavenumber phonon energy distributions for non-equilibrium molecular dynamics simulations of harmonic and anharmonic 1-D chains	31
Figure 3.7	Position-time-frequency energy distribution of ballistic transport in [110] direction of silicon obtained by the wavelet transform	32
Figure 3.8	Frequency-dependent phonon group velocities in high-symmetry directions of silicon obtained by the wavelet transform	33
Figure 3.9	Sketch of simulation method for calculating frequency-dependent vibrational diffusivity of an isotropic material	34
Figure 4.1	Radial distribution function of simulated a-Si	43
Figure 4.2	Angular distribution function of simulated a-Si	44
Figure 4.3	Coordination histogram of simulated a-Si	45
Figure 4.4	Density of states of simulated a-Si	45
Figure 4.5	Radial distribution function of simulated a-SiO ₂	46
Figure 4.6	Angular distribution functions of simulated a-SiO ₂	47
Figure 4.7	Density of states of simulated a-SiO ₂	48
Figure 5.1	Short-range order parameters of simulated Si _{0.5} Ge _{0.5} structures generated by a Monte Carlo method	52
Figure 5.2	Thermal conductivities of 8 ³ unit cell Si _{0.5} Ge _{0.5} structures with varying long- and short-range order	54
Figure 5.3	Size effects on the thermal conductivity for select Si _{0.5} Ge _{0.5} structures	55
Figure 5.4	Fitting of normal mode velocity coordinate power spectral density to obtain relaxation times, $\mathbb{L} = \mathbb{S}_1 = 0$ structure	56
Figure 5.5	Mode relaxation times for slices through \mathbb{L} - \mathbb{S}_1 parameter space	57
Figure 6.1	Effect of ping direction on calculated a-Si frequency-dependent vibrational diffusivity for a transient heat decay simulation with wavelet analysis	65
Figure 6.2	Effect of pinged atom	65
Figure 6.3	Effect of ping magnitude	66
Figure 6.4	Fitting of wavelet transformed transient heat decay to analytical transport model	67
Figure 6.5	Comparison of Cahill–Pohl model, Allen–Feldman theory, and present predictions of vibrational diffusivity in simulated amorphous silicon	69
Figure 6.6	Spectral diffusivity of a-Si obtained by the wavelet transform-based method for different bond strengths and structures	70
Figure 6.7	Radial distribution functions of $\sim 100,000$ atom models of a-Si for different potentials and preparation methods	70

Figure 6.8	Spectral diffusivity of simulated a-SiO ₂ obtained by the wavelet transform-based method	71
------------	---	----

LIST OF TABLES

Table 3.1	Wavenumber distribution of anharmonic wave-packet energy over time	27
Table 4.1	Energy parameters used in Stillinger-Weber potentials of a-Si	38
Table 4.2	Parameters of Tersoff potential for a-Si and a-SiO ₂	39
Table 4.3	Parameters used in Buckingham-style potentials of a-SiO ₂	40
Table 4.4	Temperatures of liquid phase before quenching for each a-Si and a-SiO ₂ potential	41
Table 4.5	Thermophysical properties of simulated a-Si compared to experiment for various potentials and quench rates	49
Table 4.6	Thermophysical properties of simulated a-SiO ₂ compared to experiment for various potentials and quench rates	49

1

INTRODUCTION

Solids may be categorized as either crystalline or disordered depending on the arrangement of their constituent atoms. The atomic structure of a crystal is defined by a *basis* arrangement of atoms that is repeated on each point of an infinite, space-filling *lattice* [1]. In the strictest sense, materials that fail either of these criteria are disordered. In an amorphous material, or “glass,” the atoms are neither grouped into a basis nor do they sit on the points of a lattice. Instead, the atoms are more or less randomly distributed throughout space [2]. The atoms of an alloy are similar to those of a crystal in that the structure is defined by an arrangement of atoms that is repeated on each lattice site. However, the identities of the atoms assigned to a lattice site may differ from site to site, breaking the translational symmetry intrinsic to a crystal.

Among other considerations, the transport properties of a material clearly depend on its atomic structure. So one can expect that the thermal conductivity of a glass or an alloy will differ from that of a crystal made of the same elements insofar as their structures differ—both qualitatively and quantitatively. Therefore, pursuit of a theoretical understanding of thermal transport in glasses and alloys must begin with those details of their atomic structures that lead to common traits among their thermal conductivities.

1.1 THERMAL CONDUCTIVITIES OF AMORPHOUS MATERIALS

Thermal transport in amorphous materials has been the focus of great research effort over the past half-century. The unique thermal properties of amorphous materials, and the challenges in modeling them, undoubtedly arise from their disordered structure. Upon collating the experimental data of several amorphous materials in 1971, Zeller and Pohl first noticed that all of the thermal conductivities were within a factor of five for the whole temperature range [3]. Conversely, the thermal conductivities of the crystalline polymorphs¹ may differ by four orders of magnitude, *e.g.* diamond and ethanol at 77 K (Fig. 1.1). Zeller and Pohl also noticed that the trends were all similar, monotonically increasing with temperature, with a characteristic *plateau* in thermal conductivity at about 10 K. The heat capacity, too, differed from that of a crystal, having an additive term proportional to T at low temperatures. Freeman and Anderson subsequently noticed in 1986 that the thermal conductivity curves collapse onto each other after applying a simple scaling procedure [4]. One exception to this *universality* was that the plateaus, while spanning the same scaled temperature, had different magnitudes

¹ Polymorph is nearly synonymous with *allotrope*, but includes materials of more than one element.

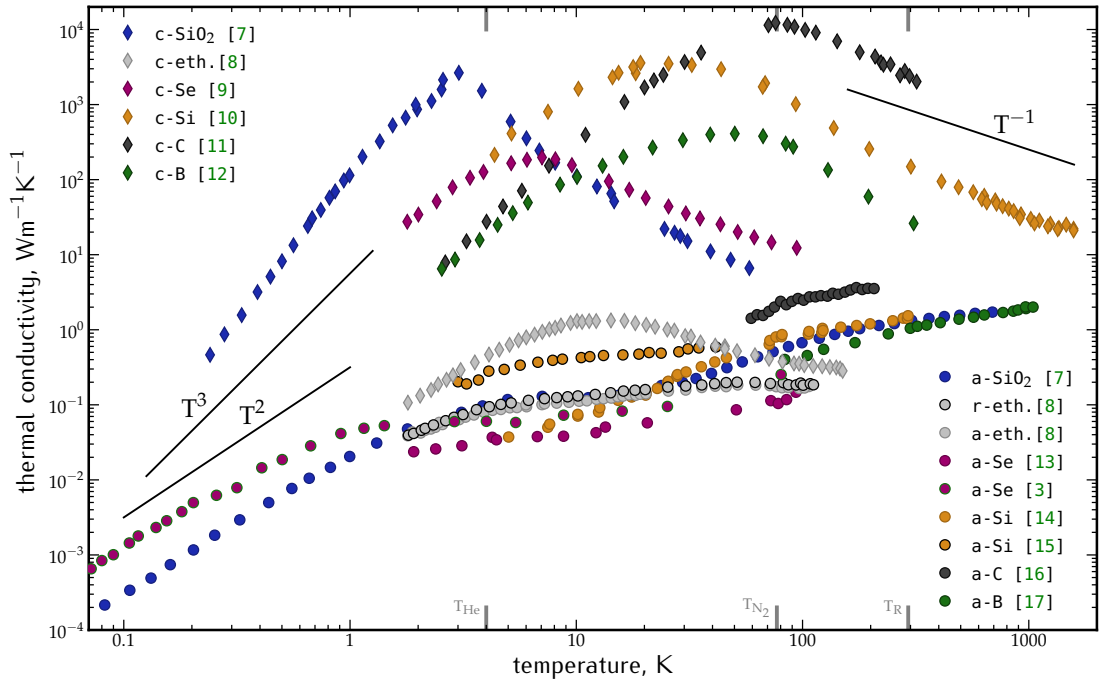


Figure 1.1: Experimental thermal conductivity versus temperature for select crystalline and amorphous materials. Crystalline silica [7], ethanol [8], selenium [9], silicon [10], carbon (diamond) [11], and boron [12] all exhibit a rise in thermal conductivity in proportion to the low temperature heat capacity, a local maximum, and decrease as umklapp scattering dominates. For non-cubic crystals, thermal conductivity is taken parallel to the c-axis. Amorphous silica [7], ethanol [8], selenium [3, 13], silicon [14, 15], carbon [16], and boron [17] all have thermal conductivities that are orders of magnitude lower than for the crystalline phase. The trends also differ: monotonically increasing with temperature with a plateau at ~ 10 K for typical amorphous materials. Amorphous silicon and carbon are predicted to be atypical in this regard [5]. Rotationally disordered ethanol [8] has nearly identical behavior to amorphous ethanol. The grey tick marks denote the boiling temperatures of helium and nitrogen, and room temperature, respectively.

of scaled thermal conductivity. Pohl *et al.* incorporated acoustic attenuation data into their 2002 review, showing that the cause of the low temperature trends was also responsible for the acoustic attenuation [5]. The same data showed that amorphous carbon, silicon, and germanium had atypical acoustic attenuations that were two orders of magnitude smaller than all other amorphous materials, making them atypical amorphous materials. Finally, a 2007 review by Lubchenko and Wolynes [6] includes more recent developments and discusses the physics of the supercooled liquid at the glass transition temperature and its relationship with the low temperature properties. While much has been learned over the last few decades, there is still no comprehensive theory for the thermal properties of amorphous materials.

Figure 1.1 summarizes the thermal conductivities of several amorphous materials and contrasts them with their crystalline polymorphs. The effect of disordering a crystal is an orders-of-magnitude drop in thermal conductivity across all temperatures. Besides the magnitude of thermal conductivity, the temperature trends are completely different. The crystalline trend has a low temperature T^3 scaling from the Debye theory of heat capacity, a high temperature T^{-1} scaling due to umklapp scattering, and a maximum in between. The amorphous trend has a low temperature scaling of roughly T^2 [3], monotonically increases with temperature, and has the plateau at about 10 K.

The plotted crystalline data cover a range of crystal types and bonding, with a commensurate spread of thermal conductivities. Represented are basis sizes of two (crystalline Si or c-Si and c-C) to several dozen (β phase of c-B) atoms, as well as hexagonal (c-Se, α phase of c-SiO₂), monoclinic (c-ethanol), and face-centered cubic (c-Si, c-C, c-B) lattices. The amorphous data also span different classes of amorphous materials, but exhibit a relatively tight clustering, within a factor of ten. Amorphous silica (a-SiO₂), a-ethanol, and a-Se have the plateau. The plateau of a-SiO₂ is clear while the plateaus of the other two are slight. Data for a-Si is conflicted: Pompe and Hegenbarth [15] show a slight plateau, but Zink *et al.* [14] do not, which suggests that preparation profoundly affects an amorphous material. Ethanol has two disordered phases: the molecules of a-ethanol are randomly distributed in space, and those of r-ethanol sit on body-centered cubic lattice sites but have random orientation. The thermal conductivities of the two phases are nearly identical [8], underscoring the universality of whatever imbues amorphous materials with their thermal properties.

1.2 THEORY OF THERMAL TRANSPORT IN AMORPHOUS MATERIALS

The trend of the thermal conductivity of amorphous materials (illustrated in Fig. 1.1) may be divided into three regions: below the plateau, at the plateau, and above the plateau. These regions correspond to low, intermediate, and high temperature regimes, respectively. Theoretical efforts to explain the low temperature heat capacity and T^2 thermal conductivity trends have been variations of the *two-level system* [18, 19]. Essentially, within the disordered state, some atoms or groups of atoms have two spatial configurations that are nearly equivalent in energy but separated by a small displacement vector and energy barrier. Then, an atom (or atoms) can tunnel between the two states, yielding a heat capacity term proportional to T [18, 19]. Since the states are accessible only by tunneling, there is a characteristic time associated with the transition, and the heat capacity term linear in T is therefore time-dependent [18]. Tunneling atoms in a two-level system interact with acoustic phonons through resonant scattering, explaining the T^2 scaling of thermal conductivity [18, 19]. In addition to the indirect experimental evidence for the two-level systems offered by the low temperature heat capacity and thermal conductivity, two-level systems matching the theory were observed in simulations of amorphous materials [20–23]. The potential surface giving rise to the two-level system may also be understood in terms of a soft anharmonic potential with up to fourth order terms [24].

Moving beyond a model of thermal conductivity based on phonon transport, Allen and Feldman, along with other collaborators, expounded a theoretical basis for vibrational transport at and above the plateau [25–28]. In their model, the vibrational spectrum is divided into three types of heat carriers based on the characteristics of their corresponding mode eigenvectors, calculated within the theoretical framework of lattice dynamics [29]. At low frequencies, the eigenvector is a plane-wave, which is to say that it is “phonon-like.” These modes can propagate some distance before scattering, like phonons, and are hence called *propagons*. At high

frequencies, the eigenvector is localized, meaning that it has a maximal magnitude at a certain location and an exponentially decreasing magnitude moving away. Within the harmonic approximation, these localized modes cannot carry heat (although they still contribute to the heat capacity) [30], and for this reason they are called *locons*. At intermediate frequencies, the eigenvectors are neither extended nor localized according to the above definitions. Rather, the eigenvector decays somewhat slower than exponentially, yielding modes with intrinsic diffusivity, hence *diffusons*. The diffusivity of these modes scales with the degree of overlap of their eigenvectors with those of spatially adjacent modes having nearly the same frequency [26]. The thermal conductivity in the plateau region of a-Si [15, 31] is thus explained by Feldman *et al.* as due to the cross-over between heat being primarily carried by propagons and heat being carried by diffusons [27].

Above the plateau, the theory of Allen and Feldman (A-F) as discussed above, and a model by Cahill and Pohl (C-P) [7, 32] offer competing explanations for the thermal conductivity. The two approaches lie on opposite ends of the complexity spectrum, and pragmatically, each has strengths and weaknesses. One goal of this dissertation is to obtain an independent estimate of the transport in this regime so as to provide a point of comparison between the A-F theory and the C-P model. A secondary goal is to work towards a theory balancing their respective strengths and weaknesses.

In the A-F theory, as the temperature rises above the plateau, the disorder of the amorphous structure more effectively scatters the propagons; meanwhile the diffusons begin to contribute, producing “a plateaulike feature for a fairly broad range of parameters” [27]. As the temperature increases further, the diffusion contribution to the thermal conductivity monotonically rises and eventually saturates [27], which is consistent with the trends plotted in Figure 1.1. The theory has its foundation in lattice dynamics and condensed matter physics, and thus provides a more accurate prediction of the thermal conductivity at and above the plateau. But to do so, the theory requires knowledge of the exact microstate of the system, including the harmonic force constants acting between the atoms. Such information will only ever be available in simulations. To accurately represent the structure of an amorphous material, simulations require on the order of thousands of atoms or more. Thus, the computational cost of using *ab initio*-based methods to calculate the force constants is prohibitively expensive for the immediate future, leaving less accurate empirical models as the only alternative. Finally, A-F theory requires calculation of the eigenvalues and eigenvectors of the system’s dynamical matrix [29], with a cost scaling with the number of atoms cubed (see Sec. 6.1). This limits the calculation to domains with length scales on the order of 4 nm based on current computing power.

The alternative for predicting high temperature thermal conductivity is the C-P model [7, 32]. Adapting an earlier theory of crystalline thermal conductivity by Einstein [33] to the disordered amorphous state, Cahill and Pohl assumed that phonons scatter with a mean-free-path equal to one-half their wavelength. This yields a f^{-1} frequency dependence of the diffusivity. For such a simple model, it gives reasonable estimates of the experimental high temperature thermal conductivity [32]. The model requires only the density and sound speeds of a material to make its prediction of the thermal conductivity [7]. However, the prediction

ignores all aspects of the microstructure, omitting the very characteristics that apparently define an amorphous material and its thermal properties.

A successor to the A–F theory and the C–P model would therefore incorporate the statistical structure of the material, unlike the C–P model, without requiring knowledge of the exact microstate and diagonalization of the dynamical matrix, unlike the A–F theory. Pursuit of such a theory should guide research efforts in this area. And while this dissertation does not reach such an end goal, it does take a step forward by detailing a new method for the calculation of the frequency-dependent diffusivity from the system’s microstate that does not require diagonalization of the dynamical matrix (Sec. 3.3 and Chap. 6).

An improved understanding of amorphous materials is vital for advancing technologies that utilize them. In applications such as phase-change memory [34, 35] and thermal insulation [36], the thermal conductivity and heat capacity are of primary concern. In other applications, for example integrated circuits [37], metallic glasses [38], and Josephson junctions in quantum computers [39], the properties are secondary but of no less concern depending on the implementation. An improved understanding may also translate to other types of disordered materials, like alloys.

1.3 THERMAL CONDUCTIVITIES OF ALLOYS

An alloy is defined by a series of parameters: the lattice and the atoms’ relation to it; the composition as $N-1$ concentrations, where N is the number of elements composing the alloy; the long range-order parameter, which measures the probability that a certain element may be found on a certain lattice site [40]; and a series of short-range order parameters: one for each neighbor distance found in the alloy [41] that gives the probability that an atom is surrounded by its preferred neighbors with respect to the ordered structure. An order parameter of one corresponds to an alloy defined by a lattice and basis of definite atoms. For an order parameter of zero, the probability of finding a certain element on a certain lattice site is equal to its concentration in the alloy, *i.e.* the atoms are randomly placed on the lattice. The structure of the completely disordered alloy may also be modeled as a basis of “averaged” atoms that are repeated on each lattice site [42]. The present work will focus on binary alloys, and the interpretation and calculation of long- and short-range order parameters will be further discussed in Section 2.3.

The thermal conductivity of an alloy is most sensitive to its composition. For a binary alloy, $A_{1-x}B_x$, the thermal conductivity rapidly drops as the concentration, x , increases from zero. For semiconducting alloys at a concentration of approximately 20%, the thermal conductivity flattens out, and then there is a weak dependence on concentration until about 80%, where the conductivity rapidly increases towards the thermal conductivity of material B. For specific compositions, the alloy may also exhibit variable ordering, a trait most often found in metallic alloys, like Cu_3Au [40].

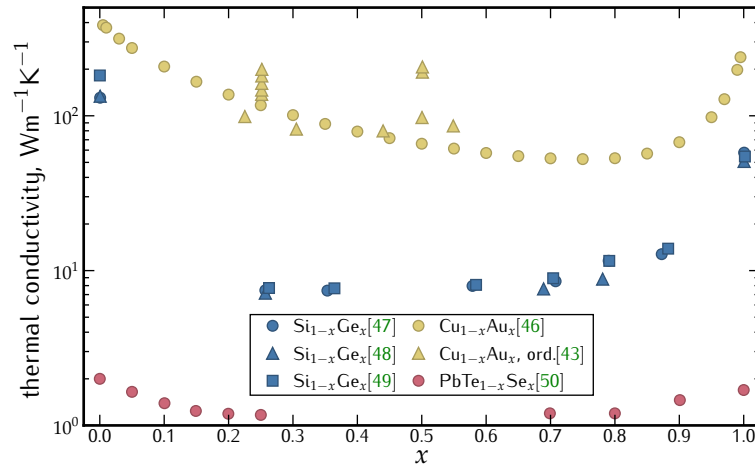


Figure 1.2: Experimental thermal conductivity of $\text{Si}_{1-x}\text{Ge}_x$ [47–49], $\text{Cu}_{1-x}\text{Au}_x$ [43, 46], and $\text{PbTe}_{1-x}\text{Se}_x$ [50] alloys at 300 K. The thermal conductivity rapidly decreases upon alloying and plateaus at $x \approx 0.2$ for semiconducting alloys. Note the rise in thermal conductivity with ordering for Cu_3Au and CuAu (yellow triangles).

The room temperature thermal conductivities of select binary alloys are plotted in Figure 1.2. $\text{Cu}_{1-x}\text{Au}_x$ is the paradigm of alloys that exhibit ordering [40–43]. $\text{Si}_{1-x}\text{Ge}_x$ and $\text{PbTe}_{1-x}\text{Se}_x$ are high temperature thermoelectric materials [44, 45]; the thermal conductivity of $\text{Si}_{1-x}\text{Ge}_x$ is studied in Chapter 5. Although the metallic $\text{Cu}_{1-x}\text{Au}_x$ alloy [46] does not plateau for intermediate x , it does follow the same general pattern as the other alloys.² Also plotted are the thermal conductivities of ordered Cu_3Au and CuAu [43], which demonstrate a rise in thermal conductivity with ordering.³ While $\text{PbTe}_{1-x}\text{Se}_x$ comprises three elements, the tellurium and selenium atoms cannot occupy the lead lattice sites, and thus only one concentration is needed to define the alloy.

1.4 THEORY OF THERMAL TRANSPORT IN ALLOYS

The theoretical framework for thermal transport in alloys is closely tied to that of phonon transport in crystals. A disordered alloy may be modeled as a crystal whose lattice constant, atomic masses, and interatomic forces are the concentration-weighted averages of the species composing the alloy. For this *virtual crystal approximation*, Abeles provided expressions for the phonon-phonon scattering and phonon-defect scattering [51]. The specific case of an isotopically disordered alloy, *i.e.* an alloy for which only the masses of the species differ, was subsequently treated more rigorously by Tamura [52]. In these theories, the disorder is treated as a perturbation to the masses and interatomic forces of the virtual crystal. This theory accurately models the experimental $\text{Si}_{1-x}\text{Ge}_x$ thermal resistivity obtained by Abeles *et al.* [48] and has been used recently in *ab initio* calculations of the thermal conductivity of $\text{Si}_{1-x}\text{Ge}_x$ [53] and $\text{PbTe}_{1-x}\text{Se}_x$ [54]. The virtual crystal framework is not restricted to theoretical modeling or *ab initio* calculation. For example, it has been applied to the analysis of classical molecular

² Data is a theory-based interpolation of experimental data by many groups.

³ Data is aggregated from previous studies by the author.

dynamics simulations of $\text{Si}_{1-x}\text{Ge}_x$ [55] and to the prediction of the boundary conductance of a disordered interface [56].

Theoretical investigation into the effect of alloy ordering on transport has focused on the electronic structure [57, 58] and electronic conductivity [59, 60] of metallic alloys [61]. Harrison, Hauser, and their collaborators extended the theory of electronic transport to certain semiconducting ternary III-V alloys [62–64]. The lattice-mediated conductivity, or indeed the overall thermal conductivity, of semiconductor devices was not a huge concern until a decade and a half ago, when the heat generated by these devices began to outpace the ability of cooling technology [65]. Furthermore, most semiconductors may only be found in their thermodynamically favored state, whether that be completely disordered [66] or completely ordered [67]. So it is difficult to coax them into a partially ordered state, a task that typically requires non-equilibrium growth techniques [68, 69]. Perhaps for these reasons, a theoretical development of lattice-mediated thermal conductivity with alloy ordering has lagged behind the electronic theory.

While a theory of electronic transport as a function of ordering may be sufficient for most metallic alloys, where lattice vibrations contribute less than 10% of the overall thermal conductivity [46], such a theory is insufficient for partially ordered semiconducting alloys. In a recent pair of studies, Duda *et al.* [70, 71] performed molecular dynamics simulations of a Lennard-Jones alloy, systematically varying the long-range order and measuring the effect on the lattice thermal conductivity. Their results show that at low temperatures relative to the melting point, the thermal conductivity spans nearly an order of magnitude between the disordered and ordered states. Furthermore, the majority of the change occurs at long-range order parameters close to one. That the aforementioned electronic theories are concerned with the short-range order [57–59] begs the question of how short-range order affects the lattice thermal conductivity of partially ordered semiconducting alloys. Furthermore, by what mechanism does the ordering of a semiconducting alloy influence the thermal conductivity? These questions are addressed in Chapter 5 of this dissertation, where simulations of $\text{Si}_{0.5}\text{Ge}_{0.5}$ with independently controlled long- and short-range order parameters show that it is actually the short-range order that dictates the thermal conductivity of this material.

As with amorphous materials, an improved theoretical understanding of alloy thermal conductivity would benefit technologies that utilize them. Two current technological applications of alloys are in thermoelectrics [72, 73] and data storage [74]. In thermoelectrics, the figure of merit is inversely proportional to the thermal conductivity, giving disordered semiconducting alloys with reasonable electronic properties good performance. There has been much recent research into avenues for reducing the thermal conductivity of $\text{Si}_{1-x}\text{Ge}_x$ alloys without adversely affecting the electronic properties [44, 75–80]. Highly ordered iron-based alloys are desirable for their magnetic properties, and they are being used in combination with intense laser heating to boost data storage densities in the next generation of hard-drive technology, “heat-assisted magnetic recording media” [74, 81–84].

1.5 OVERVIEW OF DOCTORAL CONTRIBUTION

Classical molecular dynamics simulation offers a powerful yet flexible tool for studying nanoscale thermal transport through disordered materials. By using empirical potentials to describe the atomic interactions, classical molecular dynamics simulation is several orders of magnitude faster than *ab initio*-based simulations of atomic dynamics [85–87]. This offers the capability to simulate anywhere from thousands to millions of atoms and permits the simulator to explicitly include the disorder of amorphous or alloy materials, options not available when using the virtual crystal approximation, for instance. By integrating Newton’s second law, the simulation calculates the trajectory of an atomic system, outputting the positions, velocities, and energies of the atoms over time. This information implicitly contains everything there is to know about the vibrational energy transport in the system,⁴ and so the task of the simulationist becomes one of signal processing to transform the data into a form susceptible to analysis and interpretation.

Since phonons are the plane-wave vibrations of the atoms in a crystal, it is no surprise that the Fourier transform [88] has been used to great effect to analyze different aspects of molecular dynamics simulations. Two examples are the calculation of the phonon density of states [29] and the static structure factor [89]. But methods based on the Fourier transform cannot say where or when changes in the phonon population occur because the Fourier transform sacrifices spatial and temporal information to obtain the wavenumber or frequency spectrum. The *where* and *when* of changes in the phonon population are intimately related to their transport and scattering. Answers to *where* and *when* phonons scatter are particularly pertinent to materials and devices with nanoscale heterogeneities, where the thermal behavior of the device is strongly dependent on phonon dynamics over nanometer length scales and picosecond time scales.

The wavelet transform [90], like the Fourier transform, is an analysis technique that provides spectral information, *e.g.* wavenumber and frequency. But, unlike the Fourier transform, it retains some spatial and temporal information. Farge presents a history of the development of the wavelet transform in her review on the topic [91]. Following its derivation, the wavelet transform found applications in such diverse fields as geophysics [92], signal processing [93], data compression [94], turbulence [91], and meteorology [95]. The wavelet transform has been used once before in the context of nanoscale thermal transport. In a study by Shiomi and Maruyama, the authors analyzed the quasi-ballistic transport of thermal energy in a carbon-nanotube using the wavelet transform [96]. By designing molecular dynamics simulations around the capabilities of the wavelet transform, the simulationist may attack many long-standing questions regarding the fundamental physics of vibrational energy transport in a variety of nanoscale systems.

My primary contributions to the nanoscale thermal transport community, as presented in this dissertation, are two-fold: 1) The development of three new simulation procedures based on the wavelet transform that extend the ability of molecular dynamics simulations to study

⁴ Except, perhaps, for the scattering of acoustic phonons with two-level states, which is an inherently quantum mechanical phenomenon.

nanoscale thermal transport in bulk crystalline and amorphous materials, as well as interfacial systems; and 2) The decoupling of short-range order from long-range order in simulations of $\text{Si}_{0.5}\text{Ge}_{0.5}$ that demonstrate that the short-range order parameter entirely determines the thermal conductivity of the alloy. My work has also yielded two secondary contributions: 3) The systematic evaluation of potentials for silicon and silica with attention to their ability to reproduce room-temperature experimental thermophysical properties of the amorphous phase; 4) The application of the new wavelet-based simulation procedure to calculate the frequency-dependent vibrational diffusivity of amorphous silicon and silica and an investigation of the role of bonding on diffusivity.

I organize the remainder of the dissertation as follows. In Chapter 2, I detail the key numerical methods to be used in the construction and analysis of my simulations, especially the implementation and interpretation of the wavelet transform. In Chapter 3, I present three applications of the wavelet transform to molecular dynamics simulations of nanoscale thermal transport. I show how the wavelet transform can be used to analyze the following: wave-packet simulations of harmonic interface transmissivity and anharmonic phonon decay, steady-state non-equilibrium thermal transport across an interface, and transient thermal transport in an amorphous material to calculate the frequency-dependent vibrational diffusivity. Although even very simple interatomic potentials can capture much of the underlying physics of thermal transport in molecular dynamics simulations, if attempting to simulate a particular material system, it is prudent, when possible, to vet the interatomic potential for that material system. I do this in Chapter 4 by comparing the ability of several candidate potentials to reproduce the thermophysical properties of amorphous silicon and amorphous silica.

In Chapters 5 and 6, I apply the methods and results of the previous chapters to simulations of disordered materials to better understand the effect of their structure on the thermal transport through them. In Chapter 5, I decouple the long-range and short-range order parameters of a simulated $\text{Si}_{0.5}\text{Ge}_{0.5}$ alloy and investigate their respective impacts on the thermal conductivity and mode relaxation times. Finally, in Chapter 6, I apply the simulation procedure outlined in Section 3.3 to models of amorphous silicon and amorphous silica to calculate their frequency-dependent vibrational diffusivities.

2

NUMERICAL METHODS

The researcher who performs simulations must become well acquainted with a variety of numerical methods. Because the capital cost of pursuing new research directions via simulation is minuscule compared to that of experiments, the limiting factor for the simulationist is often how quickly he can comprehend and integrate new computational techniques and approaches into his simulations. To this end, clear and applied explanations of numerical methods are invaluable. In this chapter, I attempt such a clear presentation of three numerical methods: the wavelet transform, the calculation of the vibrational density of states from molecular dynamics trajectories, and the construction of simulated alloys with specified long- and short-range order. As these methods are foundational to some of the other research in this dissertation, I have spent much time studying and contemplating them. In retrospect, I have found clear treatments of these topics lacking. While none the methods of this chapter are wholly novel, I believe my presentation of them is—I hope that my explanations will fill the void of clear treatments of these methods and will aid other simulationists seeking to employ them.

2.1 THE CONTINUOUS WAVELET TRANSFORM

The following presentation of the wavelet transform follows the spirit of Jordan *et al.* [97] and Baker *et al.* [98]. The key difference is that here, the signal is transformed directly into the time–frequency domain instead of the time–scale domain.

To understand the wavelet transform, it is instructive to first examine the form and function of the Fourier transform and other integral transforms [88].¹ All of these transformations are achieved by convoluting the signal at hand with a *kernel function*.² Linear combinations of the kernel function form a *basis* set (not to be confused with the “basis” of crystallography) that forms an alternate, yet equally valid, expression for an arbitrary function. For the Fourier transform, the kernel function is the complex exponential and the basis set is formed from all possible frequencies, f . The Fourier transform and its analyzing function are:

$$\hat{g}(f) = \mathcal{F}[g(t)] = \int_{-\infty}^{\infty} \psi_f^*(t)g(t)dt \quad (2.1a)$$

$$\psi_f(t) = \exp(2\pi ift) \quad (2.1b)$$

¹ Another notable integral transform is the Laplace transform.

² The function used in the transformation may go by other names depending on the specific field of mathematics, science, or engineering.

where the asterisk (*) denotes the complex conjugate. The symbol ψ will be used to denote a kernel function and its subscripts give the transformed coordinates. So $\psi_f(t)$ transforms an arbitrary function of t , $g(t)$, to a function of f , $\hat{g}(f)$. The *hat* notation ($\hat{}$) signifies the Fourier transform of a function.

The wavelet transform has a form similar to Eq. 2.1. Instead of a complex exponential kernel function, the wavelet transform uses a localized wave, or wave-packet, with a mean of zero. There is no unique function that satisfies these criteria [91]. The Morlet wavelet [92] is perhaps one of the simplest choices for the kernel function. It has the form of a complex exponential in a Gaussian envelope:

$$\tilde{g}(t', f') = \mathcal{W}[g(t)] = \int_{-\infty}^{\infty} \psi_{t', f'}^*(t) g(t) dt \quad (2.2a)$$

$$\psi_{t', f'}(t) = \pi^{-\frac{1}{4}} \left(\frac{f'}{f_\psi} \right)^{\frac{1}{2}} \exp(2\pi i f' (t - t')) \exp\left(-\frac{1}{2} \left(\frac{f'}{f_\psi} \right)^2 (t - t')^2 \right) \quad (2.2b)$$

The variable f' is used instead of f because, as will be seen later, f' corresponds to a peak frequency and not an exact frequency. Whereas previous implementations of the Morlet wavelet have transformed the signal to a time-scale domain, where scale is related to the period of oscillation [92, 98], the Morlet wavelet as presented in Eq. 2.2b will convert the signal directly to the time-frequency domain, which eases the interpretation of the transformed signal in the context of nanoscale thermal transport. The connection between the two implementations is straightforward, requiring only the variable substitutions: $f' = \frac{k_\psi}{2\pi s}$ and $f_\psi = \frac{k_\psi}{2\pi}$, to use the notation from Baker *et al.* [98].

The special case $f' = f_\psi$ is called the *mother wavelet*. Derivatives of the mother wavelet, called *daughter wavelets*, are obtained by shifting and horizontally stretching or compressing the mother wavelet. The variable t' controls the peak location of the daughter wavelet and the variable f' controls its peak frequency. A mother wavelet with $f_\psi = 1$ is depicted in Figure 2.1 along with shifted, compressed, and stretched daughter wavelets. Also shown for reference is a sinusoid of $f = 1$. By compressing the mother wavelet by a factor of two, the peak frequency that it analyzes is doubled, and vice versa for stretching. From the definition of the mother wavelet, the parameter f_ψ determines the number of oscillations in each daughter wavelet.

The coefficients of Equation 2.2b normalize each daughter wavelet to ensure it has unit energy; that is:

$$\int_{-\infty}^{\infty} \psi_{t', f'}^* \psi_{t', f'} dt = 1 \quad (2.3)$$

Such a normalization is not required [90], although it is the most convenient for the physical applications detailed in this work.

The variables t' and f' have been used for the transformed coordinates instead of t and f because the wavelets used in the transform are extended in both time and frequency. As such, the signal amplitude at $\tilde{g}(t', f')$ also contains contributions from times $t' \pm \delta t$ and $f' \pm \delta f$ for some δt and δf . In other words, the wavelet transform is a little “blurry.” The Gaussian

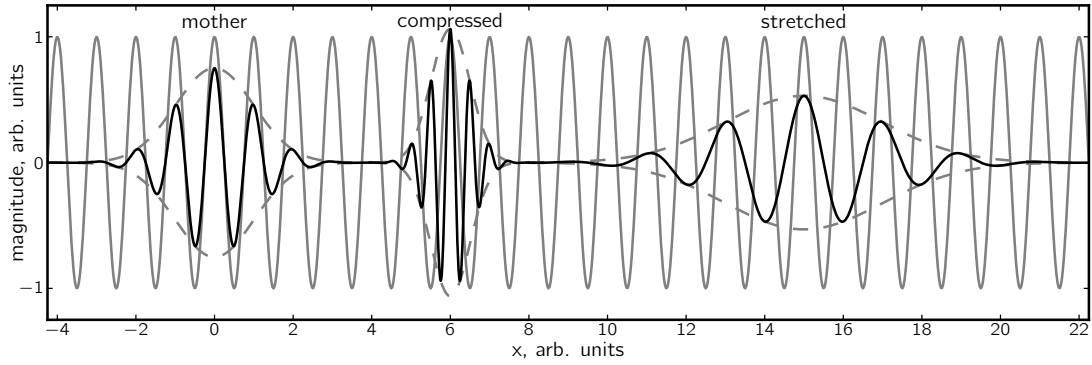


Figure 2.1: Real part of wavelets used to analyze a function compared to the kernel function of the Fourier transform. Analyzing wavelets are shifted and compressed or stretched copies of the mother wavelet.

envelope in Equation 2.2b causes the blurriness in time. It also indirectly causes the blurriness in frequency. Examining the frequency spectrum of $\psi_{t',f'}(t)$ shows why:

$$\hat{\psi}_{t',f'}(f) = \sqrt{2\pi}^{\frac{1}{4}} \left(\frac{f'}{f_\psi}\right)^{-\frac{1}{2}} \exp\left(-2\pi^2 \left(\frac{f'}{f_\psi}\right)^{-2} (f - f')^2\right). \quad (2.4)$$

Equation 2.4 is another Gaussian centered at the frequency, f' . Inspecting Eqs. 2.2b and 2.4 yields the widths of the two Gaussians:

$$\sigma_t = \frac{f_\psi}{f'}; \quad \sigma_f = \frac{1}{2\pi} \frac{f'}{f_\psi} \quad (2.5)$$

According to Equation 2.5, as the frequency, f' , of the analysis increases, time resolution improves but frequency resolution worsens, and vice versa. Notice that the product $\sigma_t \sigma_f$ is constant and equal to $1/2\pi$. This is analogous to the famous Heisenberg's uncertainty principle and occurs for the same reason! A wave's position and wavenumber cannot both be precisely known. Equation 2.5 also clarifies the role of f_ψ . It sets the reference point for the tradeoff between time and frequency resolution; increasing f_ψ improves frequency resolution for a given f' , but worsens the time resolution, and vice versa. The constraint that the mean of $\psi_{t',f'}(t)$ should be zero sets a lower limit on f_ψ of about 0.7, which gives the integral of the mother wavelet as $\left| \int_{-\infty}^{\infty} \text{Re} [\psi_{0,f_\psi}(t)] dt \right| \approx 10^{-4}$.

Since $\psi_{t',f'}(t)$ has finite widths in the time and frequency domains, f' cannot take on arbitrary values. Rather, the bounds of valid f' lie above zero and below the Nyquist frequency. The minimum f' is related to the duration of the signal, l_t . The total half-width of the wavelet might be conservatively defined as $3\sigma_t$. Then, at the frequency f' , the wavelet transform of the signal within $3\sigma_t$ of the beginning and end of the sampled time will be contaminated by edge artifacts. Defining ϕ as the fraction of the domain that is contaminated by edge artifacts at the minimum f' yields the relationship:

$$f'_{\min} = \frac{6f_\psi}{\phi l_t} \quad (2.6)$$

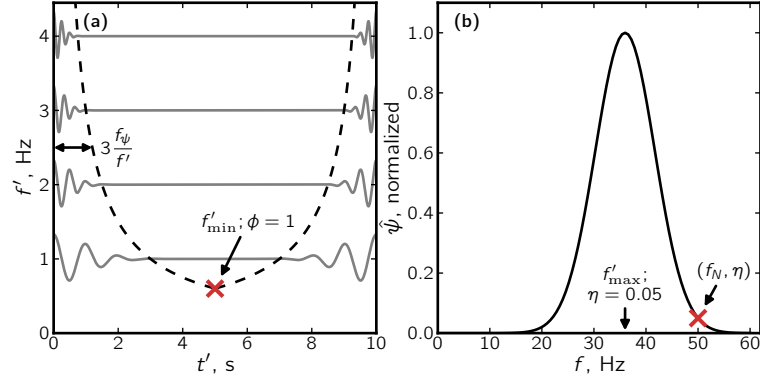


Figure 2.2: Determination of the minimum and maximum analyzable frequencies by the wavelet transform. (a) The minimum analyzable frequency is determined by the amount of edge artifacts allowed in the domain at the minimum analyzable frequency. The amplitude of the wavelets are shown to aid in the visualization. (b) The maximum analyzable frequency is determined by aliasing constraints. When the frequency spectrum of the analyzing wavelet goes past the Nyquist frequency, aliasing can occur. The parameter η is related to the amount of aliasing that is tolerated.

Figure 2.2a provides a visualization of how f'_{\min} is found. The area under the dashed curves is affected by edge artifacts, meaning that the wavelet signal, $\tilde{g}(t', f')$ is weighted by virtual zeros lying outside of the sampled region. If ϕ were greater than one, or the wavelet half-width was defined as significantly less than $3\sigma_t$ for $\phi=1$, then the wavelets used to analyze the beginning and end of the signal would overlap, or in the case of periodic boundary conditions, self-interfere.

The maximum analyzable frequency is determined by the condition of aliasing. Figure 2.2b illustrates this process. The frequency spectrum of the wavelet (Eq. 2.4) must decay to an acceptably small value by the Nyquist frequency, $f_N = \frac{1}{2\Delta t}$, where Δt is the sampling time of the signal. If η is the ratio $\hat{\psi}_{t', f'_{\max}}(f_N) / \hat{\psi}_{t', f'_{\max}}(f'_{\max})$, then, making use of Eq. 2.4, f'_{\max} is found to be:

$$\eta = \exp \left(-2\pi^2 \left(\frac{f'_{\max}}{f_{\psi}} \right)^{-2} \left(\frac{1}{2\Delta t} - f'_{\max} \right)^2 \right)$$

$$f'_{\max} = \left[2\Delta t \left(1 + \frac{1}{2\pi f_{\psi}} \sqrt{-2\ln(\eta)} \right) \right]^{-1} \quad (2.7)$$

One notable difference between the wavelet transform and the Fourier transform is that the basis functions of the wavelet transform are non-orthogonal. That is:

$$\int_{-\infty}^{\infty} \psi_{t', f'}^*(t) \psi_{t'', f''}(t) dt \neq 0; \quad \text{for } t' \neq t'' \text{ or } f' \neq f'' \quad (2.8)$$

The non-orthogonality of the wavelet basis set must be taken into account to perform the inverse transform or analyze the energy of the signal in the wavelet domain. The *admissibility constant* represents this accounting:

$$C = \int_{-\infty}^{\infty} \frac{|\hat{\psi}_{t', f_{\psi}}(f)|^2}{|f|} df \quad (2.9)$$

The inverse wavelet transform is then:

$$g(t) = \frac{1}{C_{f_\psi}} \int_{-\infty}^{\infty} \int_{-\infty}^{\infty} \psi_{t',f'}(t) \tilde{g}(t', f') dt' df' \quad (2.10)$$

By the Plancherel theorem [99, 100], also known as Rayleigh's theorem [88], the energy of the signal is conserved regardless of the domain:

$$\|g\|^2 = \int_{-\infty}^{\infty} |g(t)|^2 dt = \int_{-\infty}^{\infty} |\hat{g}(f)|^2 df = \frac{1}{C_{f_\psi}} \iint_{-\infty}^{\infty} |\tilde{g}(t', f')|^2 dt' df' \quad (2.11)$$

When interpreting the wavelet transform of a signal, it is useful to define the energy density, ρ , as:

$$\rho(t', f') = \frac{2}{C_{f_\psi}} |\tilde{g}(t', f')|^2 \quad (2.12)$$

The factor of two is to permit the integration of ρ over only positive frequencies when $g(t)$ is a real valued signal, in a procedure similar to that typically employed for the Fourier transform.

The wavelet transform may accommodate periodic boundary conditions. If the signal to be analyzed is periodic, then the calculation of the daughter wavelets, $\psi_{t',f'}(t^\circ)$, should be carried out for a periodic time variable, t° , as:

$$t^\circ = \begin{cases} t + l_t; & t < t' - \frac{l_t}{2} \\ t; & t' - \frac{l_t}{2} \leq t \leq t' + \frac{l_t}{2} \\ t - l_t; & t > t' + \frac{l_t}{2} \end{cases} \quad (2.13)$$

In the special case of a period signal, constant time sampling, and wavelet offset times, t' , equal to t , the wavelet transform may be efficiently computed using the convolution theorem [88]. Then the wavelet transform (Eq. 2.2) becomes:

$$\tilde{g}(t', f') = \mathcal{F}^{-1} \left[\hat{\psi}_{t',f'}(f) \mathcal{F}[g(t)] \right] \quad (2.14)$$

where \mathcal{F}^{-1} is the inverse Fourier transform. Equation 2.14 requires only two Fourier transforms (one being the inverse) for each f' to be analyzed. If using the Fast Fourier Transform [101] to evaluate Equation 2.14, it becomes orders of magnitude faster than using Equations 2.2 directly, which requires N'_t integrations over the whole time domain for each f' to be analyzed, where N'_t is the length of the vector containing the times t' to analyze. The main benefit of the direct evaluation of the wavelet transform, then, is that it can accommodate non-constant time sampling and t' values that lie between sampled time points. A signal can be buffered with a sufficient number of zeros³ to permit evaluation with Equation 2.14 without introducing an egregious amount of edge artifacts.

A demonstration of the wavelet transform on certain elementary functions is presented in Figure 2.3. A time signal consisting of the superposition of one delta function, two sine functions, and three wave-packet functions (Fig. 2.3a) is to be analyzed to find the parameters (times and frequencies) of each function. In the frequency domain (Fig. 2.3b), the delta function acts as a constant offset. The frequencies of the two sine functions may now be identified.

³ The buffer length should reach the next power of two for the signal length.

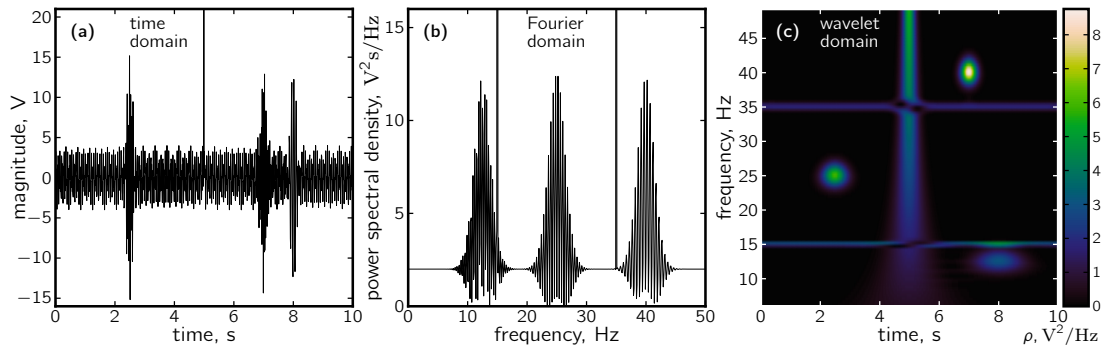


Figure 2.3: Analysis of elementary functions in the time, Fourier, and wavelet domains. (a) A signal comprising one delta function, two sine functions, and three wave-packet functions. The analyst may wish to know the times and frequencies associated with these events, for which he might use the Fourier transform or the wavelet transform. (b) The signals transformed into the Fourier domain. The frequencies of the sine functions and wave-packets may now be identified, but it is unknown which frequency belongs to which wave-packet. (c) The signal transformed into the wavelet domain. The locations and frequencies of each function are now unambiguously determined. The shapes of the energy distributions representing the functions also demonstrate the dependence of time and frequency uncertainty on the frequency.

Whereas the frequency spectrum of a wave-packet is a Gaussian, as was seen in Equation 2.4, in this example the wave-packets interfere with the delta function to produce the rapid oscillations seen here. Although the peak frequencies of the wave-packets may now be identified, it is impossible to determine which peak frequency corresponds to which wave-packet in Figure 2.3a since temporal information is not immediately available in the Fourier transform representation. In the wavelet domain (Fig. 2.3c), the peak times and frequencies of each wave-packet are readily identified. The time of the delta function and the frequencies of the sine functions are just as easily identified.

Examining Figure 2.3c shows the effect of the wavelet's time and frequency uncertainty (Eq. 2.5) on the resulting energy distribution. The delta function is wider at the bottom (low frequencies) than at the top. The higher frequency sine wave is more broadened than the other. And all three wave-packets, though defined using the same Gaussian envelope, are stretched or compressed in time and frequency to different degrees according to Equation 2.5. One last note on the interpretation of the wavelet energy density as depicted in Figure 2.3c: imagine you are a tiny person standing in the plane of the figure. If you are standing on the x-axis label ("time, s") and looking along the y-axis, you would see a cross-section of the energy landscape that resembled Figure 2.3a. Likewise, if you were to stand on the y-axis label and look along the x-axis, you would see a cross-section resembling Figure 2.3b. In this way, the wavelet transform contains information from both the time domain and the frequency domain and is a compromise between analysis of a signal in each.

2.2 CALCULATION OF THE VIBRATIONAL DENSITY OF STATES

As mentioned in Section 1.5, molecular dynamics simulations implicitly contain everything there is to know about the physics of vibrational transport in the system, including the vibrational density of states. A brief derivation and instructions for the calculation are given in Appendix F of Dove [29]. Even so, many steps are skipped and the exact details of the implementation and why the calculation works were not immediately apparent upon my first, or even second, reading. Whether a coincidence or not, many calculations of the vibrational density of states from a molecular dynamics simulation reported in the literature use “arbitrary units” instead of, for example, “states/(THz·nm³)” [102–108]. I believe that a more detailed derivation will reassure the interested simulationist that the “Fourier transform of the mass-weighted velocity autocorrelation function” [29] can indeed produce the correct density of states.

The following derivation of the density of states uses Dove’s notation and will reference equation numbers from the first edition of his book [29].⁴ This derivation was worked out with the aid of my colleague Nam Le, who deserves an equal share of the credit. It begins with Dove’s Equation F.10 and proceeds through Equation F.14.

The velocity, $\dot{\mathbf{u}}$, of the j th atom in the l th unit cell is (Dove Eq. F.10):

$$\dot{\mathbf{u}}(jl, t) = \frac{-i}{(Nm_j)^{1/2}} \sum_{\mathbf{k}, \nu} \omega(\mathbf{k}, \nu) \mathbf{e}(j, \mathbf{k}, \nu) \exp(i\mathbf{k} \cdot \mathbf{r}(jl)) Q(\mathbf{k}, \nu, t), \quad (2.15)$$

where N is the number of unit cells, m_j is the mass of the j th atom in the unit cell, \mathbf{k} is the angular wavevector, ν indexes the modes, \mathbf{r} is the position vector, \mathbf{e} is the mode eigenvector, and Q is the normal mode coordinate. Taking the inner product of the velocities at time t' and time $t' + t$ results in:

$$\begin{aligned} \dot{\mathbf{u}}(jl, t' + t) \cdot \dot{\mathbf{u}}(jl, t') &= \frac{-1}{Nm_j} \times \\ &\sum_{\mathbf{k}', \nu', \mathbf{k}, \nu} \omega(\mathbf{k}', \nu') \omega(\mathbf{k}, \nu) \mathbf{e}(j, \mathbf{k}', \nu') \cdot \mathbf{e}(j, \mathbf{k}, \nu) \exp(i(\mathbf{k}' + \mathbf{k}) \cdot \mathbf{r}(jl)) Q(\mathbf{k}', \nu', t' + t) Q(\mathbf{k}, \nu, t'), \end{aligned} \quad (2.16)$$

where the *primed* variables correspond to the state of the system at time $t' + t$ and the exponents have been combined.

From Dove Equation F.10 to F.11, he autocorrelates Equation 2.15 (an average of Eq. 2.16 over t'), multiplies by the mass, and sums over the atoms of the unit cell. Since autocorrelation is merely a sum over all t' , it can be freely rearranged with the summation over j and an average over l , resulting in (the autocorrelation and sum over j have not been performed yet):

⁴ Only the first edition exists as of the time this dissertation was written.

$$\begin{aligned} \frac{1}{N} \sum_l \dot{\mathbf{u}}(jl, t' + t) \cdot \dot{\mathbf{u}}(jl, t') &= \frac{-1}{N^2 m_j} \times \\ \sum_{\mathbf{k}', \nu', \mathbf{k}, \nu} \sum_l \omega(\mathbf{k}', \nu') \omega(\mathbf{k}, \nu) \mathbf{e}(j, \mathbf{k}', \nu') \cdot \mathbf{e}(j, \mathbf{k}, \nu) \exp(i(\mathbf{k}' + \mathbf{k}) \cdot \mathbf{r}(jl)) Q(\mathbf{k}', \nu', t' + t) Q(\mathbf{k}, \nu, t'). \end{aligned} \quad (2.17)$$

Now, using Dove Equation B.1:

$$\frac{1}{N} \sum_l \exp(i\mathbf{k} \cdot \mathbf{r}(l)) = \delta_{\mathbf{k}, 0}, \quad (2.18)$$

and breaking up the exponent of Equation 2.17 as:

$$\exp(i(\mathbf{k}' + \mathbf{k}) \cdot \mathbf{r}(jl)) = \exp(i(\mathbf{k}' + \mathbf{k}) \cdot \mathbf{r}(l)) \exp(i(\mathbf{k}' + \mathbf{k}) \cdot \mathbf{r}(j)), \quad (2.19)$$

where $\mathbf{r}(jl) = \mathbf{r}(l) + \mathbf{r}(j)$; the terms in Equation 2.17 with $\mathbf{k}' \neq -\mathbf{k}$ become zero, leaving:

$$\begin{aligned} \frac{1}{N} \sum_l \dot{\mathbf{u}}(jl, t' + t) \cdot \dot{\mathbf{u}}(jl, t') &= \frac{-1}{N m_j} \times \\ \sum_{\mathbf{k}, \nu', \nu} \omega(-\mathbf{k}, \nu') \omega(\mathbf{k}, \nu) \mathbf{e}(j, -\mathbf{k}, \nu') \cdot \mathbf{e}(j, \mathbf{k}, \nu) Q(-\mathbf{k}, \nu', t' + t) Q(\mathbf{k}, \nu, t'). \end{aligned} \quad (2.20)$$

Multiplying Equation 2.20 by m_j , summing over j , and rearranging leads to:

$$\begin{aligned} \frac{1}{N} \sum_{jl} m_j \dot{\mathbf{u}}(jl, t' + t) \cdot \dot{\mathbf{u}}(jl, t') &= \frac{-1}{N} \times \\ \sum_{\mathbf{k}, \nu', \nu} \omega(-\mathbf{k}, \nu') \omega(\mathbf{k}, \nu) Q(-\mathbf{k}, \nu', t' + t) Q(\mathbf{k}, \nu, t') \sum_j \mathbf{e}(j, -\mathbf{k}, \nu') \cdot \mathbf{e}(j, \mathbf{k}, \nu). \end{aligned} \quad (2.21)$$

Again, with help from Dove Equation 4.6:

$$\sum_j \mathbf{e}(j, -\mathbf{k}, \nu') \cdot \mathbf{e}(j, \mathbf{k}, \nu) = \delta_{\nu', \nu}, \quad (2.22)$$

the terms in Equation 2.21 with $\nu' \neq \nu$ become zero, leaving:

$$\frac{1}{N} \sum_{jl} m_j \dot{\mathbf{u}}(jl, t' + t) \cdot \dot{\mathbf{u}}(jl, t') = \frac{-1}{N} \sum_{\mathbf{k}, \nu} \omega^2(\mathbf{k}, \nu) Q(-\mathbf{k}, \nu, t' + t) Q(\mathbf{k}, \nu, t'). \quad (2.23)$$

The even symmetry of the Brillouin Zone has been used to combine the terms $\omega(\mathbf{k}, \nu) \omega(-\mathbf{k}, \nu)$.

The autocorrelation of a time dependent function, $x(t)$, may be defined as:

$$\langle x(t)x(0) \rangle = \lim_{t_f \rightarrow \infty} \frac{1}{t_f} \int_0^{t_f} x(t' + t)x(t') dt', \quad (2.24)$$

which differs slightly from Dove Equation F.2, not being normalized to one at $t = 0$. The autocorrelation can also be thought of as the expectation value of the quantity $x(t' + t)x(t')$. Completing the autocorrelation of Equation 2.23 and canceling factors of N yields:

$$\sum_{jl} m_j \langle \dot{\mathbf{u}}(jl, t) \cdot \dot{\mathbf{u}}(jl, 0) \rangle = - \sum_{\mathbf{k}, \nu} \omega^2(\mathbf{k}, \nu) \langle Q(-\mathbf{k}, \nu, t) Q(\mathbf{k}, \nu, 0) \rangle. \quad (2.25)$$

Equation 2.25 is similar to, but not quite the same as, Dove Equation F.11. The differences are that we did not take the magnitude of the velocity inner product, leading to the negative sign on the right hand side. Also, we have explicitly summed over the atoms in the unit cell and averaged over all unit cells, causing the factors of N to cancel.

Going from Equation 2.25 to Dove Equation F.14 also requires several steps. By comparing Dove Equations 4.1 and 4.2, the normal mode coordinate evidently has the form:

$$Q(\mathbf{k}, \nu, t) \propto \exp(-i\omega t). \quad (2.26)$$

Along with Dove Equation 4.3, the following relations arise:

$$Q(-\mathbf{k}, \nu, t' + t) = Q^*(\mathbf{k}, \nu, t' + t) \propto \exp(i\omega t') \exp(i\omega t); \quad Q(\mathbf{k}, \nu, t') \propto \exp(-i\omega t'). \quad (2.27)$$

So the argument of the autocorrelation on the right hand side of Equation 2.25 is:

$$Q(-\mathbf{k}, \nu, t' + t) Q(\mathbf{k}, \nu, t') = |Q(\mathbf{k}, \nu, t')|^2 \exp(i\omega t). \quad (2.28)$$

Completing the autocorrelation of both sides, which is again merely averaging over all t' , gives a result analogous to Dove Equation F.12:

$$\langle Q(-\mathbf{k}, \nu, t) Q(\mathbf{k}, \nu, 0) \rangle = \langle |Q(\mathbf{k}, \nu, 0)|^2 \rangle \exp(i\omega t). \quad (2.29)$$

Substituting Dove Equation 4.19 into Equation 2.29 gives a result analogous to Dove Equation F.13:

$$\langle Q(-\mathbf{k}, \nu, t) Q(\mathbf{k}, \nu, 0) \rangle = \frac{k_B T}{\omega^2} \exp(i\omega t). \quad (2.30)$$

Plugging Equation 2.30 into Equation 2.25 yields:

$$\sum_{jl} m_j \langle \dot{\mathbf{u}}(jl, t) \cdot \dot{\mathbf{u}}(jl, 0) \rangle = -k_B T \sum_{\mathbf{k}, \nu} \exp(i\omega t). \quad (2.31)$$

Finally, taking the Fourier transform of both sides gives:

$$\int_{-\infty}^{\infty} \exp(-i\omega' t) \sum_{jl} m_j \langle \dot{\mathbf{u}}(jl, t) \cdot \dot{\mathbf{u}}(jl, 0) \rangle dt = -k_B T \sum_{\mathbf{k}, \nu} \int_{-\infty}^{\infty} \exp(i\omega t) \exp(-i\omega' t) dt; \quad (2.32)$$

the right hand side simplifies, giving the analog to Dove Equation F.14:

$$- \frac{1}{k_B T} \int_{-\infty}^{\infty} \exp(-i\omega' t) \sum_{jl} m_j \langle \dot{\mathbf{u}}(jl, t) \cdot \dot{\mathbf{u}}(jl, 0) \rangle dt = \sum_{\mathbf{k}, \nu} \delta_{\omega', \omega(\mathbf{k}, \nu)}. \quad (2.33)$$

The summation on the right hand side counts the number of modes with an angular frequency ω' . The negative sign on the left hand side is apparently erroneous and should be ignored; I have been unable to determine the step in the derivation at which it should be canceled. Remember that implicit in the autocorrelation function is a division by the duration of the signal, t_f . Otherwise, the calculated density of states would scale with the simulation time. Since the simulation must be of a finite duration and time step, the frequency resolution of the density of states is $\frac{1}{N_t \Delta t}$, where N_t is the number of points in the time series of $\dot{\mathbf{u}}$ and Δt is the printing period of the atomic velocities, which should be a multiple of the simulation time step. Dividing Equation 2.33 by the domain volume yields the density of states in the familiar units of *states per angular frequency per volume*. The “local density of states” is often calculated in molecular dynamics simulations as a measure of the local phonon population [108]. In this case, the volume to divide by is the one that encompasses the atoms included in the summation over l and j .

The density of states may be efficiently calculated with the help of the Wiener-Khinchin theorem [88]. It states that the Fourier transform of the autocorrelation function of a signal is equal to the squared magnitude of the Fourier transform of that same signal. Then, Equation 2.33 becomes:

$$g(\omega) = \frac{2}{k_B T V t_f} \sum_{j,l,\alpha} m_j |\mathcal{F}(\dot{u}(jl, \alpha, t))|^2, \quad (2.34)$$

where $g(\omega)$ is the density of states with units *states per angular frequency per volume*, and α indexes the cartesian coordinates of $\dot{\mathbf{u}}$. The summation over α accounts for the inner product in Equation 2.33. The factor of two accounts for the spectral energy contained in the negative frequencies so that $g(\omega)$ can be analyzed entirely in the positive frequency domain. For Equations 2.33 and 2.34, performing a linear Fourier transform (Eq. 2.1) gives the density of states with respect to linear frequency. The success of the calculation should be verified by comparing the integral over the positive frequencies of $g(\omega)$ to the classical value of $\frac{3N}{V}$, where N is the number of atoms.

2.3 CONSTRUCTING ALLOYS WITH VARIABLE LONG- AND SHORT-RANGE ORDER

An alloy is defined microscopically by its lattice structure, the number of constituent elements, the concentration of each element, the long-range order parameter, and the short-range order parameter for every possible neighbor distance. The long-range order parameter gives probability of finding a certain element on the same lattice site for every unit cell. The long-range order parameter ranges from zero, for a completely disordered structure, to one, for a completely ordered structure, *i.e.* one with an identical basis group of atoms occupying every lattice site. There are different ways to numerically define the short-range order, but they each measure the probability of finding ordered pairs of atoms over length scales given by interatomic neighbor distances. The short-range order may also be considered as a distance-

dependent correlation of atoms composing the structure. A short-range order parameter of zero for some distance means that atoms separated by that distance are completely uncorrelated. Simulation offers the capability to exactly control each parameter of the alloy. This section outlines the procedure for generating binary alloys with the long-range order and nearest-neighbor short-range order parameters precisely controlled. Although a binary alloy consists of two elements, ternary or higher alloys for which only two elements display disorder on their own sub-lattice may also be generated by the procedure outlined in this section.

2.3.1 Long-Range Order

Creating an alloy of a given composition and long-range order proceeds directly from the definition of the long-range order. Bragg and Williams were the first to give a general theoretical treatment of the long-range order of an alloy [40]. They defined the long-range order parameter, \mathbb{L} , of a binary alloy, $A_{1-x}B_x$, as:

$$\mathbb{L} = \frac{p - r}{1 - r}, \quad (2.35)$$

where p is the probability of finding an atom of element A occupying its correct lattice site, and r is the fraction of lattice sites populated by atoms of element A in the ordered structure with respect to the number of lattice sites eligible for a disordering substitution. This last point warrants comment. In an alloy of a given composition, the case may be that certain atoms will always remain in their positions, resisting substitution by another element. Such atoms do not contribute to the calculation of the order parameter. Bragg and Williams give Fe_3Al as an example of such an alloy: in its fully disordered state, Fe atoms occupy the corners of a body-centered cubic lattice and the central atom has a 50% chance of being Fe and a 50% chance of being Al [40].

The application of Equation 2.35 will be examined with Bragg and Williams's Cu_3Au as an example [40, 42]. Cu_3Au orders into a simple cubic lattice, where the Au atom occupies the origin, and the three Cu atoms occupy what would be the face sites of the face-centered cubic unit cell. Every lattice site is eligible for a disordering substitution.

Consider a Cu_3Au alloy with a long-range order parameter of $\frac{1}{2}$. The basis sites of the structure might be labeled zero to three, with site 0 at the origin of the unit cell and sites 1, 2, and 3 at the faces. From Equation 2.35, we have:

$$\frac{1}{2} = \frac{p_{\text{Au},0} - \frac{1}{4}}{1 - \frac{1}{4}} \quad (2.36)$$

where $p_{\text{Au},0}$ is the probability of a Au atom occupying site 0. Solving gives $p_{\text{Au},0} = \frac{5}{8}$. The probability of finding an atom at site 0, regardless of the element, is one. So by necessity, $p_{\text{Cu},0} = 1 - p_{\text{Au},0} = \frac{3}{8}$. Since the number of atoms of each element is fixed, $p_{\text{Au},1} = p_{\text{Au},2} = p_{\text{Au},3} = \frac{1 - p_{\text{Au},0}}{3} = \frac{1}{8}$ and $p_{\text{Cu},1} = p_{\text{Cu},2} = p_{\text{Cu},3} = \frac{3 - p_{\text{Cu},0}}{3} = \frac{7}{8}$.

The same result may be obtained by performing the calculation from the perspective of the Cu atoms. In other words, the minority element is not privileged:

$$\frac{1}{2} = \frac{p_{\text{Cu},1} - \frac{3}{4}}{1 - \frac{3}{4}}; \quad p_{\text{Cu},1} = \frac{7}{8} \quad (2.37)$$

The procedure for generating a Cu_3Au structure with arbitrary long-range order is then:

1. Begin with the ordered Cu_3Au structure.
2. Select a fraction of Au sites equal to $(1 - \mathbb{L})(1 - r_{\text{Au}})$ to substitute with a Cu atom.
3. Select a fraction of Cu sites equal to $(1 - \mathbb{L})(1 - r_{\text{Cu}})$ to substitute with a Au atom.
4. Do the substitutions.

Steps 2 and 3 guarantee that the composition is conserved. Note that for very small system sizes, the possible \mathbb{L} values are limited by the necessity that the fraction of Au atoms to switch multiplied by the number of unit cells in the system must be a whole number. Even so, the above approach has the benefit of resulting in a structure where \mathbb{L} is exactly as desired, regardless of the system size. At this point, the short-range order, to be discussed in Section 2.3.2, is *approximately equal to \mathbb{L} for all neighbor distances*.

The above approach is preferable to an alternate approach for structure generation: assigning a Au atom to site i with probability $p_{\text{Au},i}$ and a Cu atom to site i with probability $p_{\text{Cu},i}$, as in Equation 2.35. Then, after assigning an atom to each lattice site, the composition may be slightly different from that desired.

In the special case of a binary alloy with equal concentrations of A and B atoms, where every lattice site is eligible for a disordering substitution, the calculation of \mathbb{L} in Equation 2.35 may be simplified as [109]:

$$\mathbb{L} = \frac{|R - W|}{N} \quad (2.38)$$

where R is the number of atoms occupying the “right” lattice site with respect to the ordered structure, W is the number of atoms occupying the “wrong” lattice site, and N is the total number of atoms. Of course, $R + W = N$, and the same method listed above may be used to generate the structure. Without the absolute value in Equation 2.38, if there were more atoms in “wrong” positions than “right,” then \mathbb{L} would be negative. But, without loss of generality, the ordering of such a structure could be evaluated with respect to a shifted lattice, in which case “wrong” atoms become “right” atoms and vice versa, yielding a positive \mathbb{L} . Since allowing \mathbb{L} to be negative gives no physical insight, and indeed would likely cause confusion, the absolute value gives the correct result whether the underlying reference lattice should be shifted or not.

2.3.2 Short-Range Order

The short-range order of an alloy may be defined by the Warren-Cowley short-range order parameters [41]. The central idea is that the degree of order is not defined with respect to a lattice site, as is the case for the long-range order, but rather it is defined with respect to the neighbors surrounding an atom. There is a different short-range order parameter for each neighbor shell, indexed by i . Again, the short-range order parameter for a shell i measures the correlation between the identity of an atom and the identities of the atoms in its i th neighbor shell.

The Warren-Cowley short-range order parameters of an $A_{1-x}B_x$ alloy are defined as [41]:

$$\alpha_i = 1 - \frac{n_{i,A}}{c_A n_i} \quad (2.39)$$

where i indexes the neighbor shells of a B atom, $n_{i,A}$ is the number of A atoms in the i th neighbor shell, c_A is the concentration of A atoms in the alloy, and n_i is the total number of atoms in the i th neighbor shell. Using the example of Cu_3Au again, for the perfectly ordered structure, $\alpha_i = 1$ for even i and $\alpha_i = -\frac{1}{3}$ for odd i [41]. In fact, for a structure with any \mathbb{L} , the even and odd neighbor shell order parameters converge to different values.

The convergence of the short-range order parameter to different values depending on the parity of the neighbor shell is undesirable, as is the dependence of Equation 2.39 on which element is taken as the reference. A different formulation may be defined such that, like the long-range order parameter, the short-range order parameter is independent of the choice of reference element and neighbor shell parity.

Consider a simple alloy where each neighbor shell of a given atom contains only one element in the ordered structure, and the concentration of each element is $\frac{1}{2}$. An example is an alloy that orders in the zincblende structure. Then, instead of Equation 2.39, a short-range order parameter may be defined in the style of the long-range order (Eq. 2.35) for each shell that depends on the composition of that shell in the ordered structure:

$$\alpha_i = \frac{\frac{n_{i,A|B}}{n_i} - r_{A|B}}{1 - r_{A|B}} \quad (2.40)$$

where $n_{i,A}$ or $n_{i,B}$ and r_A or r_B are selected based on the identity of the central atom and whether its neighbors in shell i are all A or B atoms in the ordered structure. Taking $\text{Si}_{0.5}\text{Ge}_{0.5}$ as an example and zincblende as the ordered structure, suppose that an arbitrary atom were chosen and it happened to be a Si atom. Whether that Si atom is at the “right” lattice site or not is irrelevant to the calculation of α_i . Examining its four nearest neighbors, if three are Ge and one is Si, then

$$\alpha_1 = \frac{\frac{3}{4} - \frac{1}{2}}{1 - \frac{1}{2}} = \frac{1}{2}. \quad (2.41)$$

Averaging over all possible central atoms gives the average short-range order parameter of the whole system. Since the computation of Equation 2.40 for all i scales with N^2 , it is sufficient to take the average over a subset of atoms for a very large system.

In Equation 2.40, as i approaches infinity, the limiting value is related to the long-range order [41]. The relationship for a binary alloy with an equal number of A and B atoms is: $\lim_{i \rightarrow \infty} \alpha_i = \mathbb{L}^2$. It is therefore convenient to define a new short-range order parameter, $S_i = \sqrt{\alpha_i}$ so that $\lim_{i \rightarrow \infty} S_i = \mathbb{L}$. As with the long-range order (Eq. 2.38), an alloy with equal numbers of A and B atoms, where every lattice site is eligible for a disordering substitution and each neighbor shell of the ordered structure contains only one element, simplifies the expression for S_i as [109]:

$$S_i = \sqrt{\frac{R_i - W_i}{N_i}} \quad (2.42)$$

where R_i is the number of “right” neighbors in neighbor shell i , W_i is the number of “wrong” neighbors in neighbor shell i , and N_i is the total number of neighbors in neighbor shell i .

For an alloy with a fixed composition and long-range order, the short-range order may be efficiently manipulated through a Monte Carlo approach. After the long-range order of the structure is defined as in Section 2.3.1, S_i is approximately equal to \mathbb{L} for all i . Then, each Monte Carlo step consists of:

1. Select an atom that occupies the right lattice site.
2. Select an atom of the opposite element that occupies the wrong lattice site.
3. Exchange the two atoms. This preserves the total number of atoms of each type and the long-range order.
4. Recalculate the short-range order and accept the exchange if it brought the short-range order closer to the desired value.

Since the short-range order is defined using a square-root, for small \mathbb{L} , it is possible that Equation 2.42 produces an imaginary value. This poses no theoretical difficulty, as it means that the numerator of Equation 2.42 happens to be negative, which it will be as often as not for the initial structure corresponding to $\mathbb{L} = 0$. As such, the magnitude of S_i is the physically relevant value.

Practically, this possibility must be considered in Step 4 above, when the comparison is made to the desired short-range order parameter. This is done by letting the difference between the current short-range order and the desired short-range order, S'_i , be:

$$S'_i - S_i = \begin{cases} S'_i - S_i & \text{Im}(S_i) = 0 \\ (S_i'^2 + |S_i|^2)^{\frac{1}{2}} & \text{Re}(S_i) = 0 \end{cases} \quad (2.43)$$

The order parameter may be efficiently computed at each step by keeping a tally of the total number of “right” and “wrong” neighbors in the entire system. Combined with a neighbor list, the total count of correct neighbors predictably changes with each Monte-Carlo step. Such

accounting is necessary for simulations containing perhaps a thousand atoms or more. Otherwise, looping through every atom for every Monte Carlo step to calculate the short-range order becomes prohibitively expensive.

The method presented in this section for constructing simulated binary alloys with the short-range order decoupled from the long-range order allows the effects of each on the thermal conductivity, and other properties, to be investigated. Such an investigation is presented in Chapter 5 for a $\text{Si}_{0.5}\text{Ge}_{0.5}$ alloy.

2.4 CONTRIBUTIONS

Although my presentation of the wavelet transform in Section 2.1 follows, and was inspired by, those of previous authors [90, 91, 97, 98], I have not previously encountered a presentation and discussion of this variant of the transform. That is, a version of the wavelet transform that directly gives the frequencies present in a signal (f'), instead of the “scale,” with no further need of manipulation. From the perspective of molecular dynamics simulation and nanoscale thermal transport, such a transformation is more naturally intuitive and therefore superior to the one detailed in my previous work [98]. Even so, my research represents the first systematic and general presentation of the wavelet transform as it applies to molecular dynamics simulations of nanoscale thermal transport. As will be seen in Chapters 3 and 6, the wavelet transform has great potential for investigating the fundamental physics underlying thermal transport by atomic vibrations.

The use of arbitrary units to express the density of states obtained by molecular dynamics simulations by many authors makes direct comparison to theoretical density of states tenuous. I was unable to find a detailed derivation when preparing this dissertation, and I suspect that others experience similar trouble. By providing what I believe to be Dove’s intermediate steps in the derivation, it is my hope that this contribution by Nam Le and myself (Sec. 2.2) will lead to more plots of the density of states in terms of “states/(THz·m³),” instead of “arbitrary units,” appearing in future journal articles.

Lastly, in Section 2.3, I provided an overview of long- and short-range order in alloys and worked some practical examples. Whereas an understanding of the definition of long-range order naturally leads to the method for constructing alloys with a specific composition and long-range order in simulations, the method to tune the short-range order is not so obvious. By describing an approach to decoupling the short-range order from the long-range order, other researchers might more easily investigate the effects of binary alloy ordering on the material properties.

3

LEVERAGING THE WAVELET TRANSFORM IN MOLECULAR DYNAMICS SIMULATIONS

The wavelet transform was presented in Section 2.1 as an analysis tool that yields simultaneous time and frequency information regarding the energy distribution of a time-dependent signal. The transform may equally be applied to space-dependent signals to yield simultaneous space and wavenumber information. Thermal transport in semiconducting solids is almost entirely due to vibrating atoms: vibrations that occur at certain times and places within the solid, and characterized by certain frequencies and wavenumbers. The wavelet transform can therefore be used to investigate the vibrational dynamics near an interface or within a disordered material. The purpose of this chapter is to describe the application of the wavelet transform to three types of molecular dynamics simulations: wave-packet study of interface transmissivity [110], steady-state non-equilibrium transport across an interface to measure thermal boundary conductance [103], and transient decay of a localized heating event [96]. The primary goal is to instill a sense of the capabilities of the wavelet transform as it pertains to molecular dynamics simulation of thermal transport. Quantitative results will be discussed only briefly, if at all.

3.1 WAVE-PACKET SIMULATIONS OF INTERFACES AND ANHARMONIC SCATTERING

In the wave-packet method, a localized packet of vibrational energy is constructed within a simulated crystal and “fired” at the interface [110]. The *wave-packet* approximates a phonon. By tracking the energy of the wave-packet before and after a scattering event with an interface, the interface transmissivity can be calculated, perhaps for use in a model of thermal boundary conductance [111–113]. Wave-packet simulations have been used to study such varied material systems as: epitaxial semiconductor interfaces [110], textured semiconductor interfaces [114], silicon-to-carbon nanotube interfaces [115], self-assembled monolayer interfaces [116], thermal rectification [117], and thin films [118].

The aforementioned research, and other studies using the technique, have focused on the simulation of one incident wave-packet at a time (although simulations with multiple wave packets are possible [119]) in a zero Kelvin system, where the transmission is determined by summing the kinetic and potential energies on either side of the interface after the wave-packet scattering process completes. A limitation of this approach is that it is unable to capture the

mechanisms of the energy transfer during the time the packet interacts with the interface due to the nonequilibrium, non-steady-state, and especially, localized nature of the process. Enabled by the wavelet transform, understanding the mechanisms by which the features of an interface affect the phonon transport will aid in the prediction of thermal boundary conductance of “non-ideal” interfaces [113] encountered in countless technologies.

A description of the wave-packet method follows. Consider a simulation domain that is very long in the z -direction compared to its cross-section. An interface separating two materials, A and B, exists somewhere in the middle of the domain with its unit normal vector parallel to the z -direction. Beginning from the ground state of the system, a wave-packet can be constructed in material A using the following position and velocity relations:

$$\mathbf{u}(z) = \text{Re} \left\{ A \mathbf{e}(k_p) \exp[2\pi i(k_p(z - z_p) - f_p t)] \exp \left[-\frac{1}{2} \left(\frac{z - z_p}{\sigma} \right)^2 \right] \right\} \quad (3.1)$$

and

$$\dot{\mathbf{u}}(z) = \text{Re} \left\{ -2\pi i f_p A \mathbf{e}(k_p) \exp[2\pi i(k_p(z - z_p) - f_p t)] \exp \left[-\frac{1}{2} \left(\frac{z - z_p}{\sigma} \right)^2 \right] \right\} \quad (3.2)$$

where A is the amplitude of the wave-packet, k_p is the peak wavenumber, $\mathbf{e}(k_p)$ is the mode eigenvector associated with k_p , z_p is the peak position, f_p is the mode frequency, and σ is the packet width. The phonon mode selected for the wave-packet study should have a direction of propagation parallel to the z -direction, and may have any polarization, *e.g.* longitudinal acoustic or transverse optical polarizations. It is convenient for the start of the simulation to coincide with a time $t = 0$. The time component was included in Equation 3.1 because it is necessary for deriving $\dot{\mathbf{u}}$, which is merely $\partial \mathbf{u} / \partial t$. The amplitude should be much less than the nearest neighbor distance if the simulation is to be harmonic. The wave-packet σ also controls the width in the wavenumber domain. The larger σ is, the more localized in k -space the wave-packet will be. This can also be seen in the Morlet wavelet (Eqs. 2.2b and 2.4).

With the atomic displacements and velocities defined by Equations 3.1 and 3.2, the wave-packet will propagate in the positive z -direction once the simulation begins. In order for the simulation to be analyzed by the wavelet transform, a one-dimensional signal must be generated from the simulation. This can be done by summing the displacements or velocities of the atoms in primitive cells sharing the same z coordinate:

$$u(z) = \sum_{jl} [\mathbf{u}(jl) \cdot \mathbf{e}(j)] \delta_{z,z_l} \quad (3.3)$$

where $\mathbf{u}(jl)$ is the displacement of the j th atom of the l th primitive cell and $\mathbf{e}(j)$ is the polarization vector of the j th atom for a phonon branch whose propagation direction is collinear with the z -direction. The delta function sums only those primitive cells that share a location in the z -direction.

Table 3.1: Wave-packet energy over time (Fig. 3.1) and its distribution among k_p , $2k_p$, and $>2k_p$ modes. The total energy decreases as energy scatters into modes lower than k_p or different polarizations.

Time (ps)	Energy (nm ³)	k_p (%)	$2k_p$ (%)	$>2k_p$ (%)
0.00	869.6	99.8	0.2	0.0
4.00	602.3	95.0	3.4	1.6
8.75	215.6	86.3	4.4	9.3
20.00	120.4	47.0	6.6	46.4

3.1.1 Anharmonic scattering of a wave-packet

Sinha *et al.* [120] used the wave-packet method to investigate the decay of phonons generated at transistor hotspots. The authors set the amplitude, A , of the wave-packet to a value large enough that it experienced the anharmonic terms of the interatomic potential. Energy from the wave-packet subsequently scattered into different modes, characterized by a relaxation time. A similar system was investigated using the wavelet transform in Figure 3.1 [98]. The displacements of the atoms along the z -direction were converted to a one-dimensional signal by Equation 3.3 and then wavelet transformed for successive time steps. The wavelet transform provides details regarding the amount of energy scattered from the initial wavenumber, and the “shape” of the phonon as time progresses. Three-phonon scattering redistributes energy into the $2k_p$ mode by 4 ps. Energy then scatters into large wavenumber modes before “drifting” back down and becoming more diffuse by 20 ps. Table 3.1 gives the distribution of energy among wavenumber bins over time. Here, the energy does not have a strict physical interpretation, but corresponds to the squared displacement of the atoms. The total amount of energy decreases as energy scatters into different polarizations or beyond the wavenumbers analyzable by the wavelet transform (Eqs. 2.6 and 2.7). Energy scattered into different polarizations can no longer be accounted for because Equation 3.3 selects only one polarization to create the one-dimensional signal.

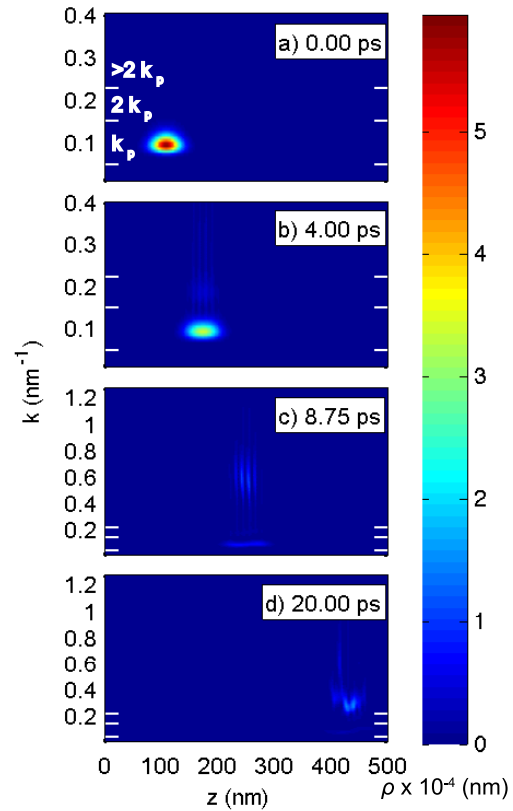


Figure 3.1: Anharmonic breakdown of a wave-packet viewed using the wavelet transform. Hash marks delineate regions of energy summation (Table 3.1). Three-phonon scattering redistributes energy into the $2k_p$ mode by 4 ps. The wavelet transform gives the “shape” of the energy distribution as energy scatters into large wavenumber modes then “drifts” back down and becomes more diffuse by 20 ps.

3.1.2 Wave-packet studies of interface transmission

The example of anharmonic wave-packet scattering occurred in a homogeneous crystal. Consider now a system of two materials joined at a planar interface. Suppose that the researcher wanted to investigate the interaction of phonons at the interface in this heterogeneous system. If there are many wave-packets present in the system, at different locations and with different wavenumbers, the filtering ability of the wavelet transform, as was seen in Figure 2.3, may be used to isolate and observe the dynamics of individual wave-packets. As an example, Figure 3.2 depicts a multiple wave-packet simulation where one wave-packet of interest (which is boxed) scatters with the interface in the presence of the others [98]. Calculating the transmissivity in the normal way, by summing the potential and kinetic energy on both sides before and after the scattering event [110] will not work because of the presence of the other wave-packets. But in the wavelet domain, the calculation of the transmissivity is straightforward: simply calculate the incident energy and reflected energy of the wave-packet, *i.e.* within the boxed regions of Figures 3.2a and 3.2d [98].

For an interfacial system where the two materials differ only by their masses, the case of a non-planar interface may easily be accommodated by the wave-packet simulation method and wavelet transform analysis. Four examples of non-planar interfaces are depicted in Figure 3.3, their goal being to emulate different aspects of a non-ideal interface, primarily the possibility of interdiffusion of the atomic species and interface roughness. In each case, the extent of the interface is 10 nm, that is, the influence of the interface does not extend more than 5 nm into each material on a side. The atoms of the right-hand material (cyan) are heavier than the atoms of the left-hand material (brown).

The first interface is defined by an $A_{0.5}B_{0.5}$ alloyed region 10 nm in thickness (Fig. 3.3a). The second interface also exhibits “interdiffusion,” but instead of an abrupt change in composition, there is a smooth grading of the composition defined by the log-normal Laplace distribution [108] (Fig. 3.3b). The sawtooth interface exhibits a sharp change in composition, but is geometrically rough (Fig. 3.3c). Finally, the sinusoidal interface also has an abrupt change in composition and geometric roughness, but with a different symmetry from the sawtooth interface (Fig. 3.3d).

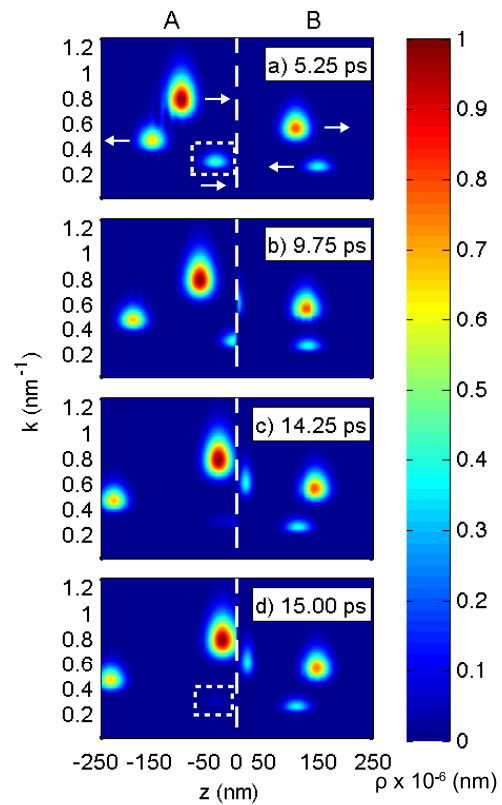


Figure 3.2: Wavelet transform of a multiple wave-packet simulation. The box indicates a hypothetical wave-packet of interest. The propagation directions of the wave-packets are indicated.

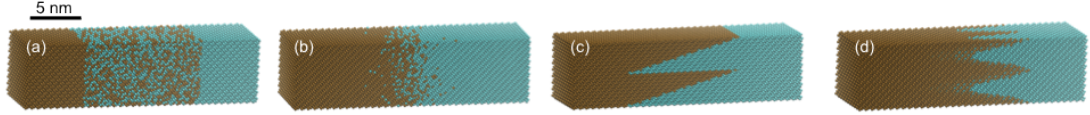


Figure 3.3: A series of non-ideal interfaces. Each interface has a transition region 10 nm in length. (a) The interface region is itself an equimolar alloy of the two materials. (b) Chemically graded interface. (c) Sawtooth interface. (d) Sinusoidal interface.

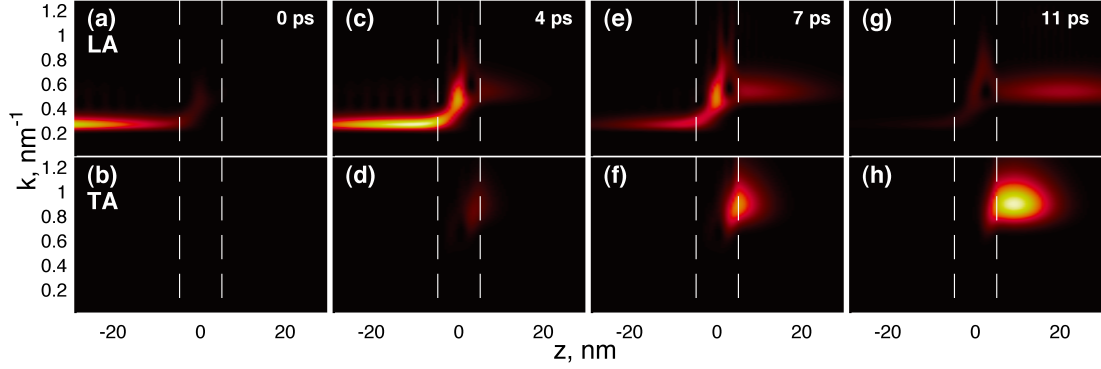


Figure 3.4: Wavelet visualization of a longitudinal acoustic (LA) phonon with a wavenumber of 0.26 nm^{-1} incident on a sawtooth interface (Fig. 3.3c). Panels a, c, e, and g track energy distribution in the LA mode and panels b, d, f, and h track the energy distribution in one of the TA modes. Dashed lines demarcate the extent of the interfacial region.

Performing wave-packet simulations on all four interfaces, with phonon wavenumbers of approximately 0.10 , 0.26 , and 0.55 nm^{-1} , elucidates the role of incident phonon wavelength compared to the length scale of the interface. In keeping with the objective of this chapter, the findings will be summarized and the case of a 0.26 nm^{-1} longitudinal wave-packet incident on the sawtooth interface will be discussed in more depth. The 0.10 nm^{-1} wave-packets scatter with each interface in much the same way, since their wavelength of 10 nm is equal to or greater than the length scales of the interfaces. The 0.55 nm^{-1} wave-packets are affected more by the interface because their wavelength of $\sim 1.8 \text{ nm}$ is smaller than the length scale of the interface. These wave-packets are able to transmit some energy across the sawtooth and sinusoidal interfaces but unable to transmit energy across the alloyed and chemically graded interfaces. This is because the mixed regions of these two interfaces had no available intermediate states for the wave-packet to scatter into before fully crossing the interface.

The 0.26 nm^{-1} wave-packets have wavelengths of $\sim 3.8 \text{ nm}$, which is on the order of the interface length scales, leading to interesting effects not seen for the other wavenumbers. Figure 3.4 shows a 0.26 nm^{-1} longitudinal acoustic (LA) wave-packet scatter with the sawtooth interface. As the wave-packet crosses the interface into the heavier material, it increases in wavenumber according to the greater acoustic impedance of that material (Figures 3.4a,c,e,g). But when the wave-packet is about 2.5 nm into material B, some of its energy is converted to a transverse acoustic (TA) mode (Figures 3.4d,e,h). Very little energy scatters into the other transverse acoustic mode. This conversion apparently occurs because of the asymmetry of the sawtooth geometry and the incident wave-packet's wavelength is on the order of the sawtooth length scale. This coherent interaction of the wave-packet with the interface, which is highly

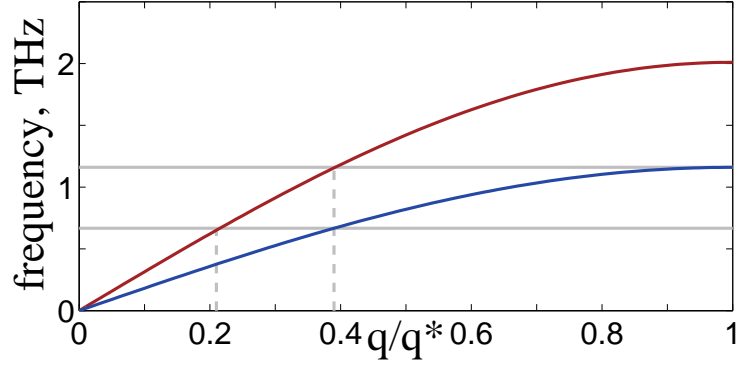


Figure 3.5: Bulk dispersion of two materials in a 1-D chain. Phonons in side A (red line) with wavenumbers above ~ 0.4 cannot cross the interface into side B (blue line) via elastic mechanisms since side B contains no phonon states with a sufficiently high frequency.

sensitive to the specific interface morphology and wave-packet wavenumber, can only be seen by using the wavelet transform.

3.2 STEADY-STATE PHONON POPULATIONS NEAR AN INTERFACE

In the simplest theoretical treatment of phonon transport across an interface, it is generally assumed that the incident population of phonons is well thermalized, in that the phonon population is the product of the density of states and the Bose-Einstein distribution [111, 112]. Whether this is a good assumption, or to what degree the phonons participating in the thermal boundary conductance are non-thermalized are open questions [121, 122]. The assumptions regarding the *local* phonon population near the interface may be tested with the wavelet transform.

Beginning with the simplest example, consider a truly one-dimensional system. Such a system consists of a chain of atoms that are only permitted to move in the x -direction. The phonon density of states in this system is constant with a value:

$$g(k) = 2 \quad (3.4)$$

Under the conditions of a harmonic lattice and classical statistics, each normal mode, indexed by k , will contain $k_B T$ of energy, where k_B is Boltzmann's constant and T is the absolute temperature. Therefore, if the phonon population is not too far from equilibrium, the kinetic energy density, $\rho(x, k)$, having units $\text{eV}/(\text{nm}^{-1}\text{nm})$ under conditions of thermal transport will not depend on the wavenumber:

$$\rho(x, k) = k_B T(x) \quad (3.5)$$

In collaboration with Nam Le, two simulations were carried out where the domain consisted of a one-dimensional chain of atoms with an interface at the center created by giving the atoms of side B three times the mass of the atoms on side A. In one simulation, the inter-

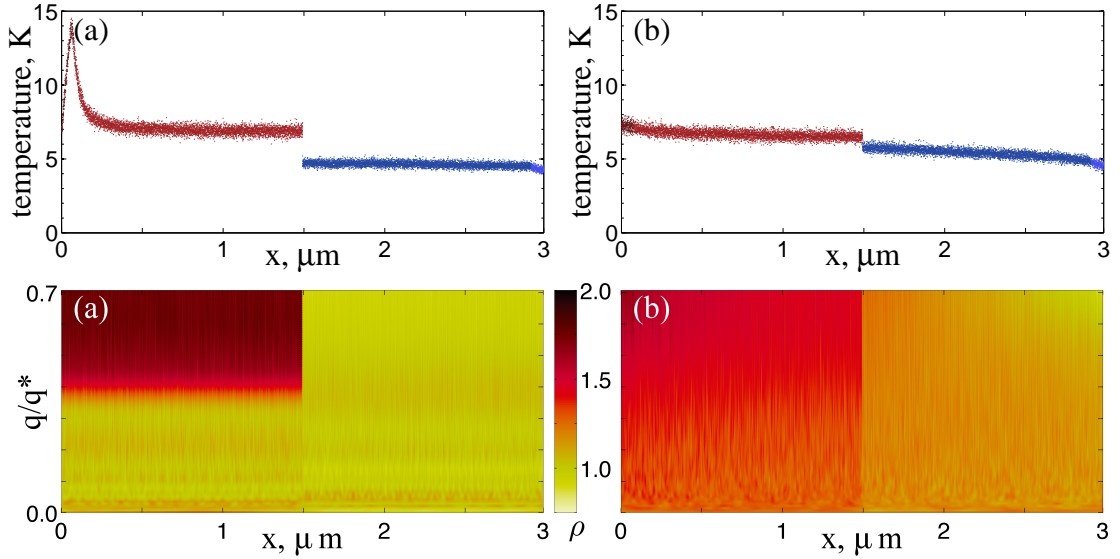


Figure 3.6: Spatial temperature profiles and space-wavenumber phonon energy distributions for non-equilibrium molecular dynamics simulations of harmonic and anharmonic 1-D chains. *TOP*: (a) Temperature profile of harmonic system. (b) Temperature profile of anharmonic system. *BOTTOM*: (a) Space-wavenumber phonon energy distribution of harmonic system. (b) Space-wavenumber phonon energy distribution of anharmonic system.

atomic potential was modeled using the Lennard-Jones potential. In the other simulation, the interatomic potential was the harmonic term of the same Lennard-Jones potential. Figure 3.5 shows the phonon dispersions of sides A and B in both simulations. For elastic interface scattering, phonons with frequencies above 1.15 THz cannot cross the interface, corresponding to phonons with a reduced wavenumber, k/k^* , of approximately 0.4.

The non-equilibrium was created by hot and cold baths on side A and B, respectively, which used velocity rescaling to achieve the desired temperature. The temperature distribution, defined as $T = m(x)\langle v(x,t)^2 \rangle / k_B$, is shown in Figure 3.6 for the harmonic and anharmonic systems. The result of periodically performing the wavelet transform over the course of the simulation and averaging the spectra, $\rho(x,k,t)$, is also shown in Figure 3.6.

For the harmonic system, the most striking feature is the excess of energy above $k/k^* = 0.4$ in side A. Since the system is harmonic and the hot bath uses velocity rescaling, there is no mechanism to redistribute the energy. The assumption of a phonon population close to equilibrium approaching the interface is clearly very wrong in this system. Compare this to the anharmonic system, where the energy distribution is much more flat (constant with respect to wavenumber), in accordance with Equation 3.5. The Lennard-Jones potential is very anharmonic, so there is no discernible non-equilibrium phonon population near the interface because the phonons equilibrate very rapidly through phonon-phonon scattering. The non-equilibrium phonon population that develops in the harmonic system leads to a much lower thermal boundary conductance, which manifests itself as a greater temperature discontinuity at the interface in comparison to the anharmonic system.

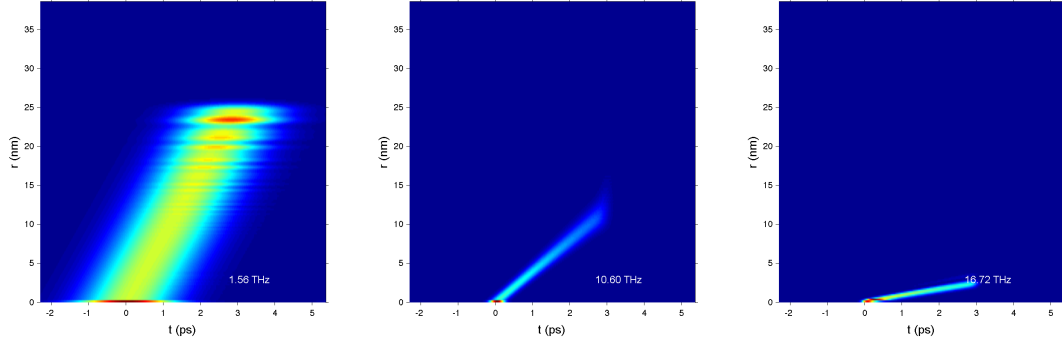


Figure 3.7: Position-time-frequency energy distribution of ballistic transport in $[110]$ direction of silicon obtained by the wavelet transform. Fitting a linear trend at each frequency gives the velocities plotted in Figure 3.8.

3.3 TRANSIENT THERMAL TRANSPORT IN AMORPHOUS MATERIALS

In Sections 3.1 and 3.2, the atomic velocities as a function of position were wavelet transformed for instants in time to create an energy distribution $\mathbb{E} = \mathbb{E}(x, k, t)$. For the non-equilibrium simulations of Section 3.2, the distributions were time-averaged to obtain the final result. A similar post-processing may be conducted, wherein the wavelet transform is performed on the trajectory of a single atom, and then combined with other atoms to create a distribution $\mathbb{E}(x, f, t)$, as in the work of Shiomi and Maruyama [96]. In this section, I discuss this type of analysis and its use in investigating the thermal transport in amorphous materials, or any other isotropic material.

Let us begin with a simple example: the calculation of a phonon's velocity as a function of its frequency. The simulation domain consists of a long thin block of silicon. Beginning from the ground state, the plane of atoms at the origin is perturbed by giving them some small, finite velocity. This event, localized in time and space, corresponds to the introduction of energy into the crystal at all wavelengths and frequencies (in the style of the delta function in Fig. 2.3). As the simulation progresses, the velocities of each atom are collected, converted to a suitable one-dimensional signal (Eq. 3.3), and wavelet transformed. If the domain is long in the z -direction, then the z -component of the atomic velocity would correspond to a longitudinal mode and the x and y components to transverse modes. The simulation can be performed for any crystallographic direction aligned with the z -axis.

Figure 3.7 shows different slices of frequency of the resulting energy distribution. Because a small initial amplitude was used for the perturbation, the system is harmonic and the energy transport is ballistic. This results in the linear relationship between distance and time seen in Figure 3.7. Fitting the linear trends for each frequency produces the frequency-dependent phonon velocity in Figure 3.8. There is good agreement at low frequencies between the present wavelet transform-based method and the actual value as calculated by lattice dynamics. Disagreement above ~ 11 THz in the velocities is due to frequency-blurring of wavelet transform (Eq. 2.5). The way the one-dimensional signal was constructed did not distinguish between

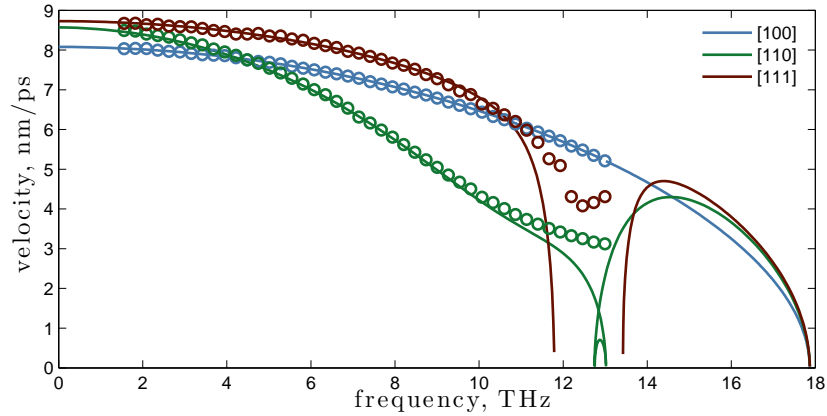


Figure 3.8: Frequency-dependent phonon group velocities in high-symmetry directions of silicon obtained by the wavelet transform. Solid lines give the actual velocities from lattice dynamics.

the acoustic and optical branches, so at high frequencies, the energy distribution is influenced by contributions of each type of phonon.

The same type of simulation may be conducted for an isotropic material, like a glass, using a spherical coordinate system instead of a cartesian coordinate system. The simulation methodology is sketched in Figure 3.9. This time, the localized heating event consists of a single atom, rather than a plane of atoms. The vibrational energy would then travel away from the central atom in all directions. The motion of any single atom over time will then depend on the times at which vibrations of a certain frequency reach it. The wavelet transform is performed on the x , y , and z components of each atom's time-dependent velocity. The velocity signal should be weighted by the square-root of half the atom's mass so that the wavelet energy, $\rho(t, f)$, will give the kinetic energy as a function of time and frequency for that atom. The time-space-frequency energy distribution is constructed by summing $\rho(t, f)$ of each cartesian component of each atom in a shell with constant radius from the perturbed atom. This yields an energy distribution $\rho(t, r, f)$ which must be fit to a transport model to obtain the transport coefficients, like velocity.

Zuckerman and Lukes used a similar method to great effect to study anisotropic wave propagation through a crystal [123] and the scattering of phonons by embedded nanoparticles [124] in molecular dynamics simulations. By exciting a single atom in the crystal at a certain frequency, and measuring the motion of atoms forming a plane some distance away, the authors were able to calculate the velocities of phonons with different wavevectors and polarizations [123] and quantitatively measure their scattering with embedded nanoparticles [124].

Whereas the energy transport in the previous example was purely ballistic by design, the transport in an amorphous material is necessarily diffusive for certain frequencies according to the Allen–Feldman theory [28, 125]. The general partial differential equation for describing such transport is the diffusive wave equation (also known as Cattaneo's Equation or the Telegrapher's Equation):

$$\frac{\partial^2 \theta}{\partial t^2} + \gamma \frac{\partial \theta}{\partial t} = v^2 \nabla^2 \theta \quad (3.6)$$

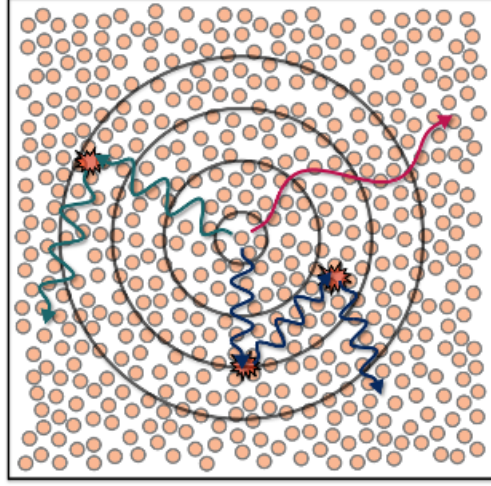


Figure 3.9: Sketch of simulation method for calculating the frequency-dependent diffusivity of an isotropic material. The central atom is perturbed at the start of the simulation, causing vibrational energy of different frequencies to radiate outwards. The atomic trajectories within shells of constant radii are wavelet transformed and summed to obtain the time-position-frequency energy distribution fit to Equation 3.8.

which for radial symmetry in a spherical coordinate system has the form:

$$\frac{\partial^2 \theta}{\partial t^2} + \gamma \frac{\partial \theta}{\partial t} = v^2 \left(\frac{\partial^2 \theta}{\partial r^2} + \frac{2}{r} \frac{\partial \theta}{\partial r} \right) \quad (3.7)$$

where θ is the transported quantity (*not* an angle), γ is the relaxation rate, and v is the velocity. The thermal diffusivity, α , is defined as $\frac{v^2}{\gamma}$ such that as v approaches infinity, the regular heat diffusion equation is recovered. The general solution to Equation 3.7 may be looked up in a reference book [126] as:

$$\theta(t, r) = \frac{2}{Rr} e^{-\frac{1}{2}\gamma t} \sum_{n=1}^{\infty} \sin\left(\frac{n\pi r}{R}\right) \left(\frac{\gamma \sin(t\sqrt{\lambda_n})}{2\sqrt{\lambda_n}} + \cos(t\sqrt{\lambda_n}) \right) \int_0^R \epsilon f_0(\epsilon) \sin\left(\frac{n\pi \epsilon}{R}\right) d\epsilon ;$$

$$\lambda_n = \left(\frac{n\pi v}{R} \right)^2 - \frac{\gamma^2}{4} \quad (3.8)$$

The integral can be evaluated analytically if the initial condition, $f_0(\epsilon)$, is modeled as a Gaussian with width σ as:

$$\int_0^R \epsilon f_0(\epsilon) \sin\left(\frac{n\pi \epsilon}{R}\right) d\epsilon = C_1 n e^{-C_2 n^2} \left[\operatorname{erfi}\left(C_2 \frac{1}{2} n - C_3\right) - \operatorname{erfi}\left(C_2 \frac{1}{2} n + C_3\right) \right] ;$$

$$C_1 = \frac{\pi i \sigma^2}{4R} ; C_2 = \frac{1}{2} \left(\frac{\pi \sigma}{R} \right)^2 ; C_3 = \frac{iR}{2\frac{1}{2}\sigma} \quad (3.9)$$

The use of a Gaussian as the initial condition is justified if its width is less than the interatomic spacing. The Gaussian permits faster convergence of the infinite series in Equation 3.8 than, say, a delta function. The series typically converges for n on the order of 100 if $v^2 \sim \gamma$ or 1000 if $v^2 \gg \gamma$. Because the wavelet energy distribution was built by summing the contributions of atoms in each radial bin, the distribution $\theta(t, r)$ must be weighted by r^2 in order to

correspond to the molecular dynamics simulation. This analytical distribution is then fit to constant frequency slices of the wavelet energy distribution to obtain $v(f)$ and $\gamma(f)$.

This method of calculating the frequency-dependent transport properties is conceptually similar to work by Sheng and Zhou [127] and Beltukov *et al.* [128]. These authors studied toy models of a disordered system by exciting a central “atom” or “atoms” at a certain frequency and then observing the resulting transport of energy. Their results are surprisingly transferable as many of the features common to amorphous materials were observed, including a plateau in the thermal conductivity at a few tens of kelvins. With their approach, a different simulation must be conducted for each frequency explored. In the present simulation method, only one simulation is needed as the frequencies are discerned in post-processing with the wavelet transform.

3.4 CONTRIBUTIONS

In this chapter I outlined three new simulation methods that harness the wavelet transform to investigate nanoscale thermal transport. Wavelet transform analysis of wave-packet simulations (Section 3.1) give insight into the anharmonic scattering mechanisms of phonons and the complex interaction of phonons with interfaces of varying geometries.

Wavelet transform analysis of steady-state non-equilibrium thermal transport across an interface (Section 3.2) offers the chance to observe non-equilibrium phonon populations in the vicinity of the interface. Such information may be compared against the assumptions behind current and future theories of thermal boundary conductance, *i.e.* under what conditions does the phonon population obey the Bose-Einstein or Maxwell-Boltzmann distributions? Extending the method to the three-dimensional non-equilibrium simulations used to measure the thermal boundary conductance is a matter of correctly applying Equation 3.3 to obtain a one-dimensional signal (aligned with the long axis of the simulation) representing the population of phonons with the same polarization and wavevector direction in the Brillouin Zone.

Lastly, the proposed method for calculating the frequency-dependent vibrational diffusivity (Section 3.3) offers an independent check of the predictions of the Allen–Feldman theory and Cahill-Pohl model. The method will be applied to simulated a-Si and a-SiO₂ in Chapter 6 and additional strengths will be discussed.

4

POTENTIALS FOR THE SIMULATION OF AMORPHOUS SILICON AND SILICA

A disordered atomic structure characterizes the amorphous phase. Lack of order causes strong scattering of lattice vibrations, leading to a low thermal conductivity on the order of 1 W/mK or less for all temperatures (Fig. 1.1). While a crystal has a precisely defined structure, an amorphous material does not. Thus, how an amorphous material is prepared may alter its thermal properties; two preparation methods may yield two structures that are qualitatively similar, *i.e.* amorphous, but quantitatively different. For example, the thermal conductivity of a-SiO₂ thin films may be altered by nearly a factor of two depending on the deposition method [129]. The ability to predict the thermal properties of amorphous materials will help guide the selection of materials for technological applications.

Due to the resistance of the amorphous phase to theoretical analysis, molecular dynamics remains one of the foremost tools for understanding amorphous materials [130]. Although much of the fundamental physics of glass formation and properties may be investigated through the use of simple potentials, *e.g.* the Lennard-Jones potential [21, 131], if molecular dynamics is to be used to gain quantitative insight into a material system, the interatomic potentials used must be carefully vetted against experimental, or at least *ab initio*, data. Furthermore, all the richness of phenomena exhibited by glasses, *e.g.* whether or not the thermal conductivity plateaus at a few tens of Kelvin, may not be captured by a single potential.

The material systems of amorphous silicon (a-Si) and amorphous silica (a-SiO₂) were selected as examples of atypical and typical glasses, respectively. To lay the foundation for future work, especially that of Chapter 6, I tested six potentials of silicon and three potentials of silica for their abilities to reproduce the experimental thermophysical properties of their amorphous phases. The amorphous structures were generated by quenching the liquid phase and I tested the quench rate over three orders of magnitude from 0.1 K/ps to 100 K/ps to determine if there was a quench rate leading to properties that matched the experimental ones the closest and to observe any systematic effects the quench rate had on the properties.

The rest of the chapter is organized as follows. In Section 4.1, I give the functional forms of the tested Si and SiO₂ potentials and the properties to which they were fit. In Section 4.2, I outline the simulation procedure and provide details regarding the calculation of the radial distribution function, coordination histogram, angular distribution function, thermal conductivity, density of states, and elastic constants. In Section 4.3, I present the data obtained by the above calculations for each potential and quench rate. Finally, in Section 4.4, I discuss the

fitness of each potential to reproduce some or all of the experimental observations and the impact that the quench rate had on the calculated structural, acoustic, and thermal properties.

4.1 POTENTIALS

For the silicon potentials, I tested three parameter sets for the three-body Stillinger-Weber potential [132] and two multi-body potentials: the Tersoff potential [133] and the Environment Dependent Interatomic Potential (EDIP) [134]. In evaluating the ability of the potentials to reproduce experimental values, it is instructive to consider the criteria by which the potential was fit.

The original parameters of the Stillinger-Weber potential (SW) were developed by fitting to the diamond structure lattice constant and binding energy, the melting temperature, and the liquid structure of real silicon [132]. Vink *et al.* optimized their Stillinger-Weber parameters (VBWM) for the amorphous phase, fitting the transverse acoustic and optical peaks in the vibrational density of states, the radial distribution function, and the angular distribution function [135]. Albenze *et al.* fit their potential (SW₁₁₅) to the structural properties of the liquid and amorphous phases, and the thermodynamic properties of the crystal and glass phase transitions [136]. I used the most recent of Tersoff's parameters (Tersoff) for silicon as they improve upon the elastic and liquid properties calculated using previous sets [133]. This particular parameterization was fit to the binding energies and lattice constants of the diamond and hypothetical crystalline structures of silicon, as well as the elastic constants of silicon [133]. The EDIP potential is similar to the Stillinger-Weber form, but the two- and three-body terms of the EDIP have a functional dependence on the local coordination [134], that is, the number of neighbors an atom has. The EDIP potential was fit to an *ab initio* database of crystal binding energies and lattice constants, self diffusion, energies of unrelaxed point defects, stacking fault energies, and experimental elastic constants [134].

The tested silica potentials comprise a Tersoff form by Munetoh *et al.* (M₃S) [137], and two variations of a Buckingham potential: those by van Beest *et al.* (BKS) [138] and Tsuneyuki *et al.* (TTAM) [139]. The M₃S potential was fit to *ab initio* calculations of the structures and binding energies of several molecules of silicon and oxygen, as well as to the experimental lattice constants of α -quartz [137]. The parameters of the BKS potential were found iteratively by fitting *ab initio* data of small silicon-oxygen clusters and then to the experimental elastic constants and lattice constants of α -quartz [138]. The TTAM potential was fit to *ab initio* calculations of the potential energy surface of a SiO₄ tetrahedra and checked against α -quartz [139]. For all three potentials, the authors checked the predictions of the resulting interatomic potential against the experimental properties of several other silica polymorphs and found reasonable agreement [137–139]. In the BKS and TTAM potentials used here, an 18–6 Lennard-Jones term has been added to prevent unphysical behavior in the liquid phase [140]. While other potentials for SiO₂ have been developed, e.g. those by Tangney and Scandolo [141] and Watanabe

Table 4.1: Energy parameters used in Stillinger-Weber potentials of a-Si. All other parameters are the same as those from the original parameterization [132].

Potential	$\epsilon \cdot A$, eV	$\epsilon \cdot \lambda$, eV
SW	15.2781	45.5210
VBWM	11.620	51.9224
SW115	10.6994	36.6535

et al. [142], these potentials are not currently available in LAMMPS [143], which is perhaps the most widely used molecular dynamics simulation package and also the one used here.

4.1.1 Silicon Potentials

The Stillinger-Weber potential is the sum of a two-body potential and a three-body potential [132]:

$$V = \epsilon \left[A \frac{1}{2} \sum_{ij} v_{ij}^{(2)}(r_{ij}) + \lambda \frac{1}{2} \sum_{ijk} v_{ijk}^{(3)}(\mathbf{r}_{ij}, \mathbf{r}_{ik}) \right] \quad (4.1a)$$

$$v_{ij}^{(2)}(r_{ij}) = \left[B \left(\frac{r_{ij}}{\sigma} \right)^{-p} - 1 \right] \exp \left(\left[\frac{r_{ij}}{\sigma} - 1 \right]^{-1} \right) \quad (4.1b)$$

$$v_{ijk}^{(3)}(\mathbf{r}_{ij}, \mathbf{r}_{ik}) = \exp \left[\frac{\gamma}{\frac{r_{ij}}{\sigma} - a} + \frac{\gamma}{\frac{r_{ik}}{\sigma} - a} \right] \cdot \left(\cos \theta_{ijk} + \frac{1}{3} \right)^2 \quad (4.1c)$$

The summations in Equation 4.1a are made over all atoms i, j, k with $i \neq j \neq k \neq i$. In the three-body interactions of Equation 4.1, and the ones to follow, the angle formed by a group of atoms ijk is measured with atom i as the vertex. The factors of one-half offset the double counting of interactions. Equation 4.1a is often practically computed for unique pairs and trios of atoms, such that $i < j < k$, in which case the factors of one-half are no longer needed [132]. The three parameter sets tested for a-Si were all identical except for the energy scales $\epsilon \cdot A$ and $\epsilon \cdot \lambda$, which are shown in Table 4.1. The rest of the parameters may be found in Stillinger and Weber [132]. The VBWM strengthens the three-body interaction and weakens the two-body interaction. The SW115 weakens both interactions, but the ratio of the three-body energy to two-body energy is increased by about 15% relative to the SW.

The Tersoff potential has the form [133]:

$$V = \frac{1}{2} \sum_{ij} f_C(r_{ij}) [A \exp(-\lambda_1 r) - b_{ij} \exp(-\lambda_2 r)] \quad (4.2a)$$

$$f_C(r_{ij}) = \begin{cases} 1; & r < R - D \\ \frac{1}{2} - \frac{1}{2} \sin \left[\frac{\pi}{2} \frac{r-R}{D} \right]; & R - D < r < R + D \\ 0; & r > R + D \end{cases} \quad (4.2b)$$

$$b_{ij} = B(1 + \beta^n \zeta_{ij}^n)^{-\frac{1}{2n}} \quad (4.2c)$$

$$\zeta_{ij} = \sum_{k \neq (i,j)} f_C(r_{ik}) g(\theta_{ijk}) \exp[\lambda_3^3 (r_{ij} - r_{ik})^3] \quad (4.2d)$$

Table 4.2: Parameters of Tersoff potential for a-Si [133] and a-SiO₂ (M3S) [137]. (*) These values differ in the fifth significant figure between Tersoff [133] and Munetoh *et al.* [137]. (†) The authors use significantly different values. Left: Tersoff, right: Munetoh *et al.*

Parameter	Si	O	Mixed
A , eV	$1.8308 \cdot 10^3$	$1.88255 \cdot 10^3$	$\sqrt{A_{Si}A_O}\delta_{jk}$
B , eV	$4.7118 \cdot 10^2$	$2.18787 \cdot 10^2$	$1.17945\sqrt{B_{Si}B_O}\delta_{jk}$
λ_1 , Å ⁻¹	2.4799	4.17108	$0.5(\lambda_{1,Si} + \lambda_{1,O})\delta_{jk}$
λ_2 , Å ⁻¹	1.7322	2.35692	$0.5(\lambda_{2,Si} + \lambda_{2,O})\delta_{jk}$
β	$1.0999 \cdot 10^{-6*}$	$1.1632 \cdot 10^{-7}$	β_i
n	$7.8734 \cdot 10^{-1}$	1.04968	n_i
c	$1.0039 \cdot 10^5$	$6.46921 \cdot 10^4$	c_i
d	$1.6218 \cdot 10^{1*}$	4.11127	d_i
h	$-5.9826 \cdot 10^{-1*}$	$-8.45922 \cdot 10^{-1}$	h_i
λ_3 , Å ⁻¹	$1.7322^\dagger 0.0$	0.0	0.0
R , Å	$2.85^\dagger 2.65$	1.85	$\sqrt{R_i R_k}$
D , Å	0.15	0.15	$0.155 - 0.005\delta_{jk}$

$$g(\theta_{ijk}) = 1 + \frac{c^2}{d^2} - \frac{c^2}{d^2 + (h - \cos\theta_{ijk})^2} \quad (4.2e)$$

As with the Stillinger-Weber potential, the factor of one-half in Equation 4.2a offsets the double counting of pair interactions and may be neglected if the summation is taken for $i < j$. Unlike the Stillinger-Weber potential, which explicitly includes three-body interactions, the Tersoff potential implicitly includes them in the coefficient of the attractive pair interaction (the second exponential in Eq. 4.2a). The parameters used for a-Si are given in Table 4.2 (along with the parameters for a-SiO₂).

The EDIP potential is more complex than both the SW and Tersoff potentials. Its form is similar to the SW, with the key difference being that certain constants in the SW become functions of the local coordination of atom i , that is, the number of neighbors of i within some cutoff distance. By accounting for the local coordination, the EDIP seeks to model a wider range of defects and disorder than the more “rigid” forms of the SW and Tersoff potentials. The details may be found in Justo *et al.* [134].

4.1.2 Silica Potentials

The M3S potential [137] uses the Tersoff potential (Eq. 4.2) with coefficients for the O–O and Si–O interactions given in Table 4.2. Mixed interactions occur when atoms i , j , and k are not all the same element. In this case, the parameters depend on the identities of all three atoms, which is accounted for by Kronecker deltas: δ_{jk} is one when atoms j and k are the same element and zero otherwise. In this case, atom i is at the vertex of the angle formed by ijk . The primary advantage of the M3S potential over other potentials for SiO₂ is that it does not require calculation of the Coulomb force, which represents the majority of the computational cost.

The BKS [138] and TTAM [139] potentials both have a form based on the Buckingham potential:

$$V = \frac{1}{2} \sum_{ij} \frac{q_i q_j}{r_{ij}} + A_{ij} \exp(-b_{ij} r_{ij}) - \frac{c_{ij}}{r_{ij}^6} \quad (4.3)$$

Table 4.3: Parameters used in Buckingham-style potentials of a-SiO₂: BKS [138] and TTAM [139] potentials. There is no pair interaction among Si atoms in the BKS potential.

Potential	Pair	A, eV	b, Å ⁻¹	c, eV·Å ⁶	ε, eV	σ, Å
BKS	Si-Si	-	-	-	-	-
	Si-O	18003.7572	4.87318	133.5381	0.017966	1.3
	O-O	1388.7730	2.76000	175.0000	0.0004781	2.2
TTAM	Si-Si	872360000	15.2207	23.3000	13.233	0.4
	Si-O	10722	4.79593	70.735	0.011229	1.3
	O-O	1756.9	2.84641	214.74	0.0004781	2.2

where q is the charge of each atom, taken as $q_{\text{Si}} = +2.4e$ and $q_{\text{O}} = -1.2e$.

The original BKS and TTAM potentials are not suitable for simulation of the liquid phase. The r^{-6} dispersive term in Equation 4.3 dominates the others for a small separation distance, leading to atoms erroneously fusing together. The energy barrier preventing this from occurring has a height corresponding to about 5000 K [140]. For the system to remain physically realistic above this temperature, Equation 4.3 must be modified. Following Guissani *et al.* [140], I added an 18-6 Lennard-Jones term to the potential such that:

$$V' = V + \frac{1}{2} \sum_{ij} 4\epsilon_{ij} \left[\left(\frac{\sigma_{ij}}{r_{ij}} \right)^{18} - \left(\frac{\sigma_{ij}}{r_{ij}} \right)^6 \right] \quad (4.4)$$

At temperatures above the melting point, the addition prevents atoms from overcoming the original barrier and binding together. The coefficients used in the BKS and TTAM potentials are given in Table 4.3. I used a modification of the Wolf method [144] by Fennell *et al.* [145] to compute the Coulomb interactions. This approach is about an order of magnitude faster than the traditional Ewald sum [144] and gives the same results for appropriately chosen parameters [146]. Kieffer *et al.* give a helpful overview of the Ewald sum and practical aspects of its application [147]. For the Wolf method, a damping parameter of 0.223 \AA^{-1} and a cutoff of 10 \AA were used [148, 149].

4.2 METHODS

4.2.1 Obtaining the Amorphous Structure

Whereas there are a few methods for creating an amorphous structure, for example algorithmically disordering a crystal [150] or even modifying atomic coordinates “by hand” [151], the most straightforward approach, and one that approximates an actual procedure for glass formation, is to quench the liquid phase to create the amorphous phase. I tested the effect of the quench rate on the structure and properties of the resulting amorphous material, quenching rates logarithmically spaced between 0.1 and 100 K/ps.

All simulations were run with LAMMPS [143], a timestep of 0.5 fs, and, unless otherwise stated, in the NPT ensemble (constant number, pressure, temperature). The system was first equilibrated at 300 K for 25 ps. Then, it was heated at a rate of 100 K/ps to a temperature above the melting point, which was material dependent (Table 4.4). The melting temperature for each

Table 4.4: Temperatures of liquid phase before quenching for each a-Si and a-SiO₂ potential. Temperatures are in kelvins.

Potential	SW	VBWM	SW ₁₁₅	Tersoff	EDIP	M3S	BKS	TTAM
T_{liquid}	2700	3400	2500	3450	2350	5300	5200	4600

potential was determined using the same heating procedure. The melting temperature was identified by a dip in temperature, caused by the strongly endothermic phase change. The melting temperature so found was not used for the sake of evaluating the fitness of each potential; rather, it was used pragmatically to find the lowest temperature, T_{liquid} , from which to begin the quench process. The melted system was held at T_{liquid} for 200 ps. The system was then quenched at a variable rate, Q , down to 100 K. Quench rates of 0.1, 1, 10, and 100 K/ps were tested for each potential, except for the BKS and TTAM potentials, where simulation time precluded the 0.1 K/ps quench rate. Finally, a fictitious viscosity of 10 meV·ps/Å² was imposed on the motion of the atoms for 30 ps in a NPH ensemble (constant number, pressure, enthalpy) to drain the remaining kinetic energy and bring the system to nearly 0 K.

4.2.2 Thermal Conductivity

The thermal conductivity was calculated using the Green-Kubo method during equilibrium [152, 153]. The quenched structure was equilibrated at 300 K for 100 ps, then the simulation was run for 2 ns, printing the conduction portion of the heat current [154] every 10 time steps. The *first avalanche* criterion [155] was used to determine the cutoff time of the heat current autocorrelation function. For both a-Si and a-SiO₂, an averaging window of 20 ps and a noise-to-signal ratio of 1000 were used.

4.2.3 Density of States

The density of states was calculated differently for a-Si and a-SiO₂.¹ The density of states of a-Si was calculated for the 0 K system using GULP [156]. The density of states of a-SiO₂ was calculated at 1 K using molecular dynamics simulation. The system was allowed to equilibrate for 100 ps at 1 K. Then, velocities were collected every 25 time steps for 25·2¹⁵ time steps (~410 ps). The density of states may be calculated from the atomic trajectory as the Fourier transform of the mass-weighted velocity autocorrelation function [29], as in Equation 2.34 of Section 2.2. The resulting density of states is somewhat noisy because the frequency resolution is so great: $1/N\Delta t$ or 2.44 GHz. So the density of states was smoothed by a Gaussian filter with a standard deviation of 0.1 THz.

¹ Ideally, the density of states of both materials should be calculated using GULP. However, complications arose when implementing the a-SiO₂ potentials in GULP, leading to the decision to use molecular dynamics simulation for the calculation.

4.2.4 Structural Characterization

The radial distribution function, RDF, gives the expected number of atoms within a shell of thickness dr and of radius r , centered about an atom. Whereas the lattice and basis is the structural “fingerprint” of a crystal, the RDF fulfills the same role for an amorphous material. The angular distribution function, ADF, gives the probability density of finding two atoms that form an angle, θ , with a mutual nearest neighbor at the vertex. In glasses with multiple elements, multiple RDFs and ADFs may be defined for each element pair or trio. The radial distribution functions and angular distribution functions were calculated directly from the quenched structures. The bin width for the RDF was 0.025 \AA . The bin width for calculating the ADFs was 0.5 degrees.

4.2.5 Elastic Constants

The elastic constants of a-Si were calculated with GULP [156]. The elastic constants of a-SiO₂ were calculated using finite differences of the ground-state system. The strain used for the finite differences was 10^{-8} . After the system was strained, the potential energy of the system was re-minimized using the conjugate gradient method, requiring fewer than 3000 iterations before the two-norm of the force vector was less than 10^{-10} . The stress tensor was recalculated, from which the elastic constants were determined.² This approach with an amorphous material is more challenging than for a crystal because any significant atomic rearrangements that occur because of the strain will greatly affect the results. Thus a very small strain, and consequently a very tight tolerance for the re-minimization of the system’s energy, must be used. A strain of 10^{-8} and force minimization threshold of 10^{-10} gave well-converged elastic constants.

4.3 RESULTS

4.3.1 a-Si Results

Figure 4.1 shows the RDFs of simulated a-Si for the SW, VBWM, SW₁₁₅, Tersoff, and EDIP potentials for quench rates ranging from 0.1 K/ps to 100 K/ps . In each figure of this section, the color of a line corresponds to the potential used and the lightness, or shade, of the line corresponds to the quench rate. The lightest shade always corresponds to a quench rate of 100 K/ps and the darkest shade to 0.1 K/ps (or 1 K/ps for the BKS and TTAM potentials). Each curve plotted in this section is the average of five independent simulations. When available, the data is compared to experiment, denoted by a black line or markers.

Across all potentials, a faster quench rate erodes the peak at $\sim 3.75 \text{ \AA}$ and reduces the valley depth at $\sim 6.25 \text{ \AA}$ in the RDF (the curves have been offset for clarity). The SW, Tersoff,

² See the example calculation by Dr. Aidan Thompson included in recent versions of the LAMMPS package.

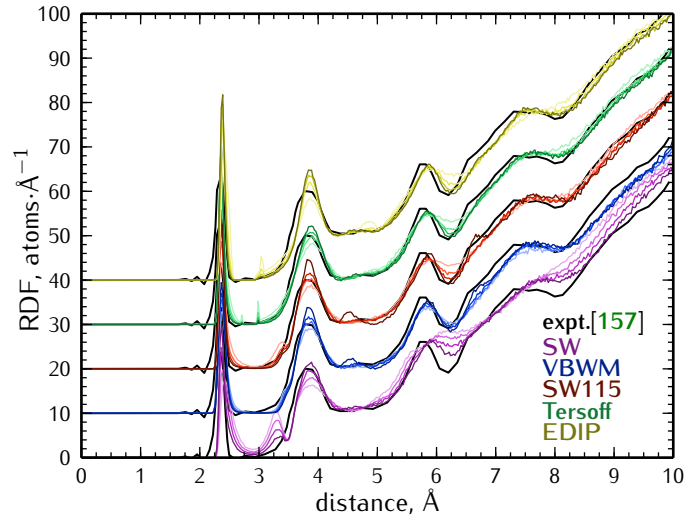


Figure 4.1: Radial distribution function of simulated a-Si generated using different potentials and quench rates. The radial distribution functions of different potentials have been offset for clarity.

and EDIP potentials give extraneous peaks between the experimental first and second neighbor peaks [157]. The SW115 potential and the VBWM potential have comparable levels of fidelity to the experimental system, although the VBWM underestimates the medium-range coordination approaching 10 Å.

Figure 4.2 shows the angular distribution functions of the simulated a-Si structures. The SW potential has a shoulder in the angular distribution function at $\sim 80^\circ$. The EDIP and, to a lesser extent, Tersoff, potentials have a peak at 60° , which is consistent with the erroneous features of their radial distribution functions. All potentials have a primary peak at roughly the tetrahedral angle of $\sim 109.5^\circ$. Faster quench rates tend to broaden the angular distribution function about the tetrahedral angle and strengthen the shoulders in the SW, Tersoff, and EDIP potentials.

In addition to the angular distribution function, the number of nearest neighbors, called the coordination, is an important metric of the short-range order of glassy materials. The number of nearest neighbors is counted for each atom and put into a histogram, plotted in Figure 4.3. Slower quench rates lead to an increase in 4-coordinated atoms compared to 3-, 5-, and 6-coordinated atoms. Defects in a-Si arise from 3-coordinated and 5-coordinated atoms, also referred to as *dangling* and *floating bonds*, respectively [158]. The experimental defect concentration is no more than a couple of percent, which may be due to either dangling bonds alone or dangling and floating bonds [158–160]. The experimental average coordination of 3.88 suggests that 3-coordinated atoms cluster about vacancies in the network structure [161], such that 3-coordinated atoms exist at a concentration of 3–4%. The VBWM gives 3- and 5-coordinated atoms on the order of the experimental values while the other potentials underestimate the 3-coordinated or vastly overestimate the 5-coordinated experimental values. The VBWM shows little sensitivity to the quench rate. The other potentials show a stronger sensitivity to the quench rate.

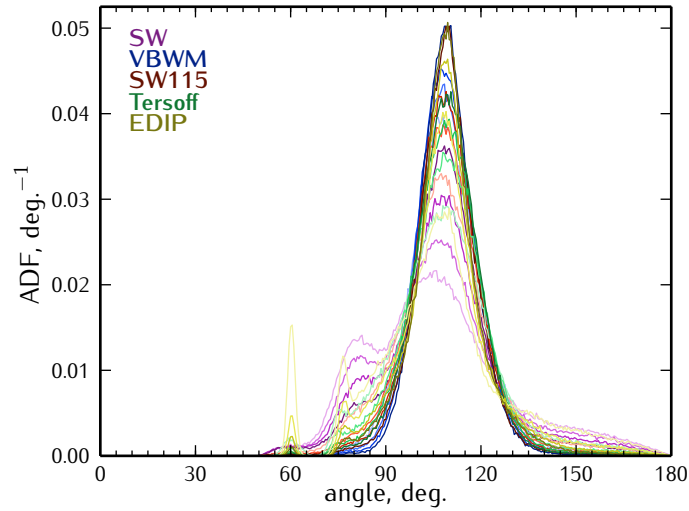


Figure 4.2: Angular distribution function of simulated a-Si generated using different potentials and quench rates.

Figure 4.4 shows the density of states of the simulated a-Si. Every potential underestimates the vibrational density of states for the acoustic peak at ~ 5 THz. Only the VBWM and Tersoff potentials properly fit the low frequency, f^2 , regime which is related by the Debye theory to the sound speed of a-Si. The VBWM potential correctly reproduces the optical peak, which is not surprising considering that this was one of its fitting metrics. Faster quench rates tend to broaden the vibrational density of states. Just as in Figure 4.3, the VBWM potential is least sensitive to the quench rate.

Representative scalars were calculated for Figures 4.1-4.3 to compare against experiment and are presented in Table 4.5. The longitudinal and Young's mode sound speeds, and the thermal conductivities are also presented. Trends in the first neighbor peak and tetrahedral bond-angle distribution that cannot easily be discerned from Figures 4.1 and 4.2 are clarified. The quench rate monotonically affects each property for a given potential, but the sign of the trend might differ. For example, a slower quench rate leads to higher density VBWM a-Si, but reduces the density of the a-Si modeled with every other potential. The Young's mode velocity is a composite of the longitudinal and transverse acoustic velocities:

$$v_Y = \left[\left(\frac{1}{3} \frac{1}{v_L} \right)^{-3} + \left(\frac{2}{3} \frac{1}{v_T} \right)^{-3} \right]^{-\frac{1}{3}} \quad (4.5)$$

where v_L is the longitudinal acoustic velocity and v_T is the transverse acoustic velocity.

4.3.2 a-SiO₂ Results

Figure 4.5 shows the radial distribution functions of simulated a-SiO₂ generated by the M₃S, BKS, and TTAM potentials for quench rates ranging from 0.1 K/ps to 100 K/ps for the M₃S potential and 1 K/ps to 100 K/ps for the BKS and TTAM potentials. As with the a-Si data,

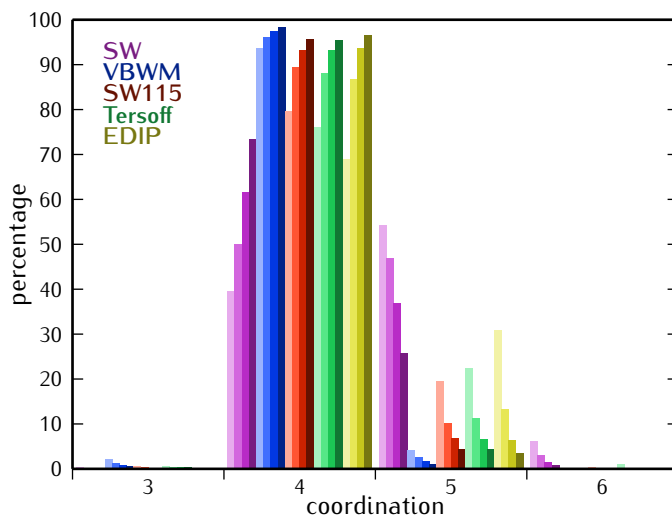


Figure 4.3: Coordination histogram of simulated a-Si generated using different potentials and quench rates.

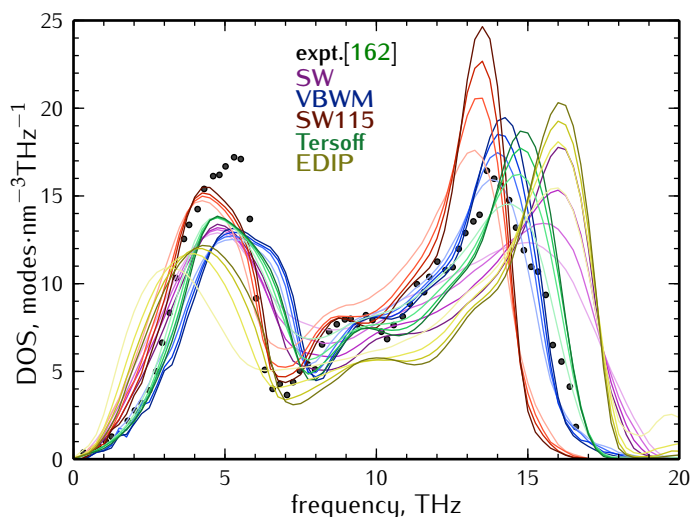


Figure 4.4: Density of states of simulated a-Si generated using different potentials and quench rates.

in each figure of this section, the color of a line corresponds to the potential used and the lightness, or shade, of the line corresponds to the quench rate. The lightest shade always corresponds to a quench rate of 100 K/ps and the darkest shade to 0.1 K/ps, for the M3S potential, or 1 K/ps for the BKS and TTAM potentials. Each curve plotted in this section is the average of five independent simulations. When available, the data is compared to experiment, denoted by a black line.

All three silica potentials greatly underestimate the width of the first, second, and third neighbor peaks in the experimental radial distribution function (Fig. 4.5). Beyond this distance, the BKS and TTAM potentials tend to reproduce the shape of the experimental radial distribution function, albeit shifted to slightly farther distances.

Figure 4.6 shows the angular distribution functions for O-Si-O and Si-O-Si bond-angles of the simulated a-SiO₂. As with a-Si, the M3S (Tersoff) potential gives an erroneous peak at

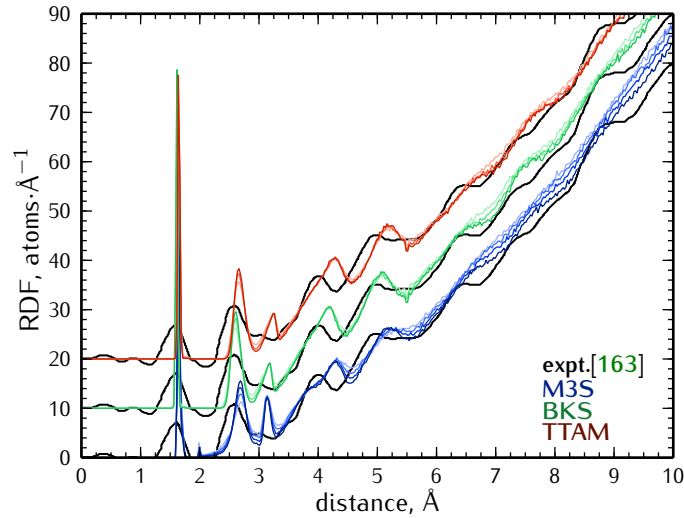


Figure 4.5: Radial distribution function of simulated a-SiO₂ generated using different potentials and quench rates.

$\sim 60^\circ$ for the O–Si–O bond-angle distribution. The BKS and TTAM have good agreement with the experimental Si–O–Si bond-angle distribution [164], while the Tersoff potential greatly underestimates the width and includes an erroneous peak at 120° .

Surprisingly, experimental calculation of the vibrational density of states for a-SiO₂ is difficult to find in the literature. Plotted in Figure 4.7 is the effective density of states, as presented by Price and Carpenter [165, 166]. The authors note that the effective density of states differs from the true one, especially below 3.6 THz, but to what extent and at which frequencies is uncertain. The BKS and TTAM potentials have a similar shape below 20 THz: that of a plateau. The M₃S potential has an excess in density of states above the other two potentials, like the experimental effective density of states, although the frequency of the peak is different. The M₃S potential fails to reproduce the split optical peaks at 30–40 THz. The BKS potential fits the optical peaks reasonably well.

As with the simulated a-Si, representative scalars were calculated for Figures 4.5 and 4.6 to compare against experiment and are presented in Table 4.6 along with longitudinal and transverse sound speeds and thermal conductivity. Trends in the first neighbor peak and Si–O–Si bond-angle distribution that cannot easily be discerned from Figures 4.5 and 4.6 are clarified. As with a-Si, the quench rate monotonically affects each property of a-SiO₂ for a given potential.

4.4 DISCUSSION

With regard to the thermophysical properties at approximately room temperature and below, I recommend the VBWM potential for simulating amorphous silicon. The VBWM potential does not display the erroneous spikes between the first and second neighbor peaks as do the Tersoff and EDIP potentials, nor does it display a shoulder in the second neighbor peak like the

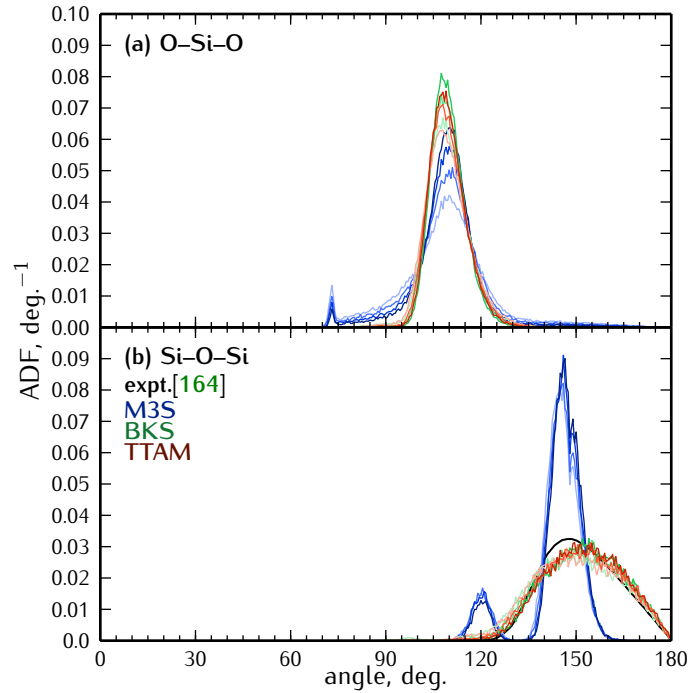


Figure 4.6: Angular distribution functions of simulated a-SiO₂ generated using different potentials and quench rates.

SW potential (Fig. 4.1). For the same reasons, the angular distribution function of the VBWM potential remains as a Gaussian centered at the tetrahedral angle, with no other peaks (Fig. 4.2). The VBWM is the only potential to have a non-trivial number of 3-coordinated atoms, which is most consistent with experiment [161] (Fig. 4.3). The VBWM is the only potential that fits the optical peak; however, its agreement with the magnitude of the transverse acoustic peak and the longitudinal acoustic peak is worse than the SW₁₁₅ potential (Fig. 4.4). Even so, the speeds of sound predicted by the VBWM potential are closer to the experimental values than those of the SW₁₁₅ potential (Table 4.5). The good agreement of the VBWM potential is not entirely surprising since many of the metrics were used in the fitting procedure for it. Since the VBWM potential fits the experimental data about as well as the other candidates for most properties, and is superior to all others in certain properties, the VBWM potential will be used for all future simulations of a-Si.

The M₃S, BKS, and TTAM potentials for silica each had shortcomings regarding their ability to reproduce the tested thermophysical properties at room temperature and below, as partially demonstrated in the results summarized in Table 4.6. The M₃S potential's failings were similar in many respects to the Si Tersoff potential: for example, the erroneous spike between the first and second neighbor peaks in the radial distribution function (Fig. 4.5) and in the O-Si-O angular distribution function (Fig. 4.6). One final shortcoming of the M₃S potential is that it has a single optical peak instead of a split optical peak as displayed by BKS and TTAM potentials, as well as experiment [165] (Fig. 4.7). Between the BKS and TTAM potentials, they each show similar agreement with the experimental radial distribution function (Fig. 4.5) and Si-O-Si angular distribution function (Fig. 4.6b). The BKS potential correctly fits the frequen-

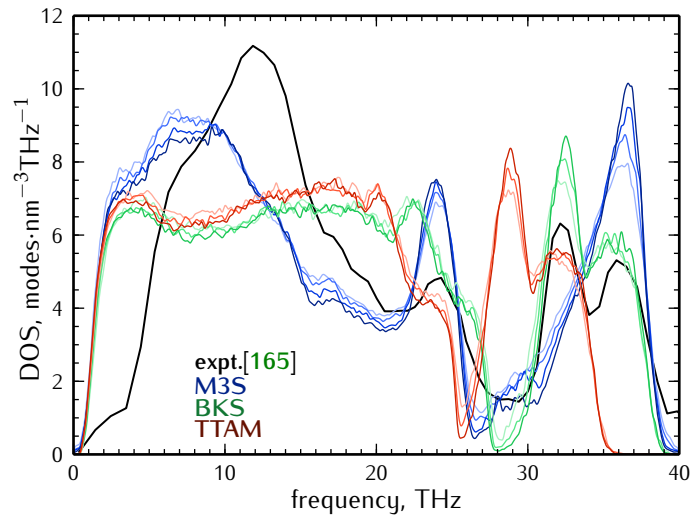


Figure 4.7: Density of states of simulated a-SiO₂ generated using different potentials and quench rates.

cies of the optical peaks in the density of states, whereas the TTAM potential underestimates the frequency (Fig. 4.7). Both the BKS and TTAM potentials have a substantial disagreement with the experimental speeds of sound (Table 4.6), although the TTAM's is less so. The BKS potential does a better job of fitting the optical peaks, while the TTAM potential is closer to the speeds of sounds. There are several more complex potentials for SiO₂, many of which include a term for the dipole interaction, *e.g.* the potential of Tangney and Scandolo [141]. These potentials may more accurately model a-SiO₂, but at greater computational cost, which is already a considerable expense for any potential that models charge interactions.

The effect of the quench rate was minor compared to the effect of the potential with regard to the tested thermophysical properties of the amorphous phase at room temperature and below. For simulations of amorphous silicon and amorphous silica in these regime where the properties tested here are of interest, researchers should balance the computational requirements of longer quenching times against the need for more “ideal” amorphous structures when using the above recommended potentials. At some quench rate much slower than those studied here, the system must necessarily cease to converge to the “ideal” amorphous structure and begin to form polycrystalline structures. For researchers interested in the glass transition and properties near the transition temperature, a potential besides the VBWM or BKS may be more suitable and the specific quench rate may be more critical to fulfilling the objectives of the simulation.

4.5 TABULATED DATA

Table 4.5: Thermophysical properties of simulated a-Si compared to experiment for SW [132], VBWM [135], SW115 [136], Tersoff [133], and EDIP [134] potentials and quench rates ranging from 0.1 to 100 K/ps. The number density ρ , RDF first peak position r_p and width σ_r , ADF peak position θ_p and width σ_θ , mean coordination C , Young's mode sound speed v_γ and longitudinal sound speed v_L , and thermal conductivity k are tabulated. The experimental data is pieced together from the works of Custer *et al.* [167], Laaziri *et al.* [157, 161], Cox-Smith *et al.* [168], and Zink *et al.* [14]. The a-Si samples studied in these experiments were generated using ion-implantation (Custer *et al.* [167] and Laaziri *et al.* [157, 161]) and electron-beam evaporation (Cox-Smith *et al.* [168] and Zink *et al.* [14]). These two methods produce a-Si thin-films of comparable "quality" and properties, whereas sputtered a-Si gives a Young's mode velocity of 4.4 ± 0.5 nm/ps [169], for example.

Expt.	Q , K/ps	ρ , nm $^{-3}$ [167]	r_p , Å[161]	σ_r , Å[161]	θ_p , °[161]	σ_θ , °[161]	C [161]	v_γ , nm/ps[168]	v_L , nm/ps[14]	k , W/mK[14]
		49.00 ± 0.05	2.352 ± 0.001	0.031 ± 0.001	107.83 ± 0.97	9.63 ± 0.08	3.881 ± 0.004	6.31 ± 0.07	7.51 ± 0.30	1.5 ± 0.4
SW	0.10	50.83	2.374	0.002	108.57	0.14	4.270	5.56	8.21	1.6
	1.00	51.89	2.396	0.003	107.84	0.14	4.396	5.41	8.41	1.6
	10.00	53.04	2.428	0.004	106.60	0.27	4.526	5.27	8.67	1.6
100.00	54.10	2.461	0.004	104.85	0.26	14.69	4.663	5.11	8.97	1.5
VBWM	0.10	47.78	2.373	0.002	108.94	0.09	4.005	6.28	7.52	2.7
	1.00	47.57	2.377	0.001	108.77	0.07	4.009	6.19	7.49	2.3
	10.00	47.30	2.379	0.001	108.62	0.08	4.013	6.07	7.43	1.8
100.00	46.92	2.386	0.002	108.38	0.10	9.92	5.88	7.35	1.4	
SW115	0.10	48.75	2.366	0.004	109.04	0.25	4.041	5.30	6.85	2.0
	1.00	48.69	2.370	0.001	108.80	0.04	4.066	5.18	6.82	1.7
	10.00	48.88	2.374	0.001	108.55	0.07	4.101	5.05	6.82	1.3
100.00	49.62	2.385	0.001	107.93	0.11	11.12	4.197	4.77	6.86	1.4
Tersoff	0.10	48.88	2.364	0.001	109.33	0.06	4.040	6.31	7.96	2.6
	1.00	48.96	2.365	0.001	109.20	0.05	4.062	6.26	7.92	2.5
	10.00	49.30	2.369	0.001	108.92	0.05	4.111	5.67	7.64	2.3
100.00	50.22	2.382	0.001	108.17	0.19	12.37	4.237	6.23	7.91	2.1
EDIP	0.10	48.22	2.382	0.000	108.86	0.09	4.035	5.27	7.81	1.6
	1.00	48.38	2.386	0.001	108.65	0.10	4.063	5.14	7.74	1.3
	10.00	48.85	2.397	0.002	108.06	0.16	4.131	5.33	8.27	1.1
100.00	49.56	2.426	0.002	106.45	0.25	11.12	4.307	4.38	6.89	1.3

Table 4.6: Thermophysical properties of simulated a-SiO₂ compared to experiment for the M3S [137], BKS [138], and TTAM [139] potentials and quench rates ranging from 100 K/ps to 1 K/ps (BKS and TTAM) or 0.1 K/ps (M3S). The experimental properties are pieced together from Fritz and Graham [170], Inamura *et al.* [171], Mauri *et al.* [164], Love [172], and Cahill and Pohl [173]. Each experimental sample was a variant of fused quartz, the glass obtained by melting and quenching quartz.

Expt.	Q , K/ps	ρ , nm $^{-3}$ [170]	r_p , Å[171]	$\theta_{Si-O-Si}$, °[164]	$\theta_{Si-O-Si}$, °[164]	$\sigma_{Si-O-Si}$, °[164]	v_T , nm/ps[172]	v_L , nm/ps[172]	k , W/mK[173]
		66.17 ± 0.03	1.6027 ± 0.0003	151.4	11.3		3.68 ± 0.10	5.85 ± 0.10	1.23
M3S	0.10	66.93	1.640	0.000	146.67	0.14	3.39	6.45	1.0
	1.00	68.58	1.640	0.000	146.34	0.15	3.38	6.42	1.0
	10.00	69.88	1.641	0.000	145.97	0.07	3.33	6.28	1.0
	100.00	70.72	1.642	0.000	145.41	0.10	3.25	6.09	1.0
BKS	1.00	67.55	1.609	0.000	152.66	0.53	4.11	6.96	2.3
	10.00	68.41	1.610	0.000	151.30	0.56	4.10	6.96	2.1
	100.00	69.53	1.610	0.000	149.39	0.60	4.08	6.98	2.2
TTAM	1.00	65.16	1.645	0.000	152.56	0.42	3.85	6.51	2.1
	10.00	65.66	1.646	0.000	151.61	0.34	3.83	6.50	2.1
	100.00	66.69	1.646	0.000	149.73	0.55	3.82	6.53	2.1

4.6 CONTRIBUTIONS

In this chapter, I systematically evaluated several potentials and quench rates for modeling the thermophysical properties of a-Si and a-SiO₂. While other comparative studies have been conducted of potentials for these material systems [174], particular attention has been paid here to those properties likely to impact the thermal transport, like the structure and acoustic sound speeds. It was determined that the potential of Vink *et al.* [135] provides an adequate representation of a-Si, while none of the tested potentials for a-SiO₂ are satisfactory. Because different quench rates were investigated, this work also provides a wealth of data (each figure and Tables 4.5 and 4.6) that can be further studied in order to understand how the quench rate quantitatively affects the material properties of a glass.

5

EFFECT OF LONG- AND SHORT-RANGE ORDER ON SILICON-GERMANIUM ALLOY THERMAL CONDUCTIVITY

Altering the composition of $\text{Si}_{1-x}\text{Ge}_x$ and other alloys is one route for engineering their thermal conductivity, k [48, 51]. In addition to numerous experimental studies [44, 175–177], there have been many recent computational studies of the thermal properties of $\text{Si}_{1-x}\text{Ge}_x$ using classical molecular dynamics [55, 75, 80, 178–180] and density functional theory [53, 79]. Studies have focused on the dependence of k on composition [53, 178], grain size [80], nanoparticle inclusions [76, 79], and nanowire boundary scattering [78], all in an effort to improve the thermoelectric figure of merit [72, 73]. Alloys possess two additional degrees of freedom for tuning k : the arrangement of the atoms on the lattice as characterized by the long-range [40] and short-range [41] order parameters (see Sec. 2.3). In molecular dynamics studies of a Lennard-Jones alloy, Duda *et al.* showed that the long-range order can be used to tune k over an order of magnitude at low temperatures [70, 71]. Here, I take $\text{Si}_{0.5}\text{Ge}_{0.5}$ as a representative model for semiconductor alloys and report the effect of long-range and short-range order on the thermal conductivity and normal mode relaxation times at 300 K using molecular dynamics simulation.

5.1 STRUCTURE GENERATION AND CHARACTERIZATION

$\text{Si}_{0.5}\text{Ge}_{0.5}$ structures with independently controlled \mathbb{L} and \mathbb{S} were generated with the procedures discussed in Section 2.3. The reference ordered structure was taken as zincblende. While the true ordered structure of $\text{Si}_{0.5}\text{Ge}_{0.5}$ consists of alternating bilayers of Si and Ge in the [111] direction [181], the choice of zincblende is justified since the usage of a single potential for all interactions in these simulations gives all ordered structures equivalent potential energy and many compound semiconductors *do* order into a zincblende structure, *e.g.* those of Vurgaftman *et al.* [67]. Thus, the present structures should primarily be considered as models of a semiconducting alloy and not strictly applicable to $\text{Si}_{0.5}\text{Ge}_{0.5}$ *per se*. Nevertheless, I believe that the findings can and should be cautiously extended to $\text{Si}_{0.5}\text{Ge}_{0.5}$ and other semiconducting alloys for which mass disorder is the dominant scattering mechanism.

For a domain size of 8^3 conventional cells (4096 atoms), order parameters of \mathbb{L} and \mathbb{S}_1 ranging from 0.0 to 0.9 in 0.1 increments were used, with $\mathbb{S}_1 \geq \mathbb{L}$. Since \mathbb{S}_i must converge to \mathbb{L}

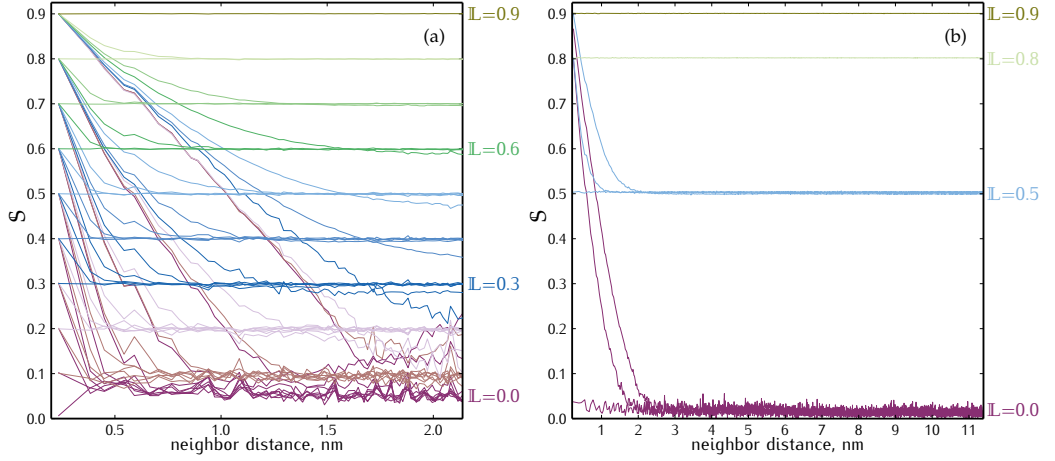


Figure 5.1: Short-range order parameters of simulated $\text{Si}_{0.5}\text{Ge}_{0.5}$ structures generated by a Monte Carlo method. Each color represents a different long-range order and each line is the average of 10 independently generated samples. (a) 8^3 conventional cell domains. (b) 42^3 conventional cell domains.

for large i , the case where $S_i < \mathbb{L}$ is unphysical for the same reason that one cannot multiply a series of fractions and obtain a greater value. Actually, with a sufficient number of atoms for good statistics, $S_i \geq S_{i+1}$ for all i [109]. The case $S_1 > \mathbb{L}$ can be thought of as corresponding to an alloy composed of grains defined by anti-phase boundaries. Then, S_i would scale with the mean grain size and \mathbb{L} would scale with the ratio of volumes occupied by phase and anti-phase grains. For the most mismatched structure, approximately 2.5×10^5 Monte Carlo steps were required for the 8^3 conventional cell domain size, scaling linearly with the number of atoms in the domain. Larger domains were also generated for select (\mathbb{L}, S_1) pairs to take into account the size effect (see Sec. 5.2). These domains had sizes of 12^3 , 18^3 , 28^3 , and 42^3 conventional cells. For each structure (\mathbb{L}, S_1, N^3) , ten independent samples were generated. No consideration has been given to the temperature or configurational entropy of these structures—they are not in equilibrium. Control over \mathbb{L} and S_i in actual $\text{Si}_{0.5}\text{Ge}_{0.5}$ requires a non-equilibrium growth process [69, 182], which is likely the case for other semiconductor alloys too.

The resulting short range order parameters as a function of neighbor distance are plotted in Figure 5.1 for the 8^3 and 42^3 domains. While only S_1 was used as a metric for the Monte Carlo generation, $S(r)$, where r is the neighbor distance, systematically decreases towards \mathbb{L} . One might characterize the approach of $S(r)$ toward \mathbb{L} by a decay length scale, which would be less than 1.5 nm for each structure plotted in Figure 5.1a. In other words, the correlation between distant atoms diminishes with the distance towards a minimal value defined by \mathbb{L} . For structures with $\mathbb{L} = 0$, $S(r)$ is substantially above zero at all neighbor distances. This is a consequence of the small domain size and the choice to define S_i using the square-root (Eq. 2.42). The square-root amplifies the small deviations of $(R_i - W_i)/N_i$ from zero; the deviations of this ratio from the ideal value (defined with respect to \mathbb{L}) were about the same for all structures. The small domain size also inhibits the exact convergence of $S(r)$ to \mathbb{L} when $S_1 \gg \mathbb{L}$. These effects diminish as the domain size increases to 42^3 conventional cells (Fig. 5.1b). The convergence of $S(r)$ toward \mathbb{L} is exact and $S(r)$ for $\mathbb{L} = 0$ is closer to zero, which is consistent with the better statistics afforded by the larger domain size.

5.2 THERMAL CONDUCTIVITY AND SIZE EFFECTS

All simulations were performed using LAMMPS [143] with a time step of 0.5 fs. The zincblende lattice constant was set to 5.43 Å, and the Si and Ge atoms only differed in their masses: 28.09 and 72.64 amu, respectively. The use of a single potential had the further benefit of isolating the effect of mass disorder from strain disorder. The Stillinger-Weber potential [132] (Eq. 4.1) was used for all interactions since the effect of strain on k is small compared to that of mass disorder for $\text{Si}_{1-x}\text{Ge}_x$ [178]. The system was equilibrated at 300 K for 1 ns in a canonical ensemble enforced by a Nosé-Hoover thermostat [183, 184] with a coupling time of 2 ps. The system was then run for an additional 1 ns in a microcanonical ensemble before data were collected for $36 \cdot 2^{17}$ time steps (2.36 ns), printing the conduction term of the heat current every 10 time steps for calculating k [154], and printing atomic velocities every 36 time steps for calculating the normal mode relaxation times, $\tau(\nu)$.

The Green-Kubo method [152, 153] at thermal equilibrium was used to measure k . The direct method would have been prohibitively expensive in computation time for such a large parameter sweep and such a stiff potential (requiring longer simulation domains to obtain the size effect). The convergence time of the heat current auto-correlation function was determined by the *first avalanche* criterion [155] with an averaging window of 8.0 ps (8^3 and 12^3 conventional cell samples) or 40.0 ps (18^3 , 28^3 , or 42^3 conventional cell samples) and a noise-to-signal cutoff of 1000. In a minority of samples, the noise-to-signal never reached the threshold value. In these cases, the maximum in the noise-to-signal determined the convergence time. The cutoff times determined by the first avalanche criterion ranged from ~ 30 to ~ 70 ps for the 8^3 structure, and ~ 200 to ~ 500 ps for the 42^3 structure, depending on the ordering. The longest cutoff times have comparable magnitudes to those of He *et al.*, which were on the order of 400 ps [179]. The uncertainty in k is reported as twice the standard deviation of the ten calculated values for the ten independent samples.

As seen in Figure 5.2, to within the uncertainty, the thermal conductivity depends only on a structure's S_1 , or possibly S_i for small i . Thus, \mathbb{L} affects k to the extent that it sets the lower limit for $S(r)$. Consistent with the low temperature trend observed by Duda *et al.* [71], $\partial k / \partial S_1$ increases as S_1 approaches one. I observe the same trend in k with respect to ordering because the structures investigated by Duda *et al.* [71], which were generated from the definition of \mathbb{L} , always had $S_i \approx \mathbb{L}$ (see Sec. 2.3).

A phonon is insensitive to material heterogeneities with length scales much less than the phonon's wavelength. Instead, these phonons can be thought of as traveling through a *virtual crystal* with effective, averaged properties, *e.g.* density and elastic moduli [51]. *Ab initio* calculations have shown that phonons with frequencies less than 2 THz carry 88% of the heat in $\text{Si}_{0.5}\text{Ge}_{0.5}$ [53]. Making use of the dispersion calculated for an empirical model of $\text{Si}_{0.5}\text{Ge}_{0.5}$ [180], this translates to a phonon wavelength greater than ~ 3.0 nm (longitudinal) or ~ 1.8 nm (transverse) in the present systems. These wavelengths are greater than the $S(r)$ decay lengths of about 1.5 nm or less (Fig. 5.1), which would suggest a reduced dependence of k on S_1 as the system size increases, introducing more long wavelength modes.

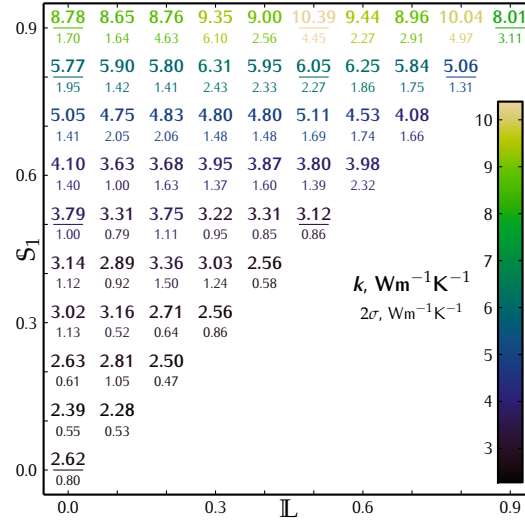


Figure 5.2: Thermal conductivities of 8^3 unit cell $\text{Si}_{0.5}\text{Ge}_{0.5}$ structures with varying long- and short-range order. The thermal conductivity is constant within the uncertainty (2σ) along the rows, indicating that the short-range order is the dominant factor. Underlined data were also studied for size effects (Fig. 5.3).

To check this effect, the linear extrapolation procedure was used to obtain a bulk k value from the size-dependent thermal conductivity having the form: $k(l) \propto l^{-1}$, where l is the cubic domain side length [55, 186, 187]. This procedure is justified if the lowest frequency modes have a relation time proportional to f^{-2} . Figure 5.3 shows the results of the linear extrapolation procedure. The strong dependence of k on S_1 and not L persists out to the bulk limit since the extrapolated points at $l^{-1} = 0$ are arranged by S_1 (marker color) and not L (marker shape). The data of He *et al.* [179] and Larkin [185], which correspond to the completely disordered case of $L = S_1 = 0$, are also plotted. There is good agreement with the data of He *et al.*, who used a Tersoff potential [188] for the atomic interactions. For the cases of $S_1 = 0.0, 0.5$, the slope of $k(l^{-1})$ appears to be flat between about 0.10 and 0.25 nm^{-1} and then increasing closer to the origin. Larkin and McGaughey [55] attribute this trend to poor phonon sampling at the low frequencies leading to a non- f^{-2} relaxation time scaling, so that the relationship $k \propto l^{-1}$ is not valid. But the present calculation of the relaxation times shows that there is indeed a low frequency trend of f^{-2} even for the domain size of 8^3 conventional cells (Fig. 5.5). This matter is discussed more in the next section (Sec. 5.3).

5.3 NORMAL MODE RELAXATION TIMES

The relaxation times, $\tau(\nu)$, were calculated using the normal mode decomposition method [153] in the frequency domain [189]. The atomic trajectories are projected onto the harmonic normal modes (calculated using GULP [156]), then Fourier transformed and fit to a Lorentzian:

$$A \frac{\Gamma(\nu)/\pi}{(f - f_0(\nu))^2 + \Gamma^2(\nu)} = t_f^{-1} |\dot{Q}(\nu, f)|^2. \quad (5.1)$$

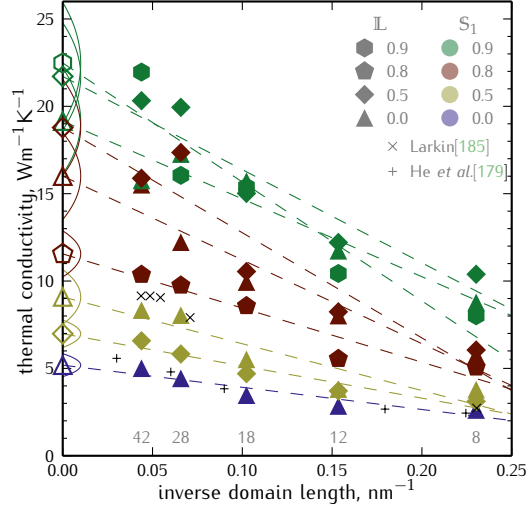


Figure 5.3: Size effects on the thermal conductivity for select $\text{Si}_{0.5}\text{Ge}_{0.5}$ structures. Each filled symbol is the average of 10 samples. The arcs along the k axis indicate the 95% confidence interval of the intercept based on the 50 total samples for each (\mathbb{L}, S_1) pair. The intercepts are ordered by S_1 and not \mathbb{L} , indicating that just as in Figure 5.2, the bulk k is determined by S_1 . Previous studies of the $\mathbb{L}=S_1=0$ alloy are also plotted.

The fit yields $\tau = 1/(4\pi\Gamma)$ and the anharmonic linear frequency, f_0 , for each normal mode, ν . At thermal equilibrium, the coefficient A is guaranteed to be $\frac{1}{2}k_B T$ from the equipartition principle. The duration of data collection, t_f , ought to be much greater than the maximum $\tau(\nu)$ for the material. Of course, t_f must be chosen before the maximal τ is known. \dot{Q} is the Fourier transform of the normal mode velocity coordinate, \dot{q} [29]: $\dot{Q} = \int_0^{t_f} \dot{q} \exp(-2\pi i f t) dt$. Dropping the negative frequency component of $|\dot{Q}(f, \nu)|^2$ caused factors of two in the derivation of Equation 5.1 to cancel. The linear, instead of angular, Fourier transform adds a factor of 2π to the expression for τ ; compare against expressions in [187] and [189]. Due to the sharpness of the peak in $|\dot{Q}|^2$, I increased the weighting near the base by taking the decimal logarithm of each side of Equation 5.1. Only points above 0.104 meV/THz ($1 \text{ amu} \cdot \text{\AA}^2 \cdot \text{ps}^{-1}$) were used in the fit. To hasten the fitting, and to make sure that the global minimum was found, I performed a grid search before regression, with 31 points linearly spaced between ± 0.1 THz of the peak frequency and 31 points logarithmically spaced between Γ of 10^{-5} and 10^{-1} ps^{-1} .

Figure 5.4 demonstrates certain aspects of the application of Equation 5.1 and the fitting procedure for the 8^3 conventional cell, $\mathbb{L} = S_1 = 0$ structure. The energies contained in the normal mode velocity degree of freedom are clustered about $\frac{1}{2}k_B T$ as predicted by the equipartition principle (Fig. 5.4a). The agreement is not exact because of the limited duration (2.36 ns of data collection) and system size (4096 atoms) of the simulation. Theoretically, as the simulation duration increases, the normal mode energies will converge to $\frac{1}{2}k_B T$, so enforcing this value in the fit ought to reduce the variance arising from limited simulation duration and size. The normal mode energies below ~ 3 THz show a much greater variance, which could be due to non-thermalization. Their relaxation times are not significantly shorter than the 2 ns of equilibration before data collection (Fig. 5.5a); the assumption of equipartition for these modes may not be as valid as for the higher frequency modes. Vertical bands in the 0–3 THz range are the result of discrete normal mode sampling caused by the small system size. The

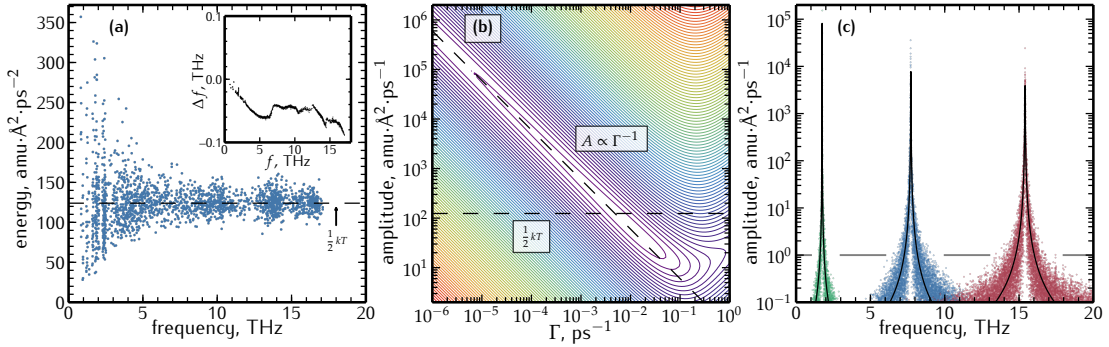


Figure 5.4: Fitting of normal mode velocity coordinate power spectral density to obtain relaxation times, $\mathbb{L} = \mathbb{S}_1 = 0$ structure. (a) Normal mode energy compared to expectation value of $\frac{1}{2}k_B T$ from equipartition. Inset: Anharmonic frequency shifts. (b) Fitting error contours for different Lorentzian amplitudes and line widths. Fitting of line width and anharmonic frequency was conducted for fixed amplitude equal to $\frac{1}{2}k_B T$. (c) Normal mode velocity coordinate spectra of three modes along with corresponding fits. Spectrum above $1 \text{ amu}\cdot\text{\AA}^2\cdot\text{ps}^{-1}$ was used in the fits.

inset of Figure 5.4a shows the shift in frequencies of the modes relative to their frequencies calculated by harmonic lattice dynamics [29, 156]. The frequencies are suppressed by less than 0.1 THz for all the modes, reflecting the stiffness of the Stillinger-Weber potential and the role of anharmonicity in dampening the normal mode vibrations.

The sensitivity of the fit to the coefficient, A , and line-width, Γ , is shown in Figure 5.4b. The peak frequency was kept fixed at the value corresponding to the greatest magnitude in the normal mode spectral power density (the right-hand-side of Eq. 5.1, visualized in Fig. 5.4c). The error in the fit is nearly constant for $A \propto \Gamma^{-1}$ across several orders of magnitude, indicating that the two parameters are nearly indistinguishable. Thus, not only does fixing $A = \frac{1}{2}k_B T$ reduce the fitting from three variables to two, but it also ensures that even in the presence of some noise, the correct values of Γ and f_0 may be found. Finally, Figure 5.4c shows the normal mode power spectral density (right-hand-side of Eq. 5.1) compared to the Lorentzian fit (left-hand-side of Eq. 5.1) for three modes. The broadening of the low-amplitude portion of the tails justifies the choice of $1 \text{ amu}\cdot\text{\AA}^2\cdot\text{ps}^{-1}$ for the lower threshold of data used in the fitting.

To justify the use of the linear extrapolation procedure and further explore the dependence of k on \mathbb{S}_1 , Figure 5.5 shows the normal mode relaxation times. Figure 5.5a compares my results for the completely disordered structure to previous molecular dynamics simulations using normal mode decomposition [55, 179, 180]. Though each work investigated $\text{Si}_{0.5}\text{Ge}_{0.5}$ thermal conductivity at 300 K, slightly different simulation and fitting procedures were used. My relaxation times agree with those of Hori *et al.* [180]. The agreement with He *et al.* [179] is also good, especially considering their use of a Tersoff potential [188] instead of the Stillinger-Weber potential. The relaxation times of Larkin and McGaughey [55] are significantly shorter than the others, although a similar trend is shown. The disagreement may be due to their use of the virtual-crystal modes for the normal mode decomposition. The disagreement, however, is perplexing since their calculations of k using the virtual-crystal normal mode relaxation times are self-consistent with the k calculated by the Green-Kubo method, as plotted in Figure 5.3 and Larkin's dissertation [185]. Furthermore, the virtual-crystal approximation with

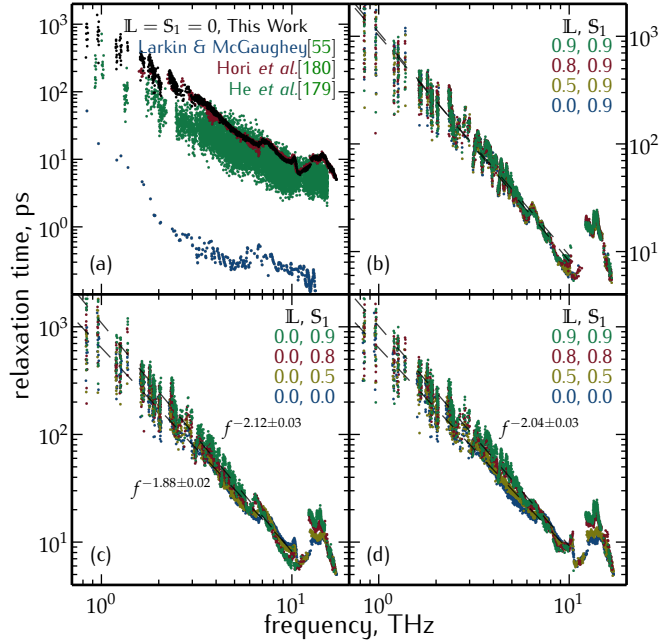


Figure 5.5: Mode relaxation times for slices through \mathbb{L} - S_1 parameter space. (a) Comparison of our fully disordered SiGe structure to previous results. (b) Constant S_1 slice. The majority of modes are unaffected by \mathbb{L} . (c) Constant \mathbb{L} slice. All modes are sensitive to S_1 . (d) $\mathbb{L}=S_1$ slice. The relaxation times are nearly identical to those of (c), in agreement with the thermal conductivity trends of Figures 5.2 and 5.3.

ab initio force constants produced k values consistent with experiment at 300 K in the work of Garg *et al.* [53].

Figures 5.5b,c and Figure 5.5d show the mode relaxation times for two paths between the ordering extrema: $(\mathbb{L}, S_1) = (0.0, 0.0) \rightarrow (0.9, 0.9)$. That Figures 5.5c and 5.5d are so similar, and Figure 5.5b shows no significant change in $\tau(\nu)$ with \mathbb{L} , supports the conclusion of Figures 5.2 and 5.3: S_1 accounts for the entire change in k upon ordering.

The relaxation times below 10 THz are roughly fit by an f^{-2} power law (Figs. 5.5b-d). The fitted exponents fell within -2 ± 0.15 for each plotted (\mathbb{L}, S_1) pair. The relaxation times below ~ 1.5 THz have a greater variance for two reasons. The total simulation time (4.36 ns) was comparable to the fitted relaxation time, so these modes are non-thermalized, invalidating the assumption of equipartition for those modes. The relaxation times are also comparable to the period of data collection, reducing the accuracy of the fit. It is likely that the power law trend in this regime continues as f^{-2} but with a reduced variance [51, 53], although this cannot be verified by the present simulations.

Figures 5.5c and 5.5d also show a change in the character of the relaxation times, especially in the range of 3 to 6 THz. The curve is smooth for $S_1=0$. But as S_1 increases, peaks and valleys form where the momentum and energy selection rules for phonon scattering become more and less restrictive. Furthermore, a bandgap forms at ~ 11 THz.

I therefore attribute the dependence of k on S_1 (instead of \mathbb{L}) to the alteration of the phonon eigenvectors caused by short-range ordering. As S_1 increases, the eigenvectors approach those of the zincblende crystal. While high frequency modes might significantly contribute to k in the limit $S_1 \rightarrow 1$, most of the increase for the ordering range studied here is caused by a reduc-

tion in the anharmonic scattering of the low frequency modes. The reduction in anharmonic scattering may be due to fewer states that satisfy momentum and energy selection rules, a reduction in the scattering cross-section, or both mechanisms. The same trend of k with disorder was observed by Garg *et al.*, who saw a reduction in k with greater disorder when they went from a virtual crystal to an explicitly disordered supercell [53]. They found that the change in k was due to altered mode relaxation times, caused by a modification of the mode eigenvectors.

These findings may be cautiously applied to real $\text{Si}_{0.5}\text{Ge}_{0.5}$ and cautiously generalized to other simulated and real alloys provided that the thermal conductivities of their disordered states arise primarily from the same mechanisms as those found in the present model of $\text{Si}_{0.5}\text{Ge}_{0.5}$, namely the scattering of lattice vibrations by mass disorder. That k depends almost solely on S_1 has implications for the characterization and theoretical modeling of alloys that primarily transport heat by lattice vibrations. When examining an alloy with the purpose of understanding or predicting its thermal conductivity, a characterization technique sensitive to the short-range order must be used, *e.g.* diffuse X-ray scattering [190]. Similarly, future efforts to theoretically model thermal transport in ordered alloys should focus on the short-range order or its effect on anharmonic phonon scattering.

In summary, I performed molecular dynamics simulations of a $\text{Si}_{0.5}\text{Ge}_{0.5}$ alloy, representing a model semiconductor alloy, and calculated the thermal conductivity as it depends on the long- and short-range ordering. I found that the bulk thermal conductivity depends almost wholly on the short-range order of the alloy for a fixed composition. Relaxation time calculations support this dependence. Changes in the character of the mode relaxation times upon ordering imply that the corresponding increase in thermal conductivity is caused by a reduction in disorder-induced anharmonic phonon scattering.

5.4 CONTRIBUTIONS

Per the opening paragraph of this chapter, there have been a number of experimental and theoretical works investigating the thermal conductivity of SiGe alloys and the alloy's dependence on a variety of structural modifications. This work extends the recent trend of research on SiGe by testing the effect of long- and short-range order parameters on the thermal conductivity. Furthermore, to my knowledge, this is the first work investigating the effect of the short-range order on any alloy whose thermal conductivity is due to lattice vibrations. By decoupling the short-range order from the long-range order, I was able to show that the dependence on long-range order that Duda *et al.* observed [71] is actually most likely implicitly due to the short-range order of the structures they investigated. The finding that the short-range order solely determines the thermal conductivity will help guide future theories of transport in non-metallic alloys with intermediate ordering, where neither the virtual crystal approximation nor traditional phonon transport theories are valid.

6

FREQUENCY DEPENDENT VIBRATIONAL DIFFUSIVITY OF AMORPHOUS SILICON AND SILICA CALCULATED WITH THE WAVELET TRANSFORM

In Section 1.2 I briefly discussed the competing theoretical frameworks for predicting thermal transport in amorphous materials at high temperatures. Chief among these frameworks are the Cahill–Pohl (C–P) model [7, 32] and the Allen–Feldman (A–F) theory [25–28].¹ In this chapter, I apply the new simulation method of Section 3.3 to a model of amorphous silicon (a-Si) and compare the prediction to those of the C–P model and the A–F theory. I also apply the method to a model of amorphous silica (a-SiO₂).

6.1 THE CAHILL–POHL MODEL AND ALLEN–FELDMAN THEORY

In this section I elaborate on the C–P model and the A–F theory and discuss their respective strengths and weaknesses. The objective is not to give a complete derivation and interpretation, but to merely provide sufficient background to give the following results context. Interested readers should look to the primary sources for further details [7, 25–28, 32].

The C–P model assumes that heat is carried by non-dispersive phonons having either a longitudinal or transverse polarization and traveling at the longitudinal and transverse acoustic sound speeds, or v_L and v_T , respectively. It is then assumed that the disorder of the amorphous structure causes the phonons to scatter with a relaxation time equal to half their vibrational period. Because the velocities of the phonons depend only on the polarization and are constant within a branch of the dispersion, the above assumption is the same as assuming the phonons scatter with a mean-free-path of one-half their wavelength. The expression for average frequency-dependent diffusivity, $D(f)$, according to the assumptions of constant acoustic velocities for the phonons and the above relaxation time is:

$$D(f) = \frac{1}{18} f^{-1} (v_L^2 + 2v_T^2), \quad (6.1)$$

¹ For completeness' sake, the *fracton* model [191–195] was another theoretical approach applied to amorphous materials, although it has since fallen out of favor and will not be considered here.

where f is the linear frequency. The factor of one-eighteenth comes from the product of: one-half from the assumed relaxation time; one-third from averaging over the three polarizations; and another one-third from geometrical averaging, *i.e.* the same term as in the classic equation of the phonon-gas model [196]: $k = \frac{1}{3}Cv\Lambda$, where C is the heat capacity, v is the average phonon velocity, and Λ is the mean-free-path.

If the averaging in Equation 6.1 is not carried out, the C–P model prediction of the thermal conductivity is [32]:

$$k = \left(\frac{\pi}{6}\right)^{\frac{1}{3}} k_B n^{\frac{2}{3}} \sum_i v_i \left(\frac{T}{\Theta_i}\right)^2 \int_0^{\frac{\Theta_i}{T}} \frac{x^3 e^x}{(e^x - 1)^2} dx \quad (6.2)$$

where k_B is Boltzmann's constant, n is the number density of atoms, i indexes the polarizations (one longitudinal and two transverse), v_i is the acoustic sound speed, T is temperature, and Θ_i is the Debye temperature equal to $v_i(\hbar/k_B)(6\pi^2n)^{\frac{1}{3}}$ and \hbar is the reduced Planck's constant.

The C–P model has two great strengths. The first is that Equation 6.2 makes its prediction based on only three material-dependent properties: the atomic number density, and the longitudinal and transverse sound speeds. Each of these properties is easily measured. The second is that Equation 6.2 has a simple analytical form and is easily calculable. To achieve such a simple form that depends on only a few material properties, the C–P model sacrifices all details of the disordered structure of an amorphous material. Per the discussion in Section 1.1 and the vast quantitative and qualitative differences between the thermal conductivities of crystalline and amorphous polymorphs seen in Figure 1.1, the disordered arrangement of atoms must have a more profound impact than merely imposing a relaxation time of one-half the vibrational period on the phonon transport. Correctly incorporating information regarding the amorphous structure should improve the fidelity of a future theoretical model. Nevertheless, the C–P model gives adequate predictions of the high temperature thermal conductivity of amorphous materials [32].

The A–F theory calculates the vibrational eigenmodes for a simulated model of the amorphous material. Spatially adjacent quasi-localized modes that have the same frequency couple with each other to transport the heat. The one free parameter of the theory is the width of the Lorentzian function that allows the modes of a finite system, which have small but finite frequency differences, to couple together. The formula for diffusivity is:

$$D(\omega_i) = \frac{\pi V^2}{3\hbar^2 \omega_i^2} \sum_{j \neq i} |S_{ij}|^2 \delta(\omega_i - \omega_j) \quad (6.3)$$

where i and j index the normal modes, ω is the angular frequency, V is the system volume, and S_{ij} are the matrix elements of the heat current operator calculated by a lattice dynamics formalism [26]. The authors also note that for a finite system, as is encountered in the practical calculation of Equation 6.3, the delta function must become a Lorentzian of a width greater than the frequency spacing of the discrete normal mode frequencies ω_i . Equation 6.3 may be interpreted as a measure of the overlap between nonlocalized and spatially adjacent vibrational eigenvectors [149]. These modes do not normally interact in the harmonic ap-

proximation [30], being eigenmodes of the system, but are coupled together by the heat flux through the system [26]. Then, the modes act like linkages in a chain to pass along energy, to use a simplistic mental picture.

The calculation of the thermal conductivity from Equation 6.3 is a direct summation over each mode [26]:

$$k' = \frac{1}{V} \sum_i C_i D_i \quad (6.4)$$

where C_i is the heat capacity of mode i calculated from the Bose-Einstein distribution: $C_i = (\partial U_i / \partial T)_V = \partial / \partial T [\hbar \omega_i (\exp(\hbar \omega_i / k_B T) - 1)^{-1}]_V$ [196]. Equation 6.4 can also be evaluated as an integral over frequency by incorporating the density of states in the ordinary way [27]. The thermal conductivity k' given by Equation 6.4 results from the contribution of only the non-propagating diffusons. The diagonal elements of \mathbf{S} give the heat transported by propagons, which for all intents and purposes behave like phonons. Thus the total k of the amorphous material is the sum of the diffuson contribution (Eq. 6.4) and the propagon contribution calculated using a phonon-gas model [26].

In contrast to the C–P model, the A–F theory takes into account the exact structure of the amorphous material because the locations of the atoms and the bonding between them are needed to evaluate S_{ij} in Equation 6.3. Furthermore, the A–F theory is rigorously derived from condensed matter physics, and so its predictions may be taken as true to the extent that the studied system lies within the scope of its derivation, which is quite general. This is not the case for the C–P model, which has no rigorous justification for the assumed relaxation time other than that it gives decent predictions of the experimental data.

The A–F theory’s use of the exact microstate, *i.e.* atomic positions and force constants, of the system is also a shortcoming, as such information will never be obtainable for a real material. While *ab initio* methods have been successfully applied to the calculation of force constants and prediction of thermal conductivity in crystals [197, 198] and disordered alloys [53], such approaches cannot rely on a small unit cell or virtual crystal approximation for the disordered structure of a glass. The severe scaling of *ab initio* methods [87] would then make calculations on systems having hundreds to thousands of atoms either impractical or impossible for currently available computing power.

There are three steps in the calculation of the A–F theory prediction which consume the majority of the computational time: 1) reduction of the $3N \times 3N$ dynamical matrix to a tridiagonal form; 2) diagonalization of the tridiagonal matrix, *i.e.* finding all eigenvalues and eigenvectors; and 3) matrix multiplication of the dynamical matrix with the eivenvector matrix (Eqs. A5 or A8 of Ref. [26]). Each of these operations requires $\mathcal{O}(N^3)$ for a direct implementation [199]. The reduction of the dynamical matrix to tridiagonal form may be carried out with the *Householder reduction*, which is $\mathcal{O}(N^3)$ [199]. Finding the eigenvalues and eigenvectors can be done in $\mathcal{O}(N^2)$ calculations with the *Multiple Relatively Robust Representations* algorithm, but the A–F theory implementation in GULP [156] currently uses the $\mathcal{O}(N^3)$ *implicitly shifted QR/QL algorithm* [199].² Finally, multiplication of square matrices by the routines found in BLAS is $\mathcal{O}(N^3)$. Although the *Strassen* and *Coppersmith-Winograd* algorithms have better scaling ($\mathcal{O}(N^{2.807})$) and

² see GULP source file pdiagg.f90 [156] and LAPACK documentation

$\mathcal{O}(N^{2.376})$, respectively), the former cannot necessarily take advantage of modern computer processor hardware to the same extent as optimized BLAS routines and has issues of numerical stability, and the latter has no practical implementation. Thus, the number of calculations required by an A–F theory prediction is $\mathcal{O}(N^3)$. Furthermore, the memory requirement to store the dynamical matrix and eigenvector matrix scales as $\mathcal{O}(N^2)$, which may be the limiting factor depending on the particular computer. These scalings limit the system sizes to tens of thousands of atoms even if empirical potentials describe the forces.

Lastly, to construct the dynamical matrix, the force constants must be known. Analytical forms for the force constant may not be available for complicated potentials. Although the force constants may be found for an arbitrary potential using the method of finite differences, as is done for first-principles calculations [197, 198], having to carry out this process adds an impediment to the calculation.

A successor to the C–P model and the A–F theory ought to contain aspects of both. Unlike the C–P model, it should use details of the amorphous structure, like the radial distribution function (Sec. 4.2, Figs. 4.1 and 4.5), but not require the exact microstate, unlike the A–F theory. The theory should depend on assumptions that are physically justifiable, like the A–F theory, yet also have a tractable analytical form, like the C–P model, to provide usable intuition to the engineer and researcher. In this chapter, I apply the new simulation method described in Section 3.3 to calculate the frequency-dependent vibrational diffusivity of a-Si and a-SiO₂. The new method requires only $\mathcal{O}(N)$ calculations and memory to obtain $D(f)$ and the force constants need not be known, marking a significant improvement over the A–F theory. In this sense, it serves as a step towards the new theory we seek. While still computationally expensive, the superior scaling of the method permits study of much larger systems that have on the order of tens of millions of atoms. Such a large system size avoids the finite size effects that contaminate A–F theory predictions of modes with frequencies of a few terahertz or less, *i.e.* propagons.

6.2 SIMULATION DETAILS

This section gives the details regarding the generation of the amorphous structure, simulation procedure, and analysis parameters employed in the method of Section 3.3 to calculate the frequency-dependent vibrational diffusivity of a-Si and a-SiO₂. The a-Si was modeled with three potentials to observe the effect of the bonding on the transport: the VBWM potential [135], which was shown in Section 4.3.1 to give thermophysical properties in agreement with experiments; the SW potential [132], which has a greater longitudinal sound speed but slower transverse sound speed compared to the VBWM (Table 4.5); and a potential whose two-body and three-body energy terms are the geometrical average of the VBWM and SW potentials. The a-SiO₂ was modeled with the BKS potential [138]. While the agreement between the BKS potential and experiment is not as good as that between the VBWM and experimental

a-Si, it is widely used in the literature and is adequate for demonstrating the independence of the present method with regard to material system.

The amorphous structure was generated in two ways to test the effect of the structure. The first was by quenching the liquid phase using the same procedure described in Section 4.2. The quench rate for the VBWM, “average,” and BKS potentials was 10 K/ps and for the SW potential it was 1 K/ps.³ The second way of obtaining the amorphous structure was by a modification to the Wooten-Winer-Weaire algorithm (WWW) [150] by Barkema and Mousseau [200]. The algorithm systematically rearranges bonded atoms so as to induce disorder. An atomic coordinate file from Mousseau⁴ was taken as the initial configuration. Because the potentials I used were different from the one used to create the structure, it had to be minimized to a new ground-state. This was done by applying a fictitious viscosity of 10 meV·ps/Å² and running the simulation for 15 ps in the NPH ensemble, as in Section 4.2.

For the quenching method of structure generation, a-Si simulations began with 23³ conventional cells of silicon in the diamond cubic structure, giving 97,336 atoms and a side length of ~12.5 nm. The a-SiO₂ quenching simulations began with 16³ conventional cells of the β -cristobalite structure, giving 98,304 atoms and a side length of ~11.4 nm. The WWW structure contained 100,000 atoms. Very large domains of quenched VBWM and quenched SW were constructed by repeating the 97,336 atom structures five times in each dimension, giving ~12 million atoms and a side length of ~62.5 nm. The objective of these large scale domains is the observation of propagon-like transport.

The final ground-state structures so obtained were the input to the simulation described in Section 3.3. Again, each simulation was run with LAMMPS [143] with a time step of 0.5 fs. In each simulation, one single atom was selected as the epicenter and received a small amount of kinetic energy while all other atoms began with zero kinetic energy. The simulation was then run for 3 ps for the ~100k atom domains and 10 ps for the large-scale domains. The velocity vectors of each atom within a sphere of radius $L/2$ of the epicentral atom, where L is the minimum of the domain dimensions, were printed every 30 time steps for “small-scale” a-Si, 20 time steps for a-SiO₂, and 90 time steps for the large-scale a-Si simulations. The printing interval serves as the Δt term of Equation 2.7 and should be chosen based on the largest frequency to be analyzed by the wavelet transform. Because only small frequencies were of interest in the large-scale simulations, the printing interval was made as long as possible to prevent the creation of excessively large data files.

For the small-scale simulations, the mother wavelet frequency was set to 2.0 THz and the η parameter was conservatively set to 0.05 [98]. In combination with the printing interval, this corresponds to a maximum analyzable frequency of 27.9 THz for a-Si and 41.8 THz for a-SiO₂ (Eq. 2.7). These frequencies are above the cutoff frequency of the material (Figs. 4.4 and 4.7). A mother wavelet frequency of 0.8 was used for the large-scale simulations with an η of 0.05, corresponding to a maximum analyzable frequency of 7.5 THz. The minimum analyzable

³ I found that the structure generated for the SW potential with a quench rate of 10 K/ps was on the verge of metastability. I inferred this from the later transient simulation which showed a sudden appearance of energy after about a picosecond. The explanation is that the perturbation from the applied pulse disturbed an atom or group of atoms, causing rearrangement and release of potential energy.

⁴ private communication

frequency is determined by the duration of the simulation. The time dependent velocities were zero-buffered such that the number of points was a power of two (to take full advantage of the FFT algorithm [101, 199]). The small-scale simulations were buffered to a length of 2^9 printing steps, giving buffered durations of 7.68 ps and 5.12 ps for a-Si and a-SiO₂, respectively. With $\phi = 1$, Equation 2.6 gives a minimum analyzable frequency of 1.56 THz and 2.34 THz, respectively. The large-scale simulations were also buffered to a length of 2^9 printing steps, giving a minimum analyzable frequency of 0.21 THz.

In evaluating Equations 3.8 and 3.9, the width of the Gaussian initial condition was set to 0.75 Å, which is less than the nearest neighbor distance in a-Si (Fig. 4.1) and a-SiO₂ (Fig. 4.5). The radius, R , in the solution was set to the greater of $L + 5$ Å and $v \cdot l_t + 5$ Å, where l_t was the duration of the system (3 or 10 ps). Equation 3.8 was computed for a grid of time and radius values equal to those produced by the simulation. A grid of velocity and relaxation rate values were tested to determine the initial point for the fitting procedure. The initial values of velocity and relaxation rate for the fitting were determined as those that minimized the error with the data for a grid of values spanning velocities of 0.5 to 10 nm/ps and relaxation rates of 0 to 100 ps⁻¹ in increments of 0.5 nm/ps and 10 ps⁻¹, respectively.

The only remaining parameters of the simulation and analysis pertain to the epicenter atom. The amount of kinetic energy (or velocity) imparted to it at the beginning of the simulation, the direction of the applied energy, and which atom is chosen as the epicenter must be specified. The impact of these choices is explored in the next section.

6.3 THE EFFECT OF PING DIRECTION, ATOM, AND MAGNITUDE

The effect of the atom chosen as the epicenter, the amount of energy imparted to it at the beginning of the simulation, and the orientation of this energy were investigated for the small-scale a-Si WWW VBWM sample. In the remaining discussion, I refer to the deposition of energy into the epicenter atom as “pinging” the atom. The effects of the ping direction, pinged atom, and ping magnitude are examined in Figures 6.1–6.3 based on five independent trials for each. For the test of whether ping direction affects the fitted frequency-dependent vibrational diffusivity, a single atom was randomly selected as the epicenter. In each case, the magnitude of the ping remained constant at 1.0 Å/ps (~ 1.5 meV of kinetic energy). The only difference was that the direction of the ping was randomized. As shown in Figure 6.1, the resulting frequency-dependent vibrational diffusivity profiles display no qualitative differences. Thus, the effect of ping direction may be interpreted as contributing to the uncertainty of the fitted curve.

In the next test, a different atom within the same exact sample was randomly selected to be the epicenter for each trial. The magnitude was again consistent between trials at 1.0 Å/ps and the ping direction of each trial was random. Because of the disorder of the amorphous phase, each atom has no orientational preference, justifying the choice of a random direction for each trial. Again, as shown in Figure 6.2, there is no qualitative difference between the trials.

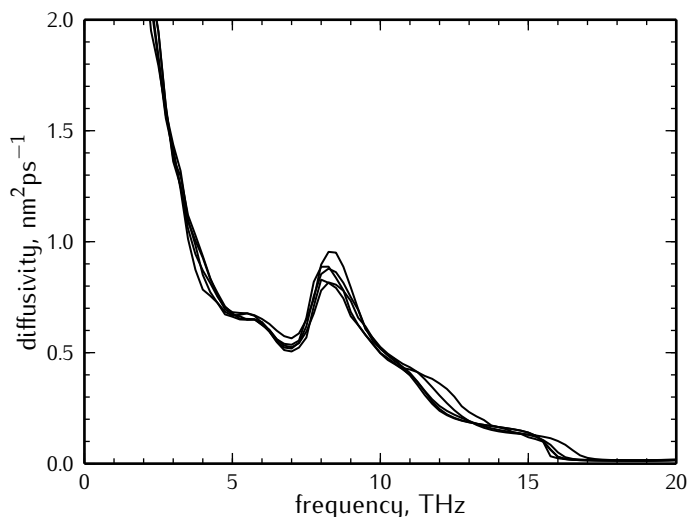


Figure 6.1: Effect of initial velocity vector direction on the calculated a-Si frequency-dependent vibrational diffusivity. Each trial used the same atom and the same magnitude of $1.0 \text{ \AA}/\text{ps}$

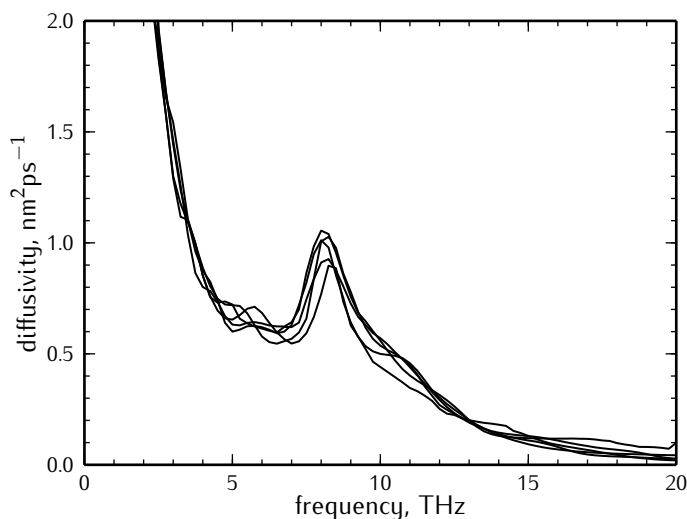


Figure 6.2: Effect of the atom receiving initial energy on a-Si frequency-dependent vibrational diffusivity. Each trial used the same magnitude of $1.0 \text{ \AA}/\text{ps}$ and a random direction.

However, qualitative differences between Figures 6.2 and 6.1 do exist. Most notably, Figure 6.1 has a slight, systematic hump at 6 THz and a series of steps at 11.5 THz and 16 THz. These features are absent from Figure 6.2, meaning that they may have some sort of dependence on the atom at the epicenter. In any case, those features are only slight and Figures 6.1 and 6.2 show the same trend.

The effect of the ping magnitude is shown in Figure 6.3. Ping velocities of 0.01, 0.1, 1.0, 10.0, and $25.0 \text{ \AA}/\text{ps}$ were tested, corresponding to the energies listed in the legend of Figure 6.3. Velocities higher than this approach the energies of the Si-Si bonds. Any atomic rearrangements invalidate the assumptions behind the simulation and analysis. In each simulation, the same atom was pinged, and the ping direction also remained constant and parallel to the z-axis of the simulation. Again, there is little difference in the resulting trends. The largest magnitude ping somewhat disagrees with the other four at frequencies below 3 THz and in the height of

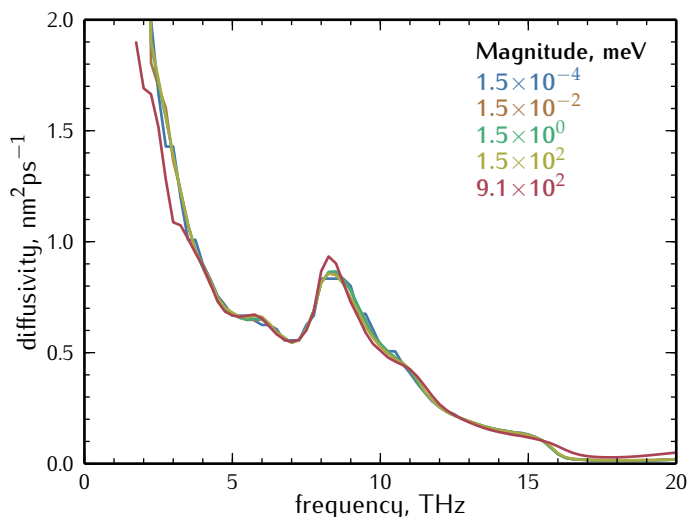


Figure 6.3: Effect of initial velocity vector magnitude on the calculated a-Si frequency-dependent vibrational diffusivity. Each trial used the same atom and the velocity was aligned with the z-direction.

the peak at ~ 8 THz. The smallest magnitude ping shows qualitative differences to the others: in a few places its diffusivity changes in discrete jumps instead of smoothly. This is likely a numerical artifact caused by the printed velocities approaching the precision used to record them in the data file. Thus, ping velocities in the range of about 0.1 to 10.0 Å/ps are suitable.

Based on the findings of Figures 6.1–6.3, the remaining simulations used a ping magnitude of 1.0 Å/ps. The uncertainty of the obtained frequency-dependent vibrational diffusivity was determined by performing trials with different epicenter atoms of the same structure, with each trial using a random ping orientation.

6.4 RESULTS AND DISCUSSION

Figure 6.4 shows the raw time-radius-frequency energy distribution generated by the wavelet transform of the atomic velocities (Sec. 3.3) compared to fits to the analytical solution to the diffusive wave equation (Eqs. 3.7–3.9) for the large- and small-scale quenched VBWM a-Si samples. In Figure 6.4a, the linear relationship between the radius and the time signifies ballistic transport. Extracting the linear trend gives a velocity of ~ 4 nm/ps, in agreement with the transverse sound speed of this simulated material (Table 4.5 and converting from v_T and v_L). As the wave propagates, it continuously loses energy to scattering, which can be seen by the dimming of the linear trend over time and the resulting “fan” that develops at shorter radial distances for a given time.

At higher frequencies, Figures 6.4b–d display no such ballistic transport of energy. Rather, the energy distribution is intrinsically diffusive, consistent with the A–F theory. At 18 THz (Fig. 6.4e), the energy no longer propagates at all. The frequency slices of the energy distribution plotted in Figure 6.4 correspond to key features in the frequency-dependent vibrational diffusivity, as seen in Figures 6.1–6.3.

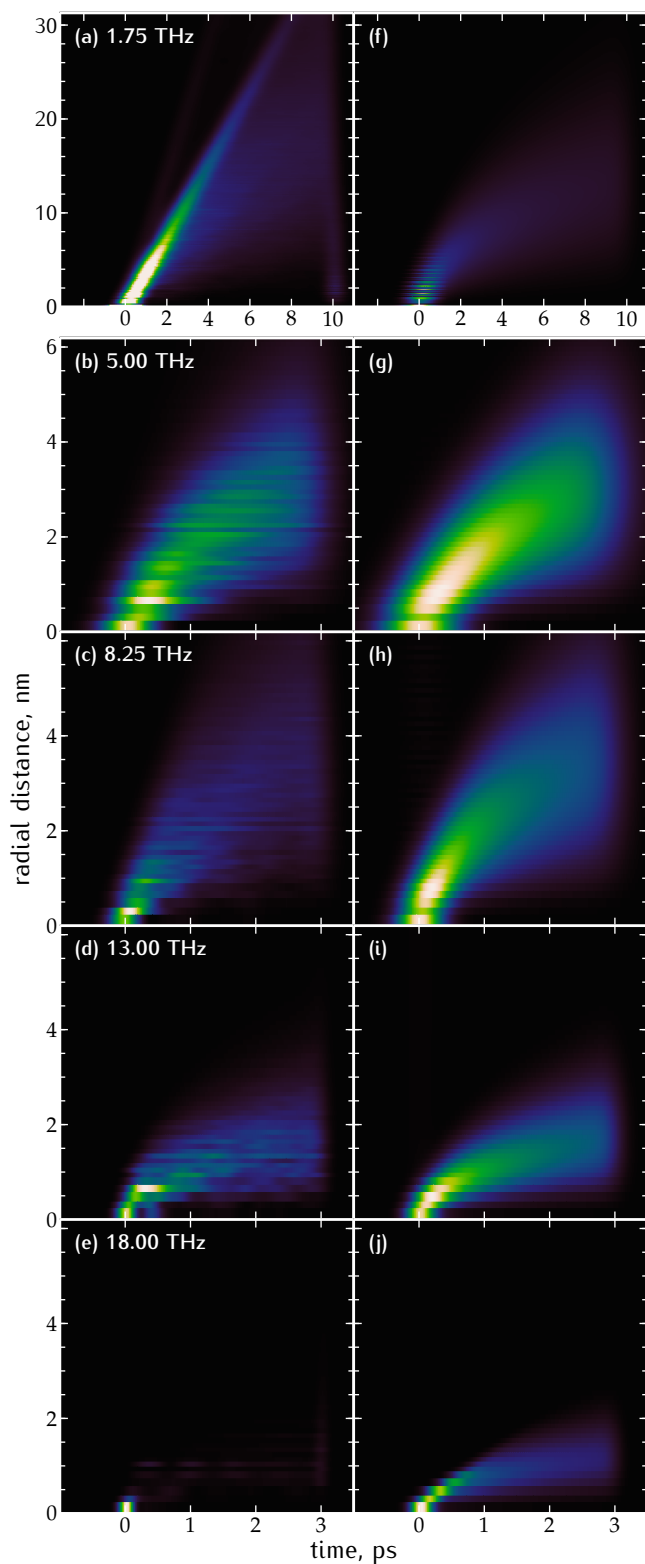


Figure 6.4: Fitting of wavelet transformed transient heat decay to analytical transport model. The left column is the data and the right column is the best fit to Equation 3.8. (a–e) Frequency slices of the time-radius-frequency energy distribution. The energy density of each slice has been normalized. Note the change in time- and radius-scales between (a) and (b–e). (f–j) Corresponding best fits of Equation 3.8 to the data.

Figures 6.4f–j show the fits of the analytical solution to the data for the same frequencies. Figures 6.4b–d are well fit by the analytical solution. Although the magnitude of the energy appears to diminish more rapidly than in the analytical model, the overall shape is the same. Figure 6.4f appears to under-predict the low-frequency diffusivity. The analytical solution can accommodate the ballistic energy transport found in Figure 6.4a, so some detail of the fitting procedure has prevented it from finding the correct parameters. The explanation may involve the artifacts near the origin: horizontal bars of greater and lesser energy.

These bars are likely due to sampling effects. The analytical solution is calculated on a grid of time and radial distance points that are the same as for the data. In the limit of purely ballistic transport, *i.e.* $v \gg \gamma$, the solution for the energy distribution is a “ridge” or line of constant slope. When a grid point lies on this line, a large magnitude of the energy is found. But when the grid point is off by a little, the solution gives no energy. Even though the initial distribution was modeled as a Gaussian (Sec. 3.3), this effect still occurs. Then, after the blurring in time caused by the wavelet transform is incorporated, the bands appear. Overcoming this difficulty will require a more sophisticated sampling method. Two approaches might be to compute the analytical solution on a more densely populated grid, or to use the velocity of the analytical solution to define the placement of grid points such that they do lie on the line of constant velocity.

The lack of transport at high frequencies, *e.g.* 18 THz as shown in Figure 6.4e, cannot be naturally accommodated by the analytical solution. This leads to an over-prediction of the diffusivity, as seen in Figure 6.4j. This issue might be resolved by testing an alternative solution that consists of only a spike at the origin. If the alternative solution fits the data more accurately, then the diffusivity would be defined as zero for that frequency. The difficulties discussed above fall into the category of technical challenges and are not intrinsic to the simulation method itself. Exploration of the proposed solutions will likely resolve the difficulties and improve the accuracy of the fitted frequency-dependent vibrational diffusivity.

One final note is that the analytical solution is only sensitive to both the velocity and the relaxation rate near the origin, with this region defined by a box with sides on the order of a half a nanometer and half a picosecond. Since the radial distribution function has sharp features in this region (Fig. 4.1), corresponding to more discrete placement of the atoms with respect to the epicenter, the continuum approximation necessary for the analytical solution is least valid near the origin. This, combined with the large span of time-radius data that lies outside the origin region, makes the fit sensitive to only the diffusivity, *i.e.* v^2/γ .

Details in the fitting procedure aside, the fitted diffusivities can now be compared against the predictions of the Allen–Feldman theory and the Cahill–Pohl model. An A–F theory calculation was performed using GULP [156] for an 8^3 conventional cell model of a-Si obtained in the same way as the small-scale quenched VBWM sample. The width of the Lorentzian was set to five times the average spacing of the eigenmode frequencies [149]. The C–P model prediction of diffusivity (Eq. 6.1) was also carried out using the longitudinal and transverse velocities of the small-scale quenched VBWM sample from Table 4.5. To account for the frequency blurring introduced by the wavelet transform, the same blurring was applied to the A–F theory prediction and the C–P model. Interestingly, since the frequency blurring in-

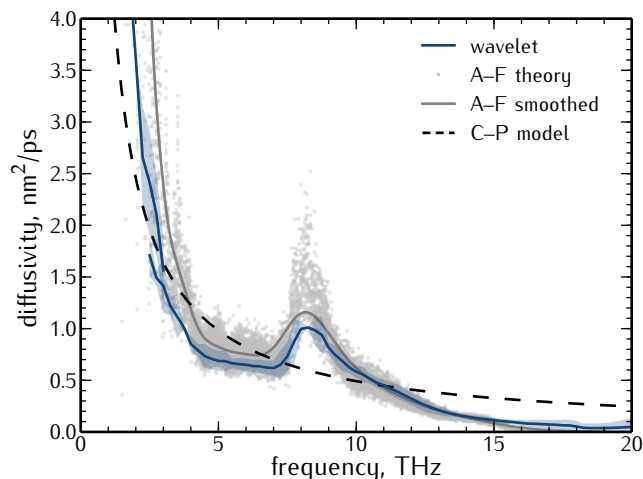


Figure 6.5: Comparison of Cahill–Pohl model, Allen–Feldman theory, and present predictions of vibrational diffusivity in simulated amorphous silicon. The blue shading gives the 95% confidence interval of the diffusivity based on 8 trials.

roduced by the wavelet transform is proportional to the frequency, and the C–P model is inversely proportional to the frequency, the C–P model prediction was unaffected.

Accounting for the frequency-blurring of the wavelet transform, the prediction of the present method closely follows the A–F theory prediction, qualitatively reproducing the spike in the diffusivity at ~ 8 THz. As seen in Figures 6.2 and 6.4j, the diffusivity above 15 THz is over-estimated because of the fitting procedure employed. At low frequencies, the diffusivity is under-estimated. Correcting the fitting procedure will therefore lead to better agreement with the A–F theory in these extremes. The agreement with the A–F theory at intermediate frequencies might be improved by using a smaller Lorentzian broadening. Similarly, if the A–F theory calculation could be performed on a system of comparable size, the average frequency spacing of the eigenmode frequencies would decrease, achieving the same effect. It appears that, if the frequency-blurring can be tolerated, the present method gives the same prediction as the A–F theory.

The C–P model, while not being able to account for the spike in the diffusivity, roughly interpolates both the A–F theory and the present prediction. As the thermal conductivity is proportional to the area under the spectral diffusivity curve, the interpolation provides some explanation as to why it gives decent predictions of the high temperature thermal conductivity of disordered materials.

Now that the accuracy, caveats, and limitations of the wavelet transform-based method have been explored, I apply it to study the effect of bond strength and structure on the spectral diffusivity of amorphous silicon. The frequency-dependent vibrational diffusivities of the quenched and WWW VBWM, averaged, and SW structures are plotted in Figure 6.6.

The spectral diffusivity of the VBWM and averaged potentials are about the same for the structures generated by quenching and relaxation of the WWW structure. This is in contrast to the SW potential, which shows a great difference between the two structures below 3 THz and in the spike region. Examining the radial distribution function of quenched SW a-Si compared to the others in Figure 6.7 provides a clue as to why. The RDF of the quenched SW

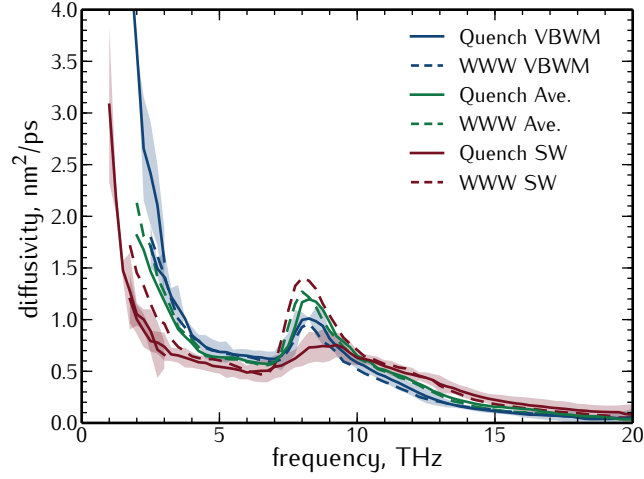


Figure 6.6: Spectral diffusivity of a-Si obtained by the wavelet transform-based method for different bond strengths and structures. Each line is the average of at least 8 trials. The shaded regions give the 95% confidence interval, which are only shown for the quenched VBWM and SW potentials for clarity.

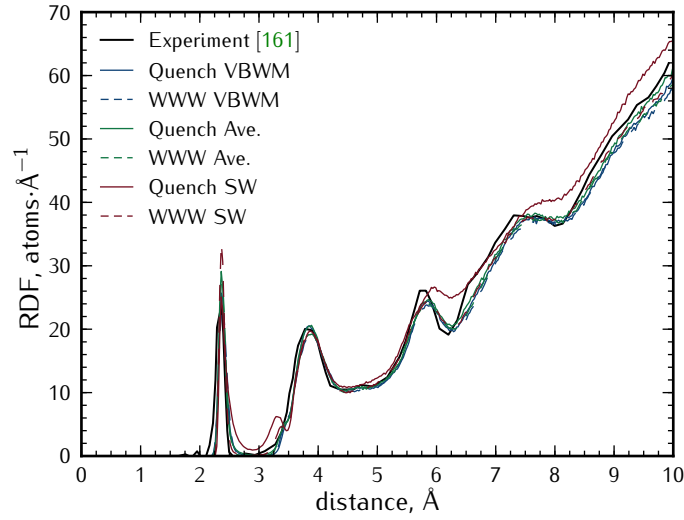


Figure 6.7: Radial distribution functions of the small-scale a-Si structures compared to each other and experiment.

structure significantly differs from the others, including the WWW SW structure. There is no such difference between the quenched and WWW RDFs of the other two potentials. Thus, the anomalous spectral diffusivity of the quenched SW below 3 THz and in the spike region is correlated with the features of the structure's RDF. This suggests that the greater disorder of the quenched SW structure is preferentially suppressing the high-diffusivity transverse- and longitudinal-like vibrations in the low frequency and spike regions. The quenched and WWW VBWM structures are similar because both the potential and the structure come from the same group and were published within a year of each other [135, 200].

Aside from the peak, the three potentials display a systematic ordering. Above the peak, the ordering is according to their longitudinal velocities: quenched VBWM has a v_L of 7.32 nm/ps and quenched SW has a v_L of 8.41 nm/ps, with the averaged potential in between. Below the peak, they are ordered according to their transverse velocities: quenched VBWM has a v_T of 4.08 nm/ps and quenched SW has a v_T of 3.62 nm/ps, with the averaged potential

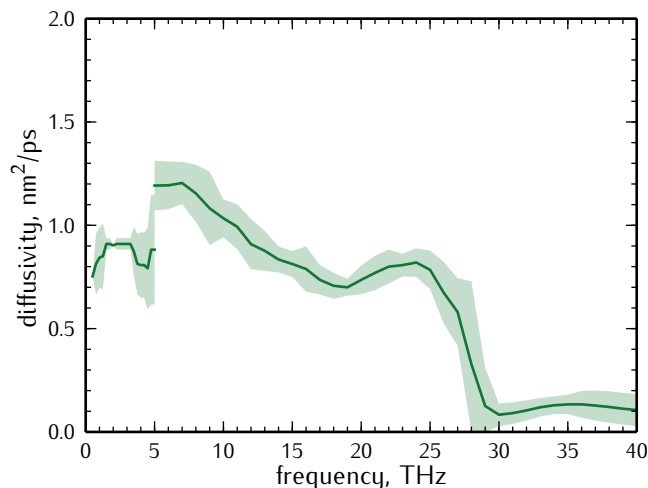


Figure 6.8: Spectral diffusivity of simulated a-SiO₂ obtained by the wavelet transform-based method. Each line segment is the average of at least 10 trials. The shaded region gives the 95% confidence interval.

in between. This dependence on the acoustic sound speeds is consistent with the linear trend of Figure 6.4a and the interpretation of the spike by Feldman *et al.* as being due to longitudinal propagons above the cutoff frequency of transverse propagons [27].

Finally, the results for a-SiO₂ are plotted in Figure 6.8. The overall shape is quite different from that of a-Si. Larkin and McGaughey have observed a spike in the diffusivity at ~ 35 THz [149], presumably due to optical-like modes. The frequency-blurring of the wavelet transform is so great at that frequency that the spike is dramatically eroded. The low-frequency diffusivity does not align between the small- and large-scale simulations. The reason for this discrepancy is unknown at this time, but the discrepancy nevertheless illustrates the need for some refinement of the simulation or fitting procedures.

6.5 CONTRIBUTIONS

In this chapter, I demonstrated the efficacy of a wavelet transform-based simulation method for calculating the frequency-dependent vibrational diffusivity of an amorphous material. Its predictions qualitatively agree with those of the Allen–Feldman theory, and the agreement may be made quantitative by refining the fitting procedure for the lowest and highest frequencies. By providing an independent point of comparison between the Allen–Feldman theory and the Cahill–Pohl model, the present results demonstrate why the Cahill–Pohl model provides reasonable predictions of the high temperature thermal conductivity of disordered materials: the frequency-dependent diffusivity it uses roughly interpolates the Allen–Feldman curve.

The new method has a few advantages over the Allen–Feldman theory. By avoiding calculations involving the dynamical matrix, the new method has the same computational scaling as the molecular dynamics simulation itself. Since the simulation occurs with the system in its ground-state, the atoms move very little and so the neighbor list never requires updating [85]. In this case, the computational scaling of the molecular dynamics simulation is formally $\mathcal{O}(N)$.

The wavelet transform analysis, too, scales as $\mathcal{O}(N)$.⁵ The $\mathcal{O}(N)$ scaling represents a significant improvement over the $\mathcal{O}(N^3)$ scaling of the Allen–Feldman theory.

The superior scaling of the method permits very large scale simulations of an amorphous material; simulations as large as 12 million atoms or 62.5^3 nm^3 were used in this work. With such large domain sizes, the low-frequency propagon transport can be directly observed for the first time in simulation. This will permit a better understanding of the propagon scattering due to disorder of the amorphous structure and the crossover between propagon and diffuson dominated transport [28, 149]. A supplemental benefit of the method is that the force constants experienced by the atoms need not be known, which might allow more complicated empirical potentials which lack a tractable analytical form of the second order derivative to be used.

Finally, because of the very large scale simulations enabled by the present method, it might be used to explore transport through disordered materials with feature sizes greater than a few nanometers, like polymers or even aerogels.

⁵ The calculation of the radial distribution function may be done by averaging over a subset of the atoms, giving a scaling of $\mathcal{O}(N)$, and sorting the atoms into the radial bins has a scaling of $\mathcal{O}(N \log N)$, but this step is negligible compared to the others in terms of resources.

7

CONCLUSIONS

The contributions of my doctoral research to the scientific community as discussed in this dissertation are: 1) the development of the wavelet transform with attention to its application to studies of nanoscale thermal transport using molecular dynamics simulation; 2) three new simulation procedures and accompanying analysis methods based on the wavelet transform; 3) a comparative study of the abilities of several potentials to model the thermophysical properties of amorphous silicon and amorphous silica along with detailed data regarding the effect of the quench rate on the final properties; 4) a systematic investigation into the effects of long- and short-range order in alloys that transport heat by lattice vibrations with the new finding that the short-range order entirely determines the thermal conductivity; and 5) a detailed proof-of-concept for one of the newly developed simulation procedures and the comparison of its predictions of the frequency-dependent vibrational diffusivity to those of the Cahill–Pohl model [7, 32] and the Allen–Feldman theory [25–28].

The wavelet transform as detailed in Section 2.1 is the most natural presentation to date of the technique with regard to analysis of nanoscale thermal transport because of its conversion of a temporal (or spatial) signal directly into a time-frequency or space-wavenumber domain, unlike previous implementations that convert the signal to a time-scale domain [91, 97, 98]. The numerical code that implements the wavelet transform as presented in Section 2.1 will be made available to the research community, along with a tutorial based on Figure 2.3 that demonstrates the transform’s properties.

A general algorithm for the construction of simulated binary alloys with specified composition, long-range order, and short-range order was presented in Section 2.3. While this algorithm was only implemented for an alloy with a zincblende structure as the ordered state in this dissertation, the algorithm could be generalized to other crystal structures in future work. The discussion of order parameters and their practical implementation regarding simulations may be useful to both simulationists and experimentalists alike.

Three new simulation procedures and analysis methods based on the wavelet transform were presented in Chapter 3. The new approaches cover a plethora of physical phenomena in nanoscale thermal transport. Simulations with the wave-packet technique [110] were analyzed to observe the anharmonic scattering of a wave-packet, approximating a phonon, and phonon scattering with non-ideal interfaces. The coherent interaction of a phonon with a geometrically sharp interface was captured in the analysis and might provide clues as to the scattering of phonons with wavelengths on the order of the interface roughness, where the scattering may not be specular or diffusive [113].

Analysis of steady-state non-equilibrium thermal transport across an interface in a one-dimensional chain showed the potential for the wavelet transform to extract localized phonon

populations near an interface. Against such information, the assumptions behind models of interfacial thermal transport can be tested [113]. This type of simulation can be adapted to non-equilibrium simulations that have a finite cross section to provide information on the phonon populations that may be found in a more realistic system. I believe my colleague Nam Le is already pursuing such simulations and will present them in his dissertation.

In Section 3.3, the final simulation procedure based on the capabilities of wavelet transform analysis was presented. The method can be used to make predictions of the frequency-dependent vibrational diffusivity of an amorphous material. The method, though yielding comparable information to the Allen–Feldman theory, has a much better computational scaling of $\mathcal{O}(N)$, compared to $\mathcal{O}(N^3)$ for the Allen–Feldman theory. Furthermore, the method does not require the force constants experienced by the atoms to make its prediction. The efficacy of the method was tested in Chapter 6 and shown to agree with the Allen–Feldman theory, and the quantitative agreement would be improved by refining the fitting procedure. The superior scaling of the new method permits simulations of tens of millions of atoms, allowing for the thermal transport properties of new materials to be explored. The large-scale simulations also permit direct observation of the propagon transport for the first time.

The systematic comparison of the abilities of various potentials to model the thermophysical properties of amorphous silicon and amorphous silica in Chapter 4 benefits the members of the simulation community by informing the selection of potentials for future studies. A great deal of data relating to the effect of quench rate on the structural and vibrational properties of the amorphous material was also generated. This information may aid future researchers interpreting their own simulations or developing theories for the effect of quench rate on the thermophysical properties of an amorphous material.

Lastly, in Chapter 5, the novel study of the effects of long- and short-range order in a $\text{Si}_{0.5}\text{Ge}_{0.5}$ alloy on its thermal conductivity provides new insight into the thermal transport by lattice vibrations in alloys. It was found that the nearest-neighbor short-range order determines the thermal conductivity. This effect was interpreted as the result of the short-range order modifying the vibrational eigenstates of the material. Whereas low frequency phonons transport most of the heat in the disordered structure [53], the increase in short-range ordering reduces their scattering and allows higher frequency modes to contribute to the thermal conductivity. This could have a major implication for the nanoscale heat transfer community: when trying to tune the thermal conductivity of a semiconducting alloy by altering its ordering, caution dictates the use of a characterization technique sensitive to the short-range order. Otherwise a sample with low long-range order, but greater short-range order, might be mistakenly discarded.

In conclusion, the potential of the wavelet transform to extract information on the fundamental physics of both phonon transport in crystalline systems and vibrational transport in amorphous systems is clearly not yet fully realized. This doctoral work serves as a starting point for future developments of the wavelet transform-based simulation and analysis techniques. Future efforts should focus on refining the quantitative predictions made by the wavelet transform and on expanding the simulation methodologies into new material systems. This doctoral work lays the foundation for new simulation methods that will enable simula-

tionists to partner with experimentalists and theorists to perhaps develop the next generation of theories of nanoscale thermal transport, covering such varied phenomena as thermal boundary conductance and the thermal conductivity of amorphous materials.

ACKNOWLEDGEMENTS

This work would not be possible without a great many people. I would first like to thank my undergraduate thesis advisor, Prof. Chuan-Hua Chen, for sparking in me a passion for research. It was in his lab that I learned to strive for creativity. I am very grateful for my graduate student mentor in that lab, now Professor Jonathan Boreyko, who taught me the basics and has become a lifelong friend. Conducting this doctoral research would be impossible without my advisor, Prof. Pamela Norris, who had faith in me from my first day and provided a research environment where independence and ingenuity can flourish. I am indebted to all my colleagues in the lab, especially Nam Le, for bearing with me in my brain-storming sessions, and for always being quick to lend an ear, whether it be for celebration or commiseration. They have made these last five years a pleasure and have set a high, high standard for future colleagues.

Each member of my committee has had a special role in shaping my academic experience. The enthusiasm of Prof. Patrick Hopkins is contagious, and his appreciation for my work has been a source of reassurance and motivation. If I already had a working knowledge of molecular dynamics, Prof. Leo Zhigilei's mentorship and class gave me the theoretical foundation upon which much of this work is built. In the particulars of nanoscale thermal transport in molecular dynamics simulation, Prof. Alan McGaughey has been a role model and facilitator by hosting his annual simulators meeting. Finally, I thank Prof. Cass Sackett for teaching the finest course I took at U.Va. and for giving me a sense of awe and wonder for pure physics and those who practice it.

There are many who contributed directly to the quality of this work, several of whom I have already mentioned. To single out a few, Prof. Alan McGaughey has been extremely generous in critiquing a couple of my publications before submission; they would not have the quality they do if not for his expertise and his willingness to share it. Prof. Leo Zhigilei pointed me in the right direction by suggesting the Monte Carlo approach for generating the alloys investigated in this work and mentored me on my first conference paper. Dr. Don Jordan was fortuitously placed in my life as his expertise in the wavelet transform and his clear gift for mentorship were instrumental in getting me started with the technique. Lastly, Prof. Patrick Hopkins, too, has freely lent his insight.

Finally, I would like to acknowledge funding from my NDSEG fellowship, the access to computing resources that it has provided, and the folks who keep those resources operational and have helped me utilize them. I have greatly appreciated the latitude afforded to me by the fellowship to pursue and develop my ideas. I have surely been spoiled by the freedom and computational resources.

LIST OF SYMBOLS

Chapter 1

f	Frequency	Hz
k	Thermal conductivity	$\text{Wm}^{-1}\text{K}^{-1}$
x	Element concentration in alloy	~
N	Number of elements in alloy	~
T	Temperature	K

Chapter 2

c	Concentration of atoms in alloy	~
\mathbf{e}	Normal mode polarization vector	~
f	Frequency	Hz
f'	Peak frequency of wavelet	Hz
f'_{\min}	Minimum analyzable frequency	Hz
f'_{\max}	Maximum analyzable frequency	Hz
f_N	Nyquist frequency	Hz
f_ψ	Mother wavelet frequency	~
g	Arbitrary function of one variable	~
j	Basis index in crystal	~
\mathbf{k}	Wavevector	m^{-1}
k_B	Boltzmann's constant	$\text{J}\cdot\text{K}^{-1}$
l	Unit cell index in crystal	~
l_t	Time duration of signal	s
m	Atomic mass	kg
n	Number of atoms in neighbor shell	~
p	Probability of element occupying crystal site	~
r	Fraction of sites occupied by an atom in ordered alloy ¹	~
\mathbf{r}	Position vector of atom in crystal	m
t	Time	s
t_f	Duration of atomic trajectory	s
t'	Peak time of wavelet	s
t°	Periodic time coordinate	s
$\dot{\mathbf{u}}$	Atomic velocity vector	m/s
x	Element concentration in alloy	~
C	Admissibility constant of wavelet transform	~
\mathcal{F}	Fourier transform	~
\mathbb{L}	Long-range order parameter of alloy	~
N	Number of unit cells in crystal	~
N'_t	Number of samples in t'	~
Q	Normal mode coordinate	$\text{kg}^{\frac{1}{2}}\text{m}$
S	Short-range order parameter of alloy	~
T	Temperature	K
\mathcal{W}	Wavelet transform	~

¹ See text for clarification

α	Warren-Cowley short-range order parameter of alloy	~
Δt	Sampling time of signal	s
η	Decay ratio of wavelet near f_N	~
ν	Polarization index	~
ρ	Wavelet energy density	$[g]^2\text{s}/(\text{s}\cdot\text{Hz})$
σ_f	Frequency uncertainty of wavelet transform	Hz
σ_t	Time uncertainty of wavelet transform	s
ϕ	Fraction of wavelet domain with edge artifacts	~
ψ	Kernal function of transform	~
ω	Angular frequency	$\text{rad}\cdot\text{s}^{-1}$
\hat{g}	Fourier transform of g	$[g]\text{s}$
\tilde{g}	Wavelet transform of g	$[g]\text{s}$

Chapter 3

\mathbf{e}	Normal mode polarization vector	~
f_p	Wave-packet peak frequency	Hz
g	Density of states in 1-D chain	$\text{states}\cdot\text{m}^{-2}$
j	Basis index in crystal	~
k	Wavenumber in 1-D chain	m^{-1}
k^*	Brillouin Zone boundary of 1-D chain	m^{-1}
k_B	Boltzmann's constant	$\text{J}\cdot\text{K}^{-1}$
k_p	Wavepacket peak wavenumber	m^{-1}
m	Atomic mass	kg
n	Numerical index	~
l	Unit cell index in crystal	~
r	Radial distance	m
t	Time	s
\mathbf{u}	Atomic displacement vector	m
$\dot{\mathbf{u}}$	Atomic velocity vector	$\text{m}\cdot\text{s}^{-1}$
v	Atomic velocity or wave velocity	$\text{m}\cdot\text{s}^{-1}$
x	Spatial coordinate	m
z	Spatial coordinate	m
z_p	Wave-packet peak position	m
A	Wave-packet amplitude	m
R	Radius of a sphere	m
T	Temperature	K
α	Thermal diffusivity	$\text{m}^2\cdot\text{s}^{-1}$
γ	Relaxation rate	s^{-1}
ϵ	Dummy radial distance	m
θ	Kinetic energy	$\text{kg}\cdot\text{m}^2\cdot\text{s}^{-2}$
σ	Wave-packet width or Gaussian width	m

Chapter 4

f	Frequency	Hz
\hbar	Reduced Planck's constant	$\text{JHz}^{-1}\text{rad}^{-1}$
i	Indexes acoustic branches or normal modes	~
SW	Stillinger-Weber Si potential [132]	~
SW	Vink <i>et al.</i> Si potential [135]	~
SW ₁₁₅	Albenze <i>et al.</i> Si potential [136]	~
EDIP	Justo <i>et al.</i> Si potential [134]	~
M ₃ S	Munetoh <i>et al.</i> SiO ₂ potential [137]	~
BKS	van Beest <i>et al.</i> SiO ₂ potential [138]	~

TTAM	Tsuneyuki <i>et al.</i> SiO ₂ potential [139]	~
RDF	Radial distribution function	atoms·m ⁻¹
ADF	Angle distribution function	deg. ⁻¹
NPT	Constant number, pressure, temperature ensemble	~
NPH	Constant number, pressure, enthalpy ensemble	~

Chapter 5

f	Frequency	Hz
f_0	Normal mode anharmonic frequency	Hz
i	Indexes neighbor shells	~
k	Thermal conductivity	Wm ⁻¹ K ⁻¹
k_B	Boltzmann's constant	J·K ⁻¹
l	Cubic domain side length	m
\dot{q}	Normal mode velocity coordinate	kg ^{1/2} ms ⁻¹
r	Neighbor shell radius	m
t_f	Duration of simulation	s
x	Element concentration in alloy	~
A	Normal mode kinetic energy	J
L	Long-range order parameter of alloy	~
N	Number of unit cells along cube side	~
\dot{Q}	Fourier transform of normal mode velocity coordinate	kg ^{1/2} m
R	Number of rightly ordered atoms	~
S	Short-range order parameter of alloy	~
T	Temperature	K
W	Number of wrongly ordered atoms	~
Γ	Lorentzian half-width at half-max	Hz
ν	Index of normal modes	~
σ	Uncertainty in thermal conductivity	Wm ⁻¹ K ⁻¹
τ	Normal mode relaxation time	s

Chapter 6

f	Frequency	Hz
\hbar	Reduced Planck's constant	JHz ⁻¹ rad ⁻¹
i	Indexes acoustic branches or normal modes	~
j	Indexes normal modes	~
k	Thermal conductivity	Wm ⁻¹ K ⁻¹
k_B	Boltzmann's constant	J·K ⁻¹
l_t	Duration of simulation	s
n	Number density of atoms	atoms·m ⁻³
v	Velocity	ms ⁻¹
v_L	Longitudinal acoustic sound speed	ms ⁻¹
v_T	Tranverse acoustic sound speed	ms ⁻¹
C	Heat capacity	Jm ⁻³ K ⁻¹
D	Diffusivity	m ² s ⁻¹
L	Minimum of domain dimensions	m
N	Number of elements in computation	~
\mathbf{S}	Heat current operator	Jm ⁻² s ^{-1/2}
T	Temperature	K
U	Internal energy	J
V	Volume	m ³
γ	Relaxation rate	s ⁻¹
Θ	Debye temperature	K

Λ Mean-free-path
 ω Angular frequency

m
 $\text{rad}\cdot\text{s}^{-1}$

BIBLIOGRAPHY

- [1] C. Kittel, *Introduction to Solid State Physics* (John Wiley and Sons, 2005).
- [2] S. R. Elliot, *Physics of Amorphous Materials* (Longman Scientific and Technical, 1990).
- [3] R. C. Zeller and R. O. Pohl, *Physical Review B* **4**, 2029 (1971).
- [4] J. J. Freeman and A. C. Anderson, *Physical Review B* **34**, 5684 (1986).
- [5] R. O. Pohl, X. Liu, and E. Thompson, *Reviews of Modern Physics* **74**, 991 (2002).
- [6] V. Lunchenko and P. G. Wolynes, *Advances in Chemical Physics* **136**, 95 (2007).
- [7] D. G. Cahill and R. O. Pohl, *Solid State Communications* **70**, 927 (1989).
- [8] A. I. Krivchikov, A. N. Yushchenko, V. G. Manzhelii, O. A. Korolyuk, F. J. Bermejo, R. Fernández-Perea, C. Cabrillo, and M. A. González, *Physical Review B* **74**, 060201(R) (2006).
- [9] A. R. Adams, F. Baumann, and J. Stuke, *Physica Status Solidi* **23**, K99 (1967).
- [10] C. J. Glassbrenner and G. A. Slack, *Physical Review* **134**, 1058 (1964).
- [11] R. Berman, E. L. Foster, and J. M. Ziman, *Proceedings of the Royal Society of London A* **237**, 344 (1956).
- [12] G. A. Slack, D. W. Oliver, and F. H. Horn, *Physical Review B* **4**, 1714 (1971).
- [13] G. K. White, S. B. Woods, and M. T. Eford, *Physical Review* **112**, 111 (1958).
- [14] B. L. Zink, R. Pietri, and F. Hellman, *Physical Review Letters* **96**, 055902 (2006).
- [15] G. Pompe and E. Hegenbarth, *Physica Status Solidi B* **147**, 103 (1988).
- [16] M. Shamsa, W. L. Liu, A. A. Balandin, C. Casiraghi, W. I. Milne, and A. C. Ferrari, *Applied Physics Letters* **89**, 161921 (2006).
- [17] O. A. Golikova, V. K. Zaitsev, V. M. Orlov, A. V. Petrov, L. S. Stilbans, and E. N. Tkalenko, *Physica Status Solidi A* **21**, 405 (1974).
- [18] P. W. Anderson, B. I. Halperin, and C. M. Varma, *Philosophical Magazine* **25**, 1 (1971).
- [19] W. A. Phillips, *Journal of Low Temperature Physics* **7**, 351 (1972).
- [20] A. Heuer and R. J. Silbey, *Physical Review Letters* **70**, 3911 (1993).
- [21] A. Heuer, *Physical Review Letters* **78**, 4051 (1997).
- [22] J. Reinisch and A. Heuer, *Physical Review Letters* **95**, 155502 (2005).
- [23] A. Heuer, in *Tunneling Systems in Amorphous and Crystalline Solids* (Springer, 1998), chap. 8.
- [24] U. Buchenau, Y. M. Galperin, V. L. Gurevich, D. A. Parshin, M. A. Ramos, and H. R. Schober, *Physical Review B* **46**, 2798 (1992).
- [25] P. B. Allen and J. L. Feldman, *Physical Review Letters* **62**, 645 (1989).
- [26] P. B. Allen and J. L. Feldman, *Physical Review B* **48**, 12581 (1993).

- [27] J. L. Feldman, M. D. Kluge, P. B. Allen, and F. Wooten, *Physical Review B* **48**, 12589 (1993).
- [28] J. L. Feldman, P. B. Allen, and S. R. Bickham, *Physical Review B* **59**, 3551 (1999).
- [29] M. T. Dove, *Introduction to Lattice Dynamics* (Cambridge University Press, 1993).
- [30] W. Lv and A. Henry, *unpublished* (2015).
- [31] D. G. Cahill, H. E. Fischer, T. Klitsner, E. T. Swartz, and R. O. Pohl, *Journal of Vacuum Science and Technology A* **7**, 1259 (1989).
- [32] D. G. Cahill, S. K. Watson, and R. O. Pohl, *Physical Review B* **46**, 6131 (1992).
- [33] A. Einstein, *Annalen der Physik* **35/340**, 679 (1911).
- [34] M. Wuttig and N. Yamada, *Nature Materials* **6**, 824 (2007).
- [35] S. Raoux, F. Xiong, M. Wuttig, and E. Pop, *MRS Bulletin* **39**, 703 (2014).
- [36] D. R. Clarke and S. R. Phillpot, *Materials Today* **8**, 22 (2005).
- [37] P. G. Le Comber, *Journal of Non-Crystalline Solids* **115**, 1 (1989).
- [38] W. L. Johnson and K. Samwer, *Physical Review Letters* **95**, 195501 (2005).
- [39] G. J. Grabovskij, T. Peichl, J. Lisenfeld, G. Weiss, and A. V. Ustinov, *Science* **338**, 232 (2012).
- [40] W. L. Bragg and E. J. Williams, *Proceedings of the Royal Society of London A* **145**, 699 (1934).
- [41] J. M. Cowley, *Physical Review* **77**, 669 (1950).
- [42] B. D. Cullity and S. R. Stock, *Elements of X-ray diffraction* (Prentice Hall, 2001).
- [43] S. Adachi, *Properties of Semiconductor Alloys: Group-IV, III-V and II-VI Semiconductors* (John Wiley and Sons, 2009).
- [44] G. Joshi, H. Lee, Y. Lan, X. Wang, G. Zhu, D. Wang, R. W. Gould, D. C. Cuff, M. Y. Tang, M. S. Dresselhaus, et al., *Nano Letters* **8**, 4670 (2008).
- [45] Y. Pei, X. Shi, A. LaLonde, H. Wang, L. Chen, and G. J. Snyder, *Nature* **473**, 66 (2011).
- [46] C. Y. Ho, M. W. Ackerman, K. Y. Wu, S. G. Oh, and T. N. Havill, *Journal of Physical and Chemical Reference Data* **7**, 959 (1978).
- [47] H. Stöhr and W. Klemm, *Zeitschrift für anorganische und allgemeine Chemie* **241**, 305 (1939).
- [48] B. Abeles, D. S. Beers, G. D. Cody, and J. P. Dismukes, *Physical Review* **125**, 44 (1962).
- [49] J. P. Dismukes, L. Ekstrom, E. F. Steigmeier, I. Kudman, and D. S. Beers, *Journal of Applied Physics* **35**, 2899 (1964).
- [50] H. Wang, A. D. LaLonde, Y. Pei, and G. J. Snyder, *Advanced Functional Materials* **23**, 1586 (2013).
- [51] B. Abeles, *Physical Review* **131**, 1906 (1963).
- [52] S. ichiro Tamura, *Physical Review B* **27**, 858 (1983).
- [53] J. Garg, N. Bonini, B. Kozinsky, and N. Marzari, *Physical Review Letters* **106**, 045901 (2011).
- [54] Z. Tian, J. Garg, K. Esfarjani, T. Shiga, J. Shiomi, and G. Chen, *Physical Review B* **85**, 184303 (2012).
- [55] J. M. Larkin and A. J. H. McGaughey, *Journal of Applied Physics* **114**, 023507 (2013).
- [56] T. Beechem, S. Graham, P. Hopkins, and P. Norris, *Applied Physics Letters* **90**, 054104 (2007).
- [57] M. Plischke and D. Mattis, *Physical Review Letters* **27**, 42 (1971).
- [58] A. Jezierski, *Physica Status Solidi B* **178**, 373 (1993).

- [59] A. E. Asch and G. L. Hall, *Physical Review* **132**, 1047 (1963).
- [60] M. Brauwiers, J. Giner, J. Van der Rest, and F. Brouers, *Solid State Communications* **17**, 229 (1975).
- [61] S. McKenzie, *Journal of Physics C: Solid State Physics* **16**, 2509 (1983).
- [62] J. W. Harrison and J. R. Hauser, *Physical Review B* **13**, 5347 (1976).
- [63] J. R. Hauser, M. A. Littlejohn, and T. H. Glisson, *Applied Physics Letters* **28**, 458 (1976).
- [64] J. W. Harrison and J. R. Hauser, *Journal of Applied Physics* **47**, 292 (1976).
- [65] E. Pop, *Nano Research* **3**, 147 (2010).
- [66] M. Laradji, D. P. Landau, and B. Dünweg, *Physical Review B* **51**, 4894 (1995).
- [67] I. Vurgaftman, J. R. Meyer, and L. R. Ram-Mohan, *Journal of Applied Physics* **89**, 5815 (2001).
- [68] F. K. LeGoues, V. P. Kesan, and S. S. Iyer, *Physical Review Letters* **64**, 40 (1990).
- [69] K. L. Whiteaker, I. K. Robinson, J. E. Van Nostrand, and D. G. Cahill, *Physical Review B* **57**, 12410 (1998).
- [70] J. C. Duda, T. S. English, D. A. Jordan, P. M. Norris, and W. A. Soffa, *Journal of Physics: Condensed Matter* **23**, 205401 (2011).
- [71] J. C. Duda, T. S. English, D. A. Jordan, P. M. Norris, and W. A. Soffa, *Journal of Heat Transfer* **134**, 014501 (2012).
- [72] A. J. Minnich, M. S. Dresselhaus, Z. F. Ren, and G. Chen, *Energy and Environmental Science* **2**, 466 (2009).
- [73] C. J. Vineis, A. Shakouri, A. Majumdar, and M. G. Kanatzidis, *Advanced Materials* **22**, 3970 (2010).
- [74] M. H. Kryder, E. C. Gage, T. W. McDaniel, W. A. Challener, R. E. Rottmayer, G. Ju, Y.-T. Hsia, and M. F. Erden, *Proceedings of the IEEE* **96**, 1810 (2008).
- [75] J. Chen, G. Zhang, and B. Li, *Applied Physics Letters* **95**, 073117 (2009).
- [76] N. Mingo, D. Hauser, N. P. Kobayashi, M. Plissonnier, and A. Shakouri, *Nano Letters* **9**, 711 (2009).
- [77] H. Kim, I. Kim, H. jin Choi, and W. Kim, *Applied Physics Letters* **96**, 233106 (2010).
- [78] Z. Wang and N. Mingo, *Applied Physics Letters* **97**, 101903 (2010).
- [79] A. Kundu, N. Mingo, D. A. Broido, and D. A. Stewart, *Physical Review B* **84**, 125426 (2011).
- [80] C. Abs da Cruz, N. A. Katcho, N. Mingo, and R. G. A. Veiga, *Journal of Applied Physics* **114**, 164310 (2013).
- [81] L. Pan and D. B. Bogy, *Nature Photonics* **3**, 189 (2009).
- [82] R. Fernandez, D. Teweldebrhan, C. Zhang, A. Balandin, and S. Khizroev, *Journal of Applied Physics* **109**, 07B763 (2011).
- [83] H. Ho, A. A. Sharma, W.-L. Ong, J. A. Malen, J. A. Bain, and J.-G. Zhu, *Applied Physics Letters* **103**, 131907 (2013).
- [84] A. Chernyshov, D. Treves, T. Le, F. Zong, A. Ajan, and R. Acharya, *Journal of Applied Physics* **115**, 17B735 (2014).
- [85] M. P. Allen and D. J. Tildesley, *Computer Simulation of Liquids* (Oxford University Press, 1989).
- [86] D. Frenkel and B. Smit, *Understanding Molecular Simulation: from Algorithms to Applications* (Academic Press, 2001).
- [87] D. Sholl and J. A. Steckel, *Density Functional Theory: a Practical Introduction* (Wiley-Interscience, 2009).
- [88] R. N. Bracewell, *The Fourier Transform and Its Applications* (McGraw-Hill, 1999).
- [89] J. J. Salacuse, A. R. Denton, and P. A. Egelstaff, *Physical Review E* **53**, 2382 (1996).

- [90] G. Kaiser, *A Friendly Guide to Wavelets* (Birkhauser, 1994).
- [91] M. Farge, *Annu. Rev. Fluid Mech.* **24**, 395 (1992).
- [92] P. Goupillaud, A. Grossman, and J. Morlet, *Geoexploration* **23**, 85 (1984).
- [93] S. G. Mallat, *IEEE Transactions on Pattern Analysis and Machine Intelligence* **11**, 674 (1989).
- [94] M. Antonini, M. Barlaud, P. Mathieu, and I. Daubechies, *IEEE Transactions on Image Processing* **1**, 205 (1992).
- [95] C. Torrence and G. P. Compo, *Bulletin of the American Meteorological Society* **79**, 61 (1998).
- [96] J. Shiomi and S. Maruyama, *Physical Review B* **73**, 205420 (2006).
- [97] D. Jordan, R. W. Miksad, and E. J. Powers, *Rev. Sci. Instrum.* **68**, 1484 (1997).
- [98] C. H. Baker, D. A. Jordan, and P. M. Norris, *Physical Review B* **86**, 104306 (2012).
- [99] M. Plancherel and M. Leffler, *Rendiconti del Circolo Matematico di Palermo* **30**, 289 (1910).
- [100] E. C. Titchmarsh, *Proceedings of London Mathematical Society* **23**, 279 (1925).
- [101] J. W. Cooley and J. W. Tukey, *Mathematics of Computation* **19**, 297 (1965).
- [102] P. K. Schelling, S. R. Phillpot, and P. Keblinski, *Journal of Applied Physics* **95**, 6082 (2004).
- [103] R. J. Stevens, L. V. Zhigilei, and P. M. Norris, *International Journal of Heat and Mass Transfer* **50**, 3977 (2007).
- [104] C. F. Carlborg, J. Shiomi, and S. Maruyama, *Physical Review B* **78**, 205406 (2008).
- [105] M. Hu, P. Keblinski, and P. K. Schelling, *Physical Review B* **79**, 104305 (2009).
- [106] J. A. Thomas, R. M. Iutzi, and A. J. H. McGaughey, *Physical Review B* **81**, 045413 (2010).
- [107] M. Shen, W. J. Evans, D. Cahill, and P. Keblinski, *Physical Review B* **84**, 195432 (2011).
- [108] T. S. English, J. C. Duda, J. L. Smoyer, D. A. Jordan, P. M. Norris, and L. V. Zhigilei, *Physical Review B* **85**, 035438 (2012).
- [109] H. Sato, in *Physical Chemistry: An Advanced Treatise*, edited by W. Jost (Academic Press, 1970), vol. 10, chap. 10, p. 579.
- [110] P. K. Schelling, S. R. Phillpot, and P. Keblinski, *Applied Physics Letters* **80**, 2484 (2002).
- [111] W. A. Little, *Canadian Journal of Physics* **37**, 334 (1959).
- [112] E. T. Swartz and R. O. Pohl, *Reviews of Modern Physics* **61**, 605 (1989).
- [113] P. M. Norris, N. Q. Le, and C. H. Baker, *Journal of Heat Transfer* **135**, 061604 (2013).
- [114] L. Sun and J. Y. Murthy, *Journal of Heat Transfer* **132**, 102403 (2010).
- [115] M. Hu, P. Keblinski, J.-S. Wang, and N. Raravikar, *Journal of Applied Physics* **104**, 083503 (2008).
- [116] L. Hu, L. Zhang, M. Hu, J.-S. Wang, B. Li, and P. Keblinski, *Physical Review B* **81**, 235427 (2010).
- [117] N. A. Roberts and D. G. Walker, *Journal of Applied Physics* **108**, 123515 (2010).
- [118] Z. T. Tian, B. E. White, Jr., and Y. Sun, *Applied Physics Letters* **96**, 263113 (2010).
- [119] C. Kimmer, S. Aubry, A. Skye, and P. K. Schelling, *Physical Review B* **75**, 144105 (2007).
- [120] S. Sinha, P. K. Schelling, S. R. Phillpot, and K. E. Goodson, *Journal of Applied Physics* **97**, 023702 (2005).
- [121] S. Simons, *Journal of Physics C: Solid State Physics* **7**, 4048 (1974).

- [122] G. Chen, *Applied Physics Letters* **82**, 991 (2003).
- [123] N. Zuckerman and J. R. Lukes, *Journal of Heat Transfer* **130**, 082402 (2008).
- [124] N. Zuckerman and J. R. Lukes, *Physical Review B* **77**, 094302 (2008).
- [125] J. Fabian and P. B. Allen, *Physical Review Letters* **77**, 3839 (1996).
- [126] A. D. Polyanin, *Handbook of linear partial differential equations for engineers and scientists* (Chapman & Hall/CRC, 2002).
- [127] P. Sheng and M. Zhou, *Science* **253**, 539 (1991).
- [128] Y. M. Beltukov, V. I. Kozub, and D. A. Parshin, *Physical Review B* **87**, 134203 (2013).
- [129] T. Yamane, N. Nagai, S. ichiro Katayama, and M. Todoki, *Journal of Applied Physics* **91**, 9772 (2002).
- [130] P. G. Debenedetti and F. H. Stillinger, *Nature* **410**, 259 (2001).
- [131] H. Jónsson and H. C. Andersen, *Physical Review Letters* **60**, 2295 (1988).
- [132] F. H. Stillinger and T. A. Weber, *Physical Review B* **31**, 5262 (1985).
- [133] J. Tersoff, *Physical Review B* **38**, 9902 (1988).
- [134] J. F. Justo, M. Z. Bazant, E. Kaxiras, V. V. Bulatov, and S. Yip, *Physical Review B* **58**, 2539 (1998).
- [135] R. L. C. Vink, G. T. Barkema, W. F. van der Weg, and N. Mousseau, *Journal of Non-Crystalline Solids* **282**, 248 (2001).
- [136] E. J. Albenze and P. Clancy, *Molecular Simulation* **31**, 11 (2005).
- [137] S. Munetoh, T. Motooka, K. Moriguchi, and A. Shintani, *Computational Materials Science* **39**, 334 (2007).
- [138] B. W. H. van Beest, G. J. Kramer, and R. A. van Santen, *Physical Review Letters* **64**, 1955 (1990).
- [139] S. Tsuneyuki, M. Tsukada, H. Aoki, and Y. Matsui, *Physical Review Letters* **61**, 869 (1988).
- [140] Y. Guissani and B. Guillot, *Journal of Chemical Physics* **104**, 7633 (1996).
- [141] P. Tangney and S. Scandolo, *Journal of Chemical Physics* **117**, 8898 (2002).
- [142] T. Watanabe, H. Fujiwara, H. Noguchi, T. Hoshino, and I. Ohdomari, *Japanese Journal of Applied Physics* **38**, L366 (1999).
- [143] S. Plimpton, *Journal of Computational Physics* **117**, 1 (1995).
- [144] D. Wolf, P. Keblinski, S. R. Phillpot, and J. Eggebrecht, *Journal of Chemical Physics* **110**, 8254 (1999).
- [145] C. J. Fennell and J. D. Gezelter, *Journal of Chemical Physics* **124**, 234104 (2006).
- [146] P. Demontis, S. Spanu, and G. B. Suffritti, *Journal of Chemical Physics* **114**, 7980 (2001).
- [147] J. Kieffer and C. A. Angell, *Journal of Chemical Physics* **90**, 4982 (1989).
- [148] A. J. H. McGaughey and M. Kaviany, *International Journal of Heat and Mass Transfer* **47**, 1799 (2004).
- [149] J. M. Larkin and A. J. H. McGaughey, *Physical Review B* **89**, 144303 (2014).
- [150] F. Wooten, K. Winer, and D. Weaire, *Physical Review Letters* **54**, 1392 (1985).
- [151] D. Henderson, *Journal of Non-Crystalline Solids* **16**, 317 (1974).
- [152] D. A. McQuarrie, *Statistical Mechanics* (University Science Books, 2000).
- [153] A. J. C. Ladd, B. Moran, and W. G. Hoover, *Physical Review B* **34**, 5058 (1986).

- [154] E. S. Landry, Ph.D. thesis, Carnegie Mellon University (2009).
- [155] J. Chen, G. Zhang, and B. Li, *Physics Letters A* **374**, 2392 (2010).
- [156] J. D. Gale and A. L. Rohl, *Molecular Simulation* **29**, 291 (2003).
- [157] K. Laaziri, S. Kycia, S. Roorda, M. Chicoine, J. L. Robertson, J. Wang, and S. C. Moss, *Physical Review Letters* **82**, 3460 (1999).
- [158] S. T. Pantelides, *Physical Review Letters* **57**, 2979 (1986).
- [159] R. Biswas, C. Z. Wang, C. T. Chan, K. M. Ho, and C. M. Soukoulis, *Physical Review Letters* **63**, 1491 (1989).
- [160] S. Roorda, W. C. Sinke, J. M. Poate, D. C. Jacobson, S. Dierker, B. S. Dennis, D. J. Eaglesham, F. Spaepen, and P. Fuoss, *Physical Review B* **44**, 3702 (1991).
- [161] K. Laaziri, S. Kycia, S. Roorda, M. Chicoine, J. L. Robertson, J. Wang, and S. C. Moss, *Physical Review B* **60**, 13520 (1999).
- [162] W. A. Kamitakahara, H. R. Shanks, J. F. McClelland, U. Buchenau, F. Gompf, and L. Pintschovius, *Physical Review Letters* **52**, 644 (1984).
- [163] E. Lorch, *Journal of Physics C* **2**, 229 (1969).
- [164] F. Mauri, A. Pasquarello, B. G. Pfrommer, Y.-G. Yoon, and S. G. Louie, *Physical Review B* **62**, R4786 (2000).
- [165] D. L. Price and J. M. Carpenter, *Journal of Non-Crystalline Solids* **92**, 153 (1987).
- [166] J. M. Carpenter and D. L. Price, *Physical Review Letters* **54**, 441 (1985).
- [167] J. S. Custer, M. O. Thompson, D. C. Jacobson, J. M. Poate, S. Roorda, W. C. Sinke, and F. Spaepen, *Applied Physics Letters* **64**, 437 (1994).
- [168] I. R. Cox-Smith, H. C. Liang, and R. O. Dillon, *Journal of Vacuum Science and Technology A* **3**, 674 (1985).
- [169] L. R. Testardi and J. J. Hauser, *Solid State Communications* **21**, 1039 (1977).
- [170] I. J. Fritz and R. A. Graham, *Journal of Applied Physics* **45**, 4124 (1974).
- [171] Y. Inamura, M. Arai, M. Nakamura, T. Otomo, N. Kitamura, S. M. Bennington, A. Hannon, and U. Buchenau, *Journal of Non-Crystalline Solids* **293**, 389 (2001).
- [172] W. F. Love, *Physical Review Letters* **31**, 822 (1973).
- [173] D. G. Cahill and R. O. Pohl, *Physical Review B* **35**, 4067 (1987).
- [174] K. Vollmayr, W. Kob, and K. Binder, *Physical Review B* **54**, 15808 (1996).
- [175] S. T. Huxtable, A. R. Abramson, C.-L. Tien, A. Majumdar, C. LaBounty, X. Fan, G. Zeng, J. E. Bowers, A. Shakouri, and E. T. Croke, *Applied Physics Letters* **80**, 1737 (2002).
- [176] R. Cheaito, J. C. Duda, T. E. Beechem, K. Hattar, J. F. Ihlefeld, D. L. Medlin, M. A. Rodriguez, M. J. Campion, E. S. Piekos, and P. E. Hopkins, *Physical Review Letters* **109**, 195901 (2012).
- [177] R. B. Wilson and D. G. Cahill, *Nature Communications* **5**, 5075 (2014).
- [178] A. Skye and P. K. Schelling, *Journal of Applied Physics* **103**, 113524 (2008).
- [179] Y. He, I. Savić, D. Donadio, and G. Galli, *Physical Chemistry Chemical Physics* **14**, 16209 (2012).
- [180] T. Hori, T. Shiga, and J. Shiomi, *Journal of Applied Physics* **113**, 203514 (2013).
- [181] J. Z. Tischler, J. D. Budai, D. E. Jesson, G. Eres, P. Zschack, J.-M. Baribeau, and D. C. Houghton, *Physical Review B* **51**, 10947 (1995).

- [182] P. C. Weakliem and E. A. Carter, *Physical Review B* **45**, 13458 (1992).
- [183] S. Nosé, *Journal of Chemical Physics* **81**, 511 (1984).
- [184] W. G. Hoover, *Physical Review A* **31**, 1695 (1985).
- [185] J. M. Larkin, Ph.D. thesis, Carnegie Mellon University (2013).
- [186] J. Shiomi, K. Esfarjani, and G. Chen, *Physical Review B* **84**, 104302 (2011).
- [187] A. J. H. McGaughey and J. M. Larkin, *Annual Review of Heat Transfer* **17**, 49 (2014).
- [188] J. Tersoff, *Physical Review B* **39**, 5566 (1989).
- [189] J. M. Larkin, J. E. Turney, A. D. Massicotte, C. H. Amon, and A. J. H. McGaughey, *Journal of Computational and Theoretical Nanoscience* **11**, 249 (2014).
- [190] B. E. Warren, *X-Ray Diffraction* (Addison-Wesley Publishing Company, Inc., 1969).
- [191] S. Alexander, C. Laermans, R. Orbach, and H. M. Rosenberg, *Physical Review B* **28**, 4615 (1983).
- [192] R. Orbach, *Science* **231**, 814 (1986).
- [193] S. Alexander, O. Entin-Wohlman, and R. Orbach, *Physical Review B* **34**, 2726 (1986).
- [194] A. Aharoney, S. Alexander, O. Entin-Wohlman, and R. Orbach, *Physical Review Letters* **58**, 132 (1987).
- [195] A. Jagannathan, R. Orbach, and O. Entin-Wohlman, *Physical Review B* **39**, 13465 (1989).
- [196] G. Chen, *Nanoscale Energy Transport and Conversion: a parallel treatment of electrons, molecules, phonons, and photons* (Oxford Press, 2005).
- [197] D. A. Broido, M. Malorny, G. Birner, N. Mingo, and D. A. Stewart, *Applied Physics Letters* **91**, 231922 (2007).
- [198] A. Ward, D. A. Broido, D. A. Stewart, and G. Deinzer, *Physical Review B* **80**, 125203 (2009).
- [199] W. H. Press, S. A. Teukolsky, W. T. Vetterling, and B. P. Flannery, *Numerical recipes: the art of scientific computing* (Cambridge University Press, 2007).
- [200] G. T. Barkema and N. Mousseau, *Physical Review B* **62**, 4985 (2000).